La investigación reportada en esta tesis es parte de los programas de investigación del CICESE (Centro de Investigación Científica y de Educación Superior de Ensenada, B.C.).

La investigación fue financiada por el CONAHCYT (Consejo Nacional de Humanidades, Ciencia y Tecnología).

Centro de Investigación Científica y de Educación Superior de Ensenada, Baja California

Doctorado en Ciencias en Oceanografía Física

Interaction between internal gravity waves and balanced motions in the Eastern Boundary Currents

Tesis

para cubrir parcialmente los requisitos necesarios para obtener el grado de

Doctor en Ciencias

Presenta:

César Antonio Pérez Quintana

Ensenada, Baja California, México

2023

Tesis defendida por

César Antonio Pérez Quintana

y aprobada por el siguiente Comité

Dr. José Gómez Valdés
Codirector de tesis

Dr. Héctor Salvador Torres Gutiérrez
Codirector de tesis

Dr. Nicolás Gilles Rascle

Dr. Jorge Vázquez Cuervo

Dr. Juan Manuel López Mariscal

Dr. Jesús Favela Vara

Dra. María Tereza Cavazos Pérez
Coordinadora del Posgrado en Oceanografía Física

Dra. Ana Denise Re Araujo
Directora de Estudios de Posgrado

Resumen de la tesis que presenta César Antonio Pérez Quintana como requisito parcial para la obtención del grado de Doctor en Ciencias en Oceanografía Física.

Interacción entre ondas internas de gravedad y movimientos balanceados en las Corrientes Limítrofes Orientales

Resumen aprobado por:

Dr. José Gómez Valdés	Dr. Héctor Salvador Torres Gutiérrez
Codirector de tesis	Codirector de tesis

Los movimientos balanceados (MB) y las ondas internas de gravedad (OIG) representan la mayor parte de la energía cinética (EC) en el océano. Dentro de las Corrientes Limítrofes Orientales (CLO), la energía cinética de las OIG es aproximadamente del mismo orden de magnitud que la de los MB, especialmente en verano, por lo que su interacción energética se torna de interés. En esta tesis, presentamos primero la implementación de un filtro dinámico que separa ambos regímenes, aplicado a la salida de una simulación global realista de alta resolución (LLC4320) para los meses de verano e invierno (2012). La partición MB-OIG resultante nos permitió desarrollar expresiones matemáticas para la evolución de la EC total en el dominio de los MB, y para el intercambio de energía cinética entre MB y OIG promovido por el estrés que las OIG ejercen sobre el régimen de MB. Este intercambio, aunque aproximadamente un orden de magnitud más pequeño que la evolución de la EC total, se encontró que es estadísticamente significativo y puede analizarse sobre datos que resuelven las escalas de las IGW.

Palabras clave: corrientes limítrofes orientales, interacción energética, ondas internas de gravedad, movimientos balanceados, modelos globales

Abstract of the thesis presented by César Antonio Pérez Quintana as a partial requirement to obtain the Doctor of Science degree in Physical Oceanography.

Interaction between internal gravity waves and balanced motions in the Eastern Boundary Currents

Abstract approved by:

Dr. José Gómez Valdés	Dr. Héctor Salvador Torres Gutiérrez
Thesis Co-Director	Thesis Co-Director

Balanced motions (BM) and internal gravity waves (IGW) account for most of the kinetic energy (KE) in the ocean. Within the Eastern Boundary Currents (EBC), IGW kinetic energy is about the same order of magnitude as BM, particularly in summer, hence its energetic interaction with BM is of interest. In this thesis, we first outlined the implementation of a dynamical filter that separates both dynamical regimes, and applied it to the output of a high-resolution, realistic, global simulation (LLC4320) for the summer and winter months (2012). The resulting BM-IGW partition allowed us to develop a mathematical expression for the total KE budget in the BM domain, including the KE exchange between BM and IGW promoted by a effective stress that IGW exert on the BM regime. This exchange, although about an order of magnitude smaller than the total KE budget, was found to be statistically significant to be considered in data that resolve IGW scales.

Keywords: eastern boundary currents, energy exchange, internal gravity waves, balanced motions, global models

Dedication

A Elsy, mi compañera de vida

Acknowledgements

Al Centro de Investigación Científica y de Educación Superior de Ensenada, Baja California, por brindar el espacio, los recursos y las condiciones para realizar esta investigación.

Al Consejo Nacional de Humanidades, Ciencia y Tecnología (CONAHCYT) por brindarme el apoyo económico para realizar mis estudios de doctorado.

A mis directores de tesis José Gómez Valdés y Héctor Salvador Torres Gutiérrez, por su apoyo y guía en el plantemiento y desarrollo de esta tesis, siempre tomando en cuenta mis ideas y estilo de trabajo.

A los miembros de mi comité de tesis Nicolás Gilles Rascle, Jorge Vázquez Cuervo, Juan Manuel López Mariscal y Jesús Favela Vara, por sus preguntas, aportaciones y sugerencias.

Al Consejo de Posgrama de Posgrado de Oceanografía Física, por otorgarme el plazo y apoyo económico adicionales para la finalización de este trabajo.

A los miembros del laboratorio de Corrientes Limítrofes Orientales, por su continua retroalimentación en los jueves de academia.

A mis compañeros y profesores de cursos, que me ayudaron a crecer con sus conocimientos y largas discusiones académicas.

Al personal del posgrado en Oceanografía Física, por mantenerlo funcionando para poder tomar clases, seminarios, y reuniones.

Al personal de biblioteca, que me facilitó de manera oportuna material bibliográfico y apoyo en la revisión de este documento.

Table of contents

List of figures

Figure Page

Figure Page

List of tables

Chapter 1. Introduction

The main Eastern Boundary Currents (EBC, henceforth) are the four large-scale oceanic currents located along the eastern edges of the ocean basins, forming part of the subtropical gyres (Wooster & Reid, 1963). Specifically, we refer to the California, Peru–Chile, Canary, and Benguela currents. Such currents are characterised by the presence of coastal upwelling, which brings nutrient-rich deep waters to the surface. This upwelling supports high primary production, leading to increased biomass in higher trophic levels, including commercially important fish species; in fact, according to Chavez & Messié (2009) and Fréon et al. (2009), the four major EBC contribute up to about 20% of the world's marine fish catch.

In addition to being highly productive regions in terms of fishery, the EBC are also interesting because they share geographical and, therefore, physical characteristics. For example, since subtropical gyres have a clockwise direction in the northern hemisphere and counterclockwise in the south, the EBC carry cold water toward lower latitudes. Also, as wind follows a similar circulation pattern, and due to the effect of Earth's rotation, its flow along the coast produces upwelling that brings cold, nutrient-rich water to the upper layers.

Satellite altimetry has provided invaluable global oceanographic information for over 25 years, offering unprecedented coverage of sea surface height (SSH) that cannot be achieved through any other observational method. The main feature that distinguishes satellite altimetry from more localised methods is its relatively low spatial resolution, which limits the study of oceanic phenomena to mesoscale features (on the order of 100 km) or larger, and only allows for the measurement of surface marine variables. However, recent advancements in satellite technology and projects in development aim to achieve spatial resolutions close to 15 km (Fu & Ferrari, 2008), opening up a new frontier for oceanographic studies with improved resolution. This enhancement will allow researchers to study ocean dynamics on a broader range of scales and investigate the interactions between these scales more effectively. As a result, large areas of interest, such as the EBC, can be studied even to the submesoscale regime, leading to a more comprehensive understanding of their underlying physical processes and impacts on global climate patterns.

In order to fully capitalise on these global observations, it is crucial to be well-equipped to read and interpret data with such spatial and temporal resolution. To this end, outputs from high-resolution global numerical models, such as MITgcm, provide invaluable information on various variables of interest (see, for example, Torres et al. (2018)). This has motivated a novel line of research that aims to study oceanographic observations at a global scale by partitioning the ocean into small regions and conducting spectral analysis on each region, in time and space (i.e., frequency and wavenumber), for each physical variable (velocity components, divergence, vorticity, temperature, SSH, etc.). This approach enables us to address questions about the similarities between regions comprising the same current, their collective and individual seasonal behaviour, their energy pathways, among other topics.

Our study will cover the four major Eastern Boundary Currents. Specifically, the square areas shown in 1 represent the study areas for each of the EBC, contained in the California Current (North Pacific, from 24.17 °N to 50.26 °N), the Canary Current (North Atlantic, from 13.8 °N to 33.76 °N), the Peru–Chile (South Pacific, from 42.55 °S to 13.7 °S) and the Benguela Current (South Atlantic, from 29.1 °S to 8.32 °S). The specific (latitude, longitude) locations of each quadrangular area can be found on Table 1.

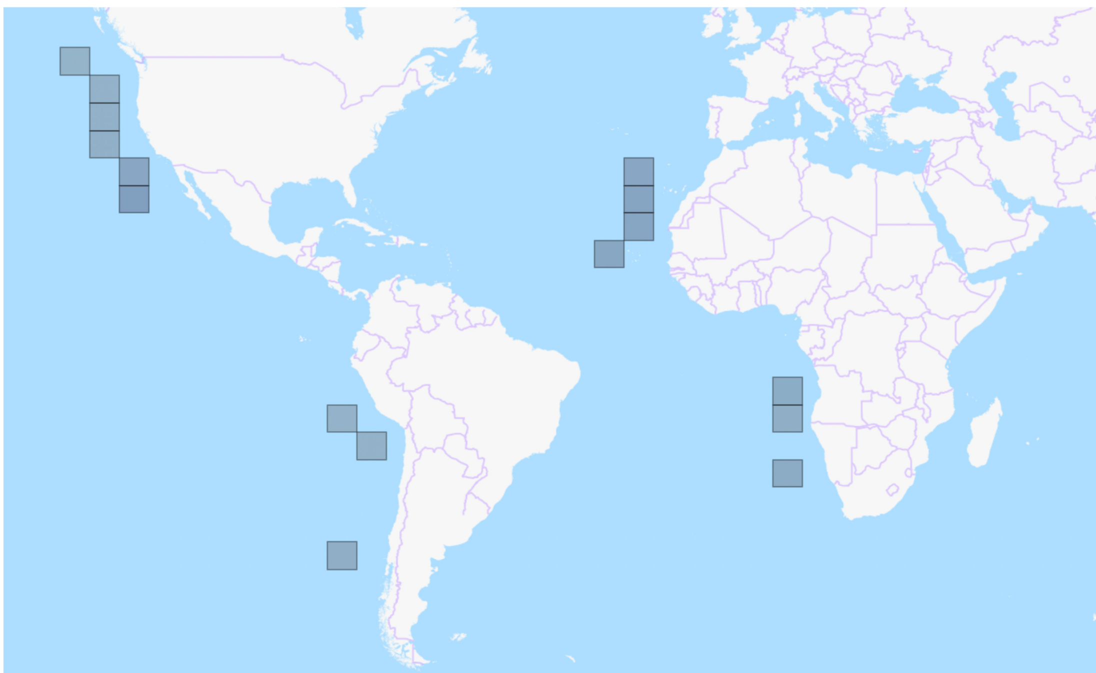

Figure 1. Study areas within each of the Eastern Boundary Currents: California (North Pacific, from 24.17 °N to 50.26 °N), Canary (North Atlantic, from 13.8 °N to 33.76 °N), Peru–Chile (South Pacific, from 42.55 °S to 13.7 °S), and Benguela (South Atlantic, from 29.1 °S to 8.32 °S). Each tile in the map represents a quasi-quadrangular area of ~ 6 ° side. Specific (latitude, longitude) locations of each quadrangular area can be found on Table 1

.

In this section, we present some aspects of what is currently known about the EBC, their similarities and differences. Later, the set of data that is intended to be used to study these currents is described, as well as some of the phenomena that can be studied for the given spatial and temporal resolution. Finally, some relevant physical aspects of energetic interactions between internal gravity waves (IGW) and balanced motions (BM), in particular how these two classes of motions exchange kinetic energy.

1.1 Background

The physical process that most characterises the Eastern Boundary Currents is the presence of coastal upwelling, which play a crucial role in the fishing activity in these regions, as they bring nutrients that nourish the lower levels of the marine trophic chain (Fréon et al., 2009; Chavez & Messié, 2009). These upwellings are generated by the winds blowing predominantly along the coast towards the equator, resulting in Ekman transport of surface waters from the coast to the open ocean (Price et al., 1987; Talley et al., 2012). In addition to these common characteristics, EBC, located on the eastern margins of the two major oceans, contain trapped coastal waves (Hill et al., 1998; Gutiérrez et al., 2014; Illig & Bachèlery, 2019), which are a combination of Kelvin waves and barotropic continental shelf waves (Connolly et al., 2013).

Beyond the continental shelf, a phenomenon that has recently garnered attention, through the use of both observations and numerical models, is the energy difference in eddies in the presence and absence of internal waves (Dunphy et al., 2017; Qiu et al., 2017; Huang et al., 2018; Klein et al., 2019). Consequently, we are interested in studying the energetic pathways between internal gravity waves (IGW) and balanced motions (BM) dynamical regimes. Although we could just use the terms *direct cascade* to refer to the energy transfer from BM to IGW, and *inverse cascade* to make reference to energetic transference from IGW to BM, we will refrain from doing so to avoid confusion and, primarily, because in this case there is no specific *large* and *small* scale when we compare BM to IGW.

Balanced motions cover most large, slow phenomena in the ocean like mesoscale eddies or large jets. They arise from the balance between two or more forces from 2-D momentum equation in the horizontal plane

$$f\hat{k} \times \mathbf{u} = -\frac{1}{\rho}\nabla p + \mathbf{Fc}, \tag{1}$$

where the left hand side contains the Coriolis acceleration, whereas the pressure gradient acceleration ($\sim \nabla p$) and the centrifugal force. Depending on the combination of forces is the balance that arises: geostrophic balance (Coriolis and pressure gradient), cyclostrophic balance (pressure gradient and centrifugal), inertial balance (Coriolis and centrifugal), or wind-gradient balance (Coriolis, pressure gradient and centrifugal). By considering additional terms to the motion equation 1 quasi-geostrophic (QG) dynamics enable us to describe submesoscale balanced motions such as fronts and filaments.

Internal gravity waves (IGW), on the other hand, exist within the interior of a stratified ocean, as they form at the interfaces between layers of water with different densities, typically caused by differences in temperature or salinity. Unlike balanced motions, IGW oscillate around their equilibrium state, governed by the force of gravity acting on density differences, also called buoyancy force that acts . In its linear approximation, for a continuously stratified fluid whose density varies with depth (i.e. $\rho = \rho(z)$), the vertical displacement occurs at the buoyancy frequency, also called the Brunt–Väisälä frequency

$$N = \sqrt{-\frac{g}{\rho}\frac{\partial \rho}{\partial z}}, \tag{2}$$

with stable, oscillating solutions appear when water density increases with depth (i.e. $\partial\rho/\partial z < 0$) which, by setting zero vertical speed component at the surface and bottom, it gives place to the dispersion relation for constant N

$$\omega_n^2(k_h) = \frac{N^2 + f^2(n\pi/k_h H)^2}{1 + (n\pi/k_h H)^2} \tag{3}$$

where f is the Coriolis parameter, k_h is the horizontal wavenumber, and n ($n = 1, 2, 3...$) is the IGW *normal mode*. The dispersion relation constraints the IGW frequencies between the range $f \leq \omega \leq N$, this is why we typically classify them as *fast motions*. When internal gravity waves break, similar to the way surface waves break along a beach, they can cause significant mixing of the ocean layers. This mixing contributes to the distribution of heat, salt, and nutrients throughout the ocean, and can even have effects on larger scale ocean circulation patterns and climate dynamics.

In this work, we intend to study in detail the dynamics of the four main Eastern Boundary Currents using high-resolution models that encompass various spatial and temporal scales. Our goal is to ultimately understand the similarities and differences between these currents, as well as the energy exchanges that occur between IGW and BM. To this end, we will first present a brief overview of the EBC and their similarities and differences. Then, we will describe the data that will be used to study these currents, as well as the phenomena that can be studied for the given spatial and temporal resolution. Finally, we will outline some relevant physical aspects of kinetic energy exchanges between IGW and BM, serving as the main motivation behind this work.

1.2 How similar are EBC when energetic interactions come into play?

Gill (1982) points out that, although EBC share several common characteristics, they have not been described by a single overarching theory. On the other hand, some recent studies (Mackas et al., 2006; Chavez & Messié, 2009) have demonstrated that these currents are not as similar as previously thought. Among the main differences is the topography, with the Pacific currents (California and Humboldt) generally having a narrower continental shelf than the Atlantic currents (Benguela and Canary). Another key difference is the influence of El Niño and La Niña in the Pacific, which is strong enough to alter fishing production and precipitation in areas near the EBC, while the Atlantic experiences the smaller magnitude and impact Benguela Niño (Mackas et al., 2006). Thus, it is essential to find a quantitative approach to characterise their similarities and differences, which will serve as a foundation for improving our understanding of these currents.

Submesoscale ocean processes occur at horizontal scales between approximately 1 and 10 kilometres and vertical scales between around 10 meters and 1 kilometre. These processes include phenomena such as ocean fronts, vortices, and filaments, which are smaller in scale than mesoscale ocean circulation but larger than microscale turbulence.

Energy transfer at the submesoscale level takes place through several processes. One key mechanism is the conversion of potential energy associated with horizontal density gradients into kinetic energy in the form of submesoscale currents and eddies. This process, known as frontogenesis, can be driven by various factors, including wind, tides, and buoyancy forces. Another significant mechanism of energy transfer at the submesoscale is the conversion of kinetic energy associated with large-scale ocean currents into internal wave energy; this process, known as current-induced internal wave generation, occurs when a large-scale current encounters a density gradient, such as a thermocline or pycnocline.

This thesis work will focus on the latter, as the kinetic energy of internal gravity waves and balanced motion in the EBC are of roughly the same order of magnitude, contrasting with more energetic regions such as the Gulf Stream or the Kuroshio extension, where the kinetic energy of IGW is significantly smaller than that of BM. Our analysis will shed some light on how BM and IGW exchange kinetic energy in the EBC, through a formulation based on the Reynolds-averaged Navier-Stokes Equations (RANS).

1.2.1 Analysing energetic interactions with high-resolution data

Energy-wise, balanced motions and internal gravity waves represent around 80% of the ocean's kinetic energy (Klein et al., 2019). In addition, it has recently been shown that there is an energy exchange between mesoscale, submesoscale, and internal waves, through direct and inverse energy cascades (Klein & Lapeyre, 2009; Barkan et al., 2017; Chereskin et al., 2019) (see Fig. 2). In the direct cascade, chaotic advection generates density fronts at the submesoscale level, which translates into an alteration in potential energy, which in turn turns into vertical density flows. In the inverse cascade, much of this kinetic energy is returned to mesoscale eddies. Studying these phenomena will only be possible with higher-resolution simulations and observations, as it involves small (submesoscale BM) and fast (IGW) motions.

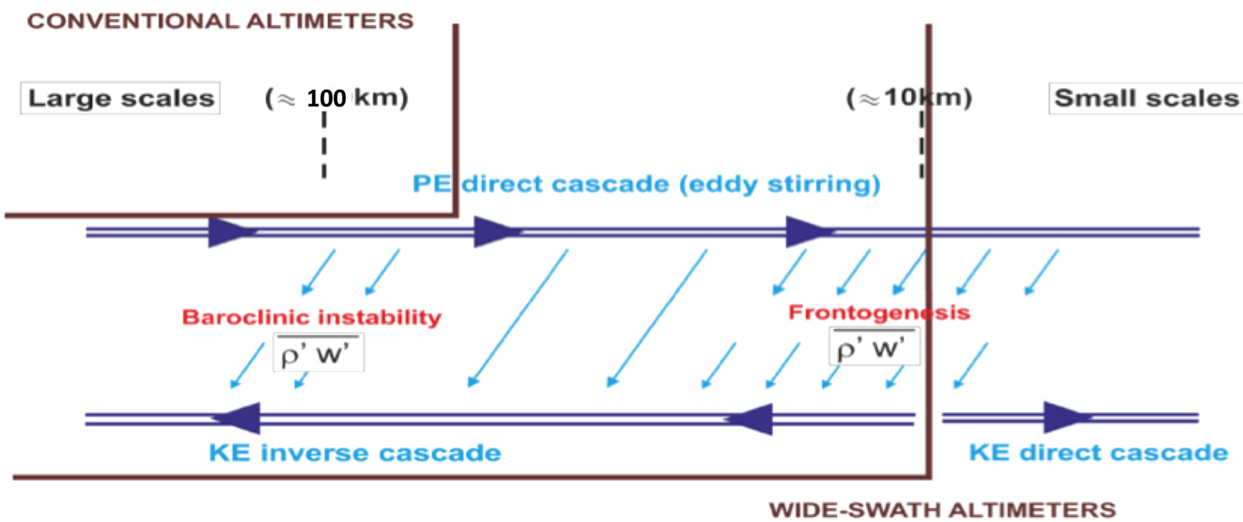

Figure 2. Schematic of energy route involving mesoscales and submesoscales. The direct (large-to-small scale) and inverse (small-to-large scale) cascades are portrayed. Reference to the maximum resolution available by observations taken with current and future satellite altimeters. Taken from Klein et al. (2019), Fig. 9.

Previously Qiu et al. (2018) and Chereskin et al. (2019) were able to determine a *horizontal transition scale* that separated the motion into mesoscale and submesoscale, that depends on the season and study area. Such criterion enables us to study the energy exchange between mesoscale and submesoscale motions. However, since BM and IGW cannot be split by horizontal scale, the application of this technique will not allow us to study the energy exchange between IGW and BM. In order to do so, we will have to come up with a refined method to separate them, which is not a trivial task. If such separation exists, we can build an analogy between the meso-to-submesoscale energy cascade and the energy exchange between IGW and BM.

1.3 Hypothesis

The equation of motion for the flow for an incompressible, two-dimensional, rotating fluid can be written as:

$$\frac{\partial u_i}{\partial t} + u_j \frac{\partial u_i}{\partial x_j} + \epsilon_{i3k} f \hat{e}_3 u_k = X_i - \frac{\partial \phi}{\partial x_i} + \nu \frac{\partial^2 u_i}{\partial^2 x_j} \tag{4}$$

where u_i is the i-th component of the velocity vector $\mathbf{u}$, f is the Coriolis parameter, X_i the i-th component external force vector F_i divided by the density ρ, ϕ is the dynamic pressure P/ρ_0, $\rho = \rho_0 + \rho\,(x, y, z, t)$ is the density, and $\nu = \mu/\rho$ is the kinematic molecular viscosity. Also, we use the permutation tensor ϵ_{ijk} to write the i-th component of the vector product $\hat{k} \times \mathbf{u}$, where $\hat{k} = \hat{e}_3$ is the unitary vector in the vertical direction pointing outwards the ocean surface.

Our hypothesis states that we should be able to separate u_i, X_i, ϕ and the equations of motion into their BM and IGW contributions:

$$\begin{aligned} \mathbf{u} &= \mathbf{u}_B + \mathbf{u}_W, \\ X &= X_B + X_W, \\ \phi &= \phi_B + \phi_W, \\ KE &= KE_B + KE_W, \end{aligned} \tag{5}$$

where the subscripts B and W stand for the balanced motions and internal waves parts of the motion, respectively.

This decomposition, if possible, would allow us to build a mathematical framework to describe the kinetic energy exchange between IGW and BM.

1.4 Research objectives

The following presents the overall objective of this study, which will subsequently be broken down into specific objectives that will help achieve the overall goal.

1.4.1 Main objective

The objective of this study is to contribute to the current understanding of the dynamics of eastern boundary currents at different scales, specifically by analysing the energetic interactions between internal waves and balanced motions.

1.4.2 Specific objectives

The work required to achieve the main objective in this thesis work can be divided into 2 main tasks or objectives:

- Be able to isolate internal gravity waves from balanced motions, considering the kinetic energy for both dynamical regimes have similar orders of magnitude in the EBC.
- Analyse the kinetic energy exchange between balanced motions and internal gravity waves for all the EBC.

Chapter 2. Data and methods

2.1 LLC4320: A realistic, high-resolution, global simulation

As mentioned earlier, understanding the results provided by future satellite observation missions is essential, and the increase in numerical model resolution necessitates higher-resolution observations to validate theories and models that enhance our comprehension of the ocean. Specifically, the primary data source of our research is the output from the LLC4320 global ocean simulation, which utilises the MITgcm (Massachusetts Institute of Technology general circulation model). LLC4320 is high-resolution simulation run with 24 s steps, on a $1/48$ ° horizontal grid spacing, 90 vertical levels with $\mathcal{O}(1m)$ resolution in the top 100 m (and up to $\mathcal{O}(100m)$ down to the bottom), and spans 14 months from mid September 2011 to mid November 2012, with hourly snapshots available.

The LLC4320 simulation is initialised with the ECCO2 (Estimating the Circulation and Climate of the Ocean, Phase II) estimation with horizontal spatial resolution of $1/6°$ (Menemenlis et al., 2008), whose output is taken to gradually increase the resolution by factors of 2, first to run the LLC1080 ($1/12°$) simulation, then LLC2160 ($1/24°$) and finally to LLC4320 ($1/48°$). The setup of the LLC4320 is similar to the ECCO initial execution, but the main difference is that LLC4320 is a free-run simulation with 16 tidal constituents as forcing, and fields from the ECMRWF (European Centre for Medium-Range Weather Forecasts) 6-hour atmospheric model analysis as boundary conditions at the upper surface that include winds, air temperature and humidity, precipitation, short and long wave radiation.

Such features allow LLC4320 to be used as a realistic, high-resolution, global simulation. The numerical settings of LLC4320 include a flux limited, seventh-order, monotonicity-preserving advection scheme (Daru & Tenaud, 2004) and the modified Leith scheme of Fox-Kemper & Menemenlis (2008) for horizontal viscosity; also vertical viscosity and diffusivity are parameterised according to the K-profile pasteurisation scheme (Large et al., 1994).

Since $1/48$ ° horizontal spacing is equivalent to approximately 2 km at mid-latitudes, numerical diffusion implies the effective resolution of the model is around four times the grid size (~ 8 km) (Rocha et al., 2016; Erickson et al., 2020), which is enough to capture submesoscale processes in the upper ocean, at least to a certain extent. Theses submesoscale processes are responsible of the transport of heat and tracers, and also of the non-linear interactions with waves, thus playing a crucial role for our analyses.

For this study, we aimed to compare the dynamics of EBC during winter (January, February, March) and summer (August, September, October) months. We used hourly snapshots of LLC4320 for these months to examine the vorticity features of the EBC, resulting in around 2200 snapshots for each variable (e.g., U, V, θ) and season.

Data can be accessed either by directly downloading from the ECCO Data Portal (see: `https://data.nas.nasa.gov/ecco/data.php?dir=/eccodata/llc_4320`) or by reading them using the xmitgcm Python package (see: Abernathey et al. (2021), `https://github.com/MITgcm/xmitgcm`).

The first major advantage of this simulation is that it covers a large percentage of the ocean and two seasons with dynamics that are in principle different, even opposite in many scenarios. The second feature is that, due to its range of spatial and temporal scales, it allows us to analyse the energy contribution of internal gravity waves and balanced movements for each of these regions. This second particularity helps us to detect non-linear interactions between different scales, as non-linearity spreads kinetic energy across the BM side of the spectrum, but more importantly near the submesoscale balanced motions (SBM) part of the spectrum 3, as they tend to interact more with the IGW nearby.

From the analysis of these energy spectra, it has been discovered that the relationship between balanced movements (in the sub- and mesoscale ranges) and internal gravity waves varies seasonally and from one region of the ocean to another (Qiu et al., 2018; Chereskin et al., 2019), by simply defining a transition scale between both classes of movements. These measurements based on transition scales gives us a first hint about the type of physical variables that we can consider to find dynamic differences in the different EBC.

2.2 Data preprocessing

After downloading all the variables for our study, it was necessary to merge them into data collections that hold the information for each study area and season. Since managing and performing calculations over each of these collections would not be scalable beyond the short term, we used the Dask Python package along with xarray; the former is a library that facilitates the creation of parallel calculations, with array functions similar to what numpy offers, while the latter takes Dask variables and gathers them into data structures that are netCDF-friendly, and at the same time takes advantage of its *lazy evaluation scheme* (i.e., it only reads data when it is required) to optimise memory consumption (Rocklin, 2015; Hoyer & Hamman, 2017).

Overall, our workflow is as follows:

1. Download hourly snapshots for each variable, area, and season.

2. Combine hourly data into time series for each variable, area, and season, then store the combined variables into a single dataset per area and season.

3. Compute derived quantities (i.e., KE, RV and DIV, averages) for further analyses, allowing us to explore patterns related to ocean dynamics.

4. Calculate dynamical filter in 3D ω-k_h spectral space, based on the estimated dispersion relation of the 10*th* IGW baroclinic mode for each area, which allows us to separate energy contributions from different oceanic scales. More details on the dispersion relations and the filter design will be provided in Chapter 3.

5. Once filtered into its BM and IGW components, estimate the kinetic energy exchange between these two dynamical regimes. The theoretical framework and results will be described in Chapter 4.

2.3 ω-k_h spectra

For a given variable $\phi(x, y, t)$ (e.g., kinetic energy, sea surface height), season (summer or winter), area (tiles in Fig. 1), by performing a Fast Fourier Transform, we obtained the 3D power spectral density (PSD) in the wavenumber (k, l) and frequency (ω) domains, $\Phi(k, l, \omega)$. A close examination of $\Phi(k, l, \omega)$ on the k–l plane confirmed that they are mostly azimuthally symmetric for all frequencies, so we were able to map the k–l plane into a horizontal wavenumber k_h; hence, the azimuthally averaged spectrum $\Phi(k_h, \omega)$ was produced.

An example of such isotropic 2D spectra in the $\omega - k_h$ space is shown in Fig. 3, and the temporal and spatial reference scales are also displayed. An estimation of the average local buoyancy frequency N, along with the average depth H at each area of interest, were used to calculate the dispersion relation curves corresponding to the first four and the tenth vertical modes of the IGW of Eq. 3. As we can see in Fig. 3, the estimation we did for N and H is good enough to reproduce the dispersion relations (dotted lines) for the first 4 modes in the spectral domain, so that we used the same estimation to calculate the dispersion relations for the 10th mode (black dashed line), which is the highest mode the LLC4320 simulation can resolve, although not visible in the spectra we analysed.

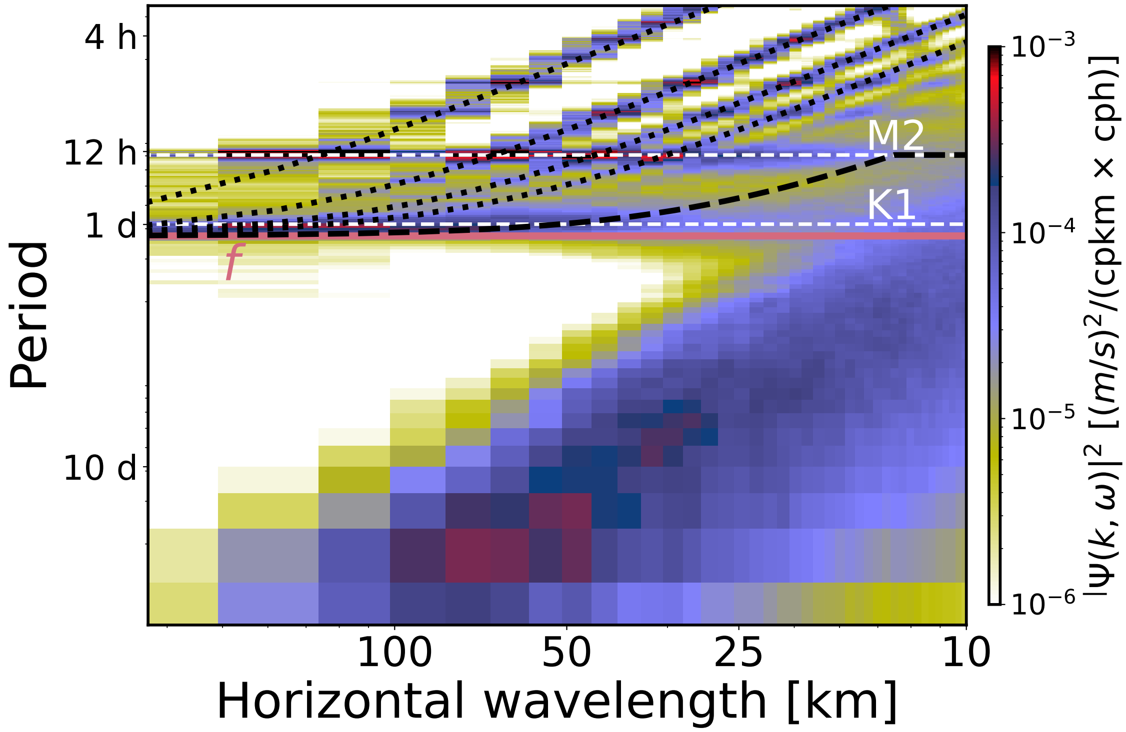

Figure 3. Power spectral density (PSD) of the surface kinetic energy (KE) in the frequency–horizontal wavenumber (ω–k_h) domain for the area centred at 26.64 °N within the Canary current during the winter (January, February, March) of 2012. The black dotted lines represent dispersion relations for modes 1, 2, 3, and 10 of the internal gravity waves. The black dashed line denotes the minimum frequency between the internal gravity waves (IGW) at mode 10 and the M_2 tide, whereas the white dashed lines mark the M_2 and K_1 tide frequencies for reference purposes. The solid dark pink line corresponds to the average Coriolis frequency f in that area (Chereskin et al., 2019). The PSD is presented in its variance-preserving form (i.e. multiplied by ω and k_h) since the plot axes are log-log scaled.

2.4 Comparing different EBC

Since there are instances where we need to compare our results and findings among the different EBC, and we have a total of 16 $6^\circ \times 6^\circ$ areas, comparing them side by side becomes considerably hard, in particular when the comparisons need to show snapshots of the fields for summer and winter. Our results and figures provide comparisons between areas centred at the same latitude whenever possible, so the effect by Earth's rotation is the same. The areas we compared are centered at 26.64° (north or south) for the California, Canary, and Benguela currents and at 21.61 °S for the Peru–Chile current. Our results and conclusions have proved to be valid for all areas and seasons, except when we state otherwise.

Chapter 3. Partitioning motion in BM and IGW

3.1 A dynamical filter to discriminate BM from IGW

BM and IGW are known to be present in a wide and similar range of horizontal scales, whereas IGW are, in general, faster than BM. Large BM are, in general, slow and can mostly be described by geostrophic dynamics, such as eddies. However, near the submesoscale (Ro ~ 1) regime, we found submesoscale BM (SBM) with horizontal scales of up to a couple of dozen kilometres, frequencies near the local Coriolis parameter, and enclosed motions, such as fronts, gradient wind (cyclostrophic) balance, and filaments (Mcwilliams et al., 2015). Since SBM tend to have frequencies and scales similar to the IGW domain, we need to set a sensible threshold to allow us to study most SBM without interference from tides or higher IGW modes.

Thus far, a question that is key for this work is, given IGW and BM are entangled in the submesoscale regime, as seen in Fig. 3, is there a method to isolate both motion regimes, that also takes into account the local, physical features of a given region?

3.1.1 Rotational–divergent ratio in the frequency–wavenumber space

We calculated the corresponding ω-k_h kinetic energy spectral densities $KE_\zeta = \left|\hat{\zeta}\right|^2/k_h^2$ and $KE_\delta = \left|\hat{\delta}\right|^2/k_h^2$, where $\hat{\zeta}$ and $\hat{\delta}$ denote the Fourier transform of the relative vorticity and divergence fields. Figure 4 shows how the quotient of spectral densities KE_ζ/KE_δ varies by current and season, making it evident that vorticity fields dominate over a broader range of frequencies in winter than they do in summer.

By inspecting Fig. 4, we determined which temporal and spatial scales are dominant in each regime from these spectra. During summer, at periods of 1 day, both divergence and vorticity have roughly the same kinetic energy, where the ratio $KE_\zeta/KE_\delta \approx 1$. The kinetic energy for motions with periods longer than 1 day can be explained, mainly, by the divergent component (IGW); hence, in this case, $KE_\zeta/KE_\delta >> 1$ (brown colour). For motions with periods longer than one day, the vorticity component explains most of the variance (green colour). During winter, the vorticity component tends to extend towards periods of shorter than one day, particularly motions with horizontal wavelengths smaller than $\sim$ 50 km.

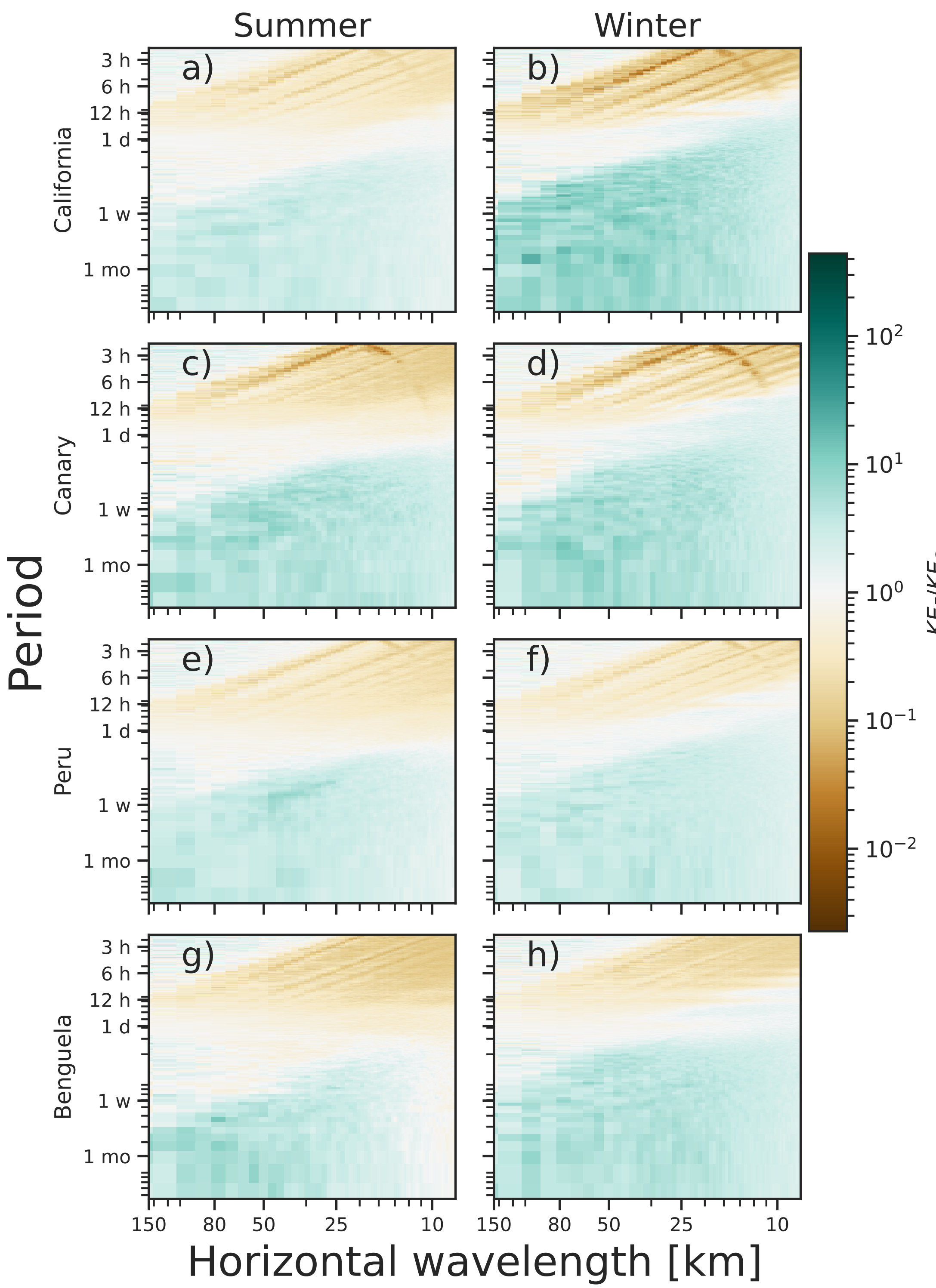

Figure 4. The quotient of spectral densities KE_ζ/KE_δ in the frequency–horizontal wavenumber domain by current and season at selected areas within the California (26.64 °N: a and b), Canary (26.64 °N: c and d), Peru–Chile (21.61 °S: e and f), and Benguela (26.64 °S: g and h) current systems. Green and orange highlight scales where either KE_ζ or KE_δ dominate, respectively.

From these spectra, one can argue that a temporal filter with a cut-off period of 1 day (or, in a more general case, the inertial period) is sufficient to discriminate BM from IGW. This procedure might work in summer, but not in winter due to the presence of submesoscale BM with periods of shorter than 1 day. It is precisely in winter that the scientific community has focused its efforts to discriminate both classes of motion. On the other hand, the implementation of a filter in the horizontal wavenumber space would rely on the definition of a *transition scale* (see, e.g. Qiu et al. (2018)), which cannot always be uniquely determined by area of study and season and also poses the challenge of choosing a dynamical criterion that suits all cases and does not depend on measurements of KE in the spectral space (which are, by themselves, sensitive to the selected time frame or method). Here, we present a dynamical filter that intends to achieve such BM–IGW separation, whose performance is assessed in the next section.

3.1.2 Choosing a dynamical cutoff frequency

The findings for the ratio of rotational to divergent components in the preceding section show that IGW and BM share the same small horizontal wavelengths and time scales as submesoscale BM, making their separation by applying a temporal or spatial filter difficult.

Chereskin et al. (2019) reported a significant contribution of IGW to ζ and δ in the California Current System, and Torres et al. (2018) reported IGW dominance in the EBC, where both studies were based on an LLC4320 simulation. In order to filter out IGW from BM, we designed a dynamical filter based on the dispersion relation of the highest IGW mode in the frequency–wavenumber ($\omega - k_h$) space. The main feature of this filter is that it does not have a fixed cutoff frequency (ω) or horizontal wavenumber (k_h), but it was thought to filter as many internal gravity waves and tides as possible. We achieved this by using a function in the $\omega - k_h$ spectral space to obtain a cutoff frequency for each k_h, $\omega_c\left(k_h\right)$.

Our candidate function was the dispersion relation for the tenth vertical normal mode ω_{10} (i.e. Eq. 3, with $n = 10$). Qiu et al. (2018) and Torres et al. (2018) used this tenth vertical normal mode to quantify the relative contributions of IGW and BM to the kinetic energy, since that one is the highest IGW mode the model can solve. As we can see in Fig. 3, this criterion does not manage to filter out semidiurnal or diurnal tides at scales below 30 km. Hence, we included an additional constraint to discard them by considering the dominant tidal band below the ω_{10} dispersion curve (M_2 in all of the cases we examined). The resulting filter is a function in the $\omega - k_h$ spectral space that obtains a cutoff frequency (ω_c) that depends on k_h in the form

$$\omega_c\left(k_h\right) = min\left[\omega_{10}, \omega_{tide}\left(k_h\right)\right], \tag{6}$$

where ω_{tide} corresponds to the frequency of the additional tidal band that needs to be discarded. The dispersion relation curve modified to discriminate BM from IGW (including M_2 tides) is represented by the black dashed line in Fig. 3.

Figure 5 better illustrates how the filter separates IGW and tides from BM in the spectral space. The actual filtering should be performed in the three-dimensional spectral space (k, l, ω) (Fig. 5, left panel), which allows the inverse FFT to be applied to the filtered signal and then go back to the physical (x, y, t) space. Therefore, BM (IGW) are found outside (inside) the paraboloid-like shape (Fig. 5, left panel) or below (above) the dispersion relation curve (Fig. 5, right panel).

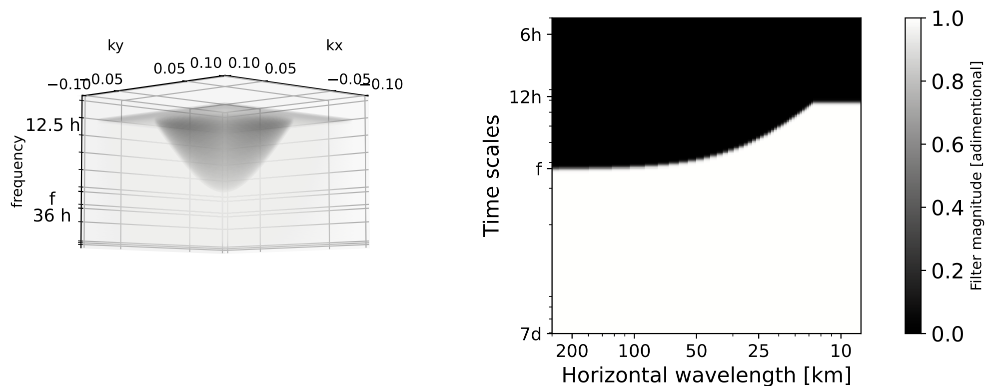

Figure 5. Dynamical filter in the k-l-ω space (left panel) and in the ω-k_h space (right panel). Internal gravity waves (balanced motions) are located inside (outside) the paraboloid-like shape in the left panel and inside the black (white) region in the right panel. The filter transfer function is given by Eq. 8.

3.1.3 Implementation of the dynamical filter

An nth-order Butterworth filter was applied in the Fourier space by transforming the input signal into the frequency domain, applying a transfer function that represents the filter, and then transforming the result back into the time domain. In general, the transfer function of an nth-order Butterworth filter in the frequency domain is given by:

$$H(\omega) = \frac{1}{1 + \left(\frac{\omega}{\omega_c}\right)^{2n}}, \tag{7}$$

where ω_c is the cutoff frequency and n is the order of the filter. The cutoff frequency represents the frequency at which the filter begins to reduce the amplitude of the input signal.

In the Fourier space, the Butterworth filter has a smooth transition from "passband" to "stopband", which means it has a monotonic behaviour with no ripples in either the passband or the stopband ends. This is one of the reasons why Butterworth filters are commonly used in many applications, such as in audio and image processing. The higher the order (n), the more the filter converges to a square (ideal) filter, without sacrificing smoothness and thus introducing less noise than the ideal filter in real-world situations where the domain is finite or the signals are not periodic.

However, the Butterworth filter also has some potential flaws. One of the main disadvantages is that it has a slow transition from the passband to the stopband, which means it requires a higher-order filter to achieve a steep transition. This can result in increased computational complexity and a higher cost in terms of both time and resources. Also, if the order is too high, since we are dealing with discrete data and spectra, the transfer function could be indistinguishable from an ideal filter, and thus introduce the noise we intend to avoid in the first place.

For our specific case, we needed to create a 3D transfer function in the Fourier space (k_x, k_y, ω) that conditions the *cutoff frequency* as a function of the isotropic wavenumber $(k_h = \sqrt{k_x^2 + k_y^2})$, as described by Eq. 6. The mathematical form of the filter in the Fourier space is the following

$$H\left(k_x, k_y, \omega\right) = \frac{1}{1 + \left(\dfrac{\omega}{\omega_c(k_h)}\right)^{2n}}, \tag{8}$$

where we note that we are not simply multiplying multiple transfer functions, one by each of the three-dimensional Fourier variables (k_x, k_y, ω), but we have a single 3D transfer function that at first glance is similar to Eq. 7; the main difference relies on the fact that the cutoff frequency ω_c depends on k_h.

The conceptualisation of the filter can be seen as layers: first, in the 1D space, we take a single k_h wavenumber which defines a 1D filter identical to Eq. 7; then, we repeat this process for all the k_h wavenumbers to build an ensemble of 1D filters, which results in the 2D filter in the ω-k_h space (Fig. 5, right panel); finally, if we rotate the filter around the ω axis, we obtain the 3D filter in the k_x-k_y-ω space (Fig. 5, left panel), so that the cutoff line that divides IGW from BM in the 2D space forms a solid of revolution in the 3D Fourier space.

Our implementation showed to be effective and introduced little distortion, except on both ends of the signal, which is expected given we did not window the input data and the domain is not periodic (i.e. data from adjacent areas differ from each other). After testing many windowing schemes, we opted for doing the FFT, then applying the filter, then inverting the FFT and then discarding the noisy ends, instead of applying a window to the data before the FFT, since the windowing process alters the overall power spectrum. In the physical space, those noisy ends represent around 3 days at the beginning and the end of a whole season ($\sim$ 90 days), and less than $0.2°$ on the southern, northern, eastern and western boundaries of each area we studied ($\sim$ $6°$ per side); this effect is more noticeable in some time series than it is on the spatial snapshots of the filtered fields.

Although we acknowledge that better implementations of the filter can be accomplished by mapping the Butterworth filter to the physical 3D (x, y, t) space, if we consider the resolution of the model output along with the window sample size, our results have been good enough to come to insightful, physically-relevant conclusions. Further optimisations must be applied should a more quantitative analysis is required.

3.2 Comparing ζ and δ at seasonal and diurnal time frames

In order to display the capabilities of the dynamical filter, we first display the *unfiltered fields* of ζ and δ in the physical space and analyse their spatial structures and the joint probability distribution functions (JPDFs) of both fields, for the winter and summer seasons. This will served as a base case for the sections below.

The rotational (ζ) and divergent (δ) components of horizontal motions were analysed, with ζ and δ being defined as $\zeta = v_x - u_y$, $\delta = u_x + v_y$, where u and v are the horizontal velocity components in Cartesian coordinates x and y, and the subscripts denote partial derivatives with respect to the subscripted variable. The relative vorticity ζ is related to the spin of horizontal motions, and the horizontal divergence δ is related to the vertical derivative of the vertical velocity via the 3D incompressibility condition. Both ζ and δ are normalized by f in the maps and timeseries shown in this thesis, which corresponds to the local inertial period. We describe the analysis of the fields of ζ/f and δ/f in the following paragraphs.

Snapshots of vorticity and divergence in summer and winter are presented in Fig. 6 as the first comparison between these two seasons. In winter, elongated positive and negative filaments with magnitudes of order 1 for ζ/f and 0.5 for δ/f dominated the vorticity and divergence fields, respectively. Additionally, small-scale cyclonic eddies were all over the space, reaching magnitudes of order 1 for ζ/f. On the other hand, internal gravity waves overshadowed balanced motions in the δ map in the summer season, whereas submesoscale BM features were weak but observable in the ζ map, compared to their winter counterpart.

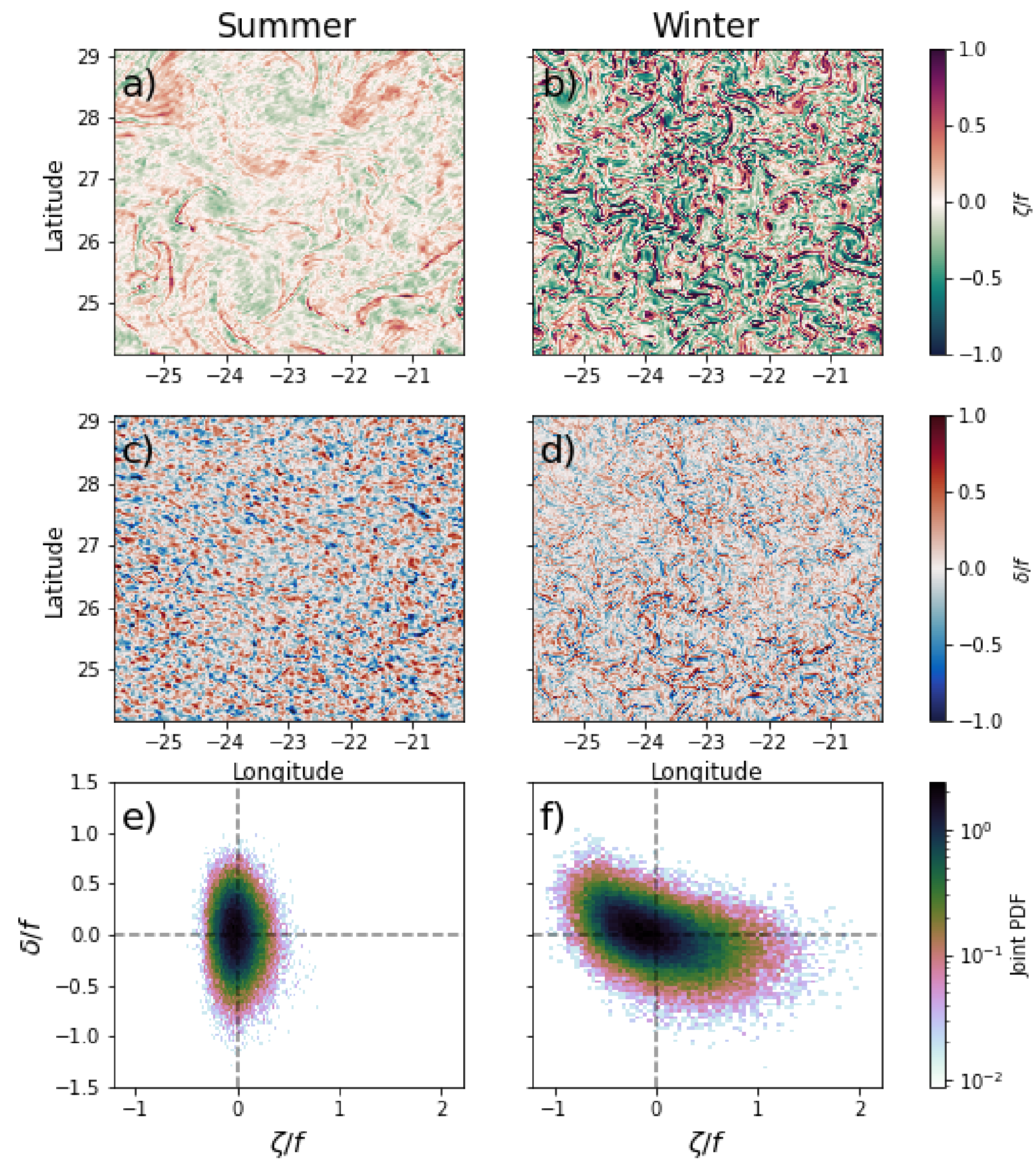

Figure 6. Snapshots of the total (unfiltered normalized) relative vorticity (ζ/f: a and b) and divergence (δ/f: c and d) fields, along with their corresponding ζ-δ joint probability distributions (e and f) at Canary (26.64 N) for summer (a, c, and e) and winter (b, d, and f) at times when the sea surface temperature was maximal (at around 17:00 local time). ζ and δ were then normalized by their Coriolis frequencies f. JPDF colours are presented on a logarithmic scale.

To compare the diurnal variations in δ and ζ, maps of vorticity and divergence can be visualised in Fig. 7, which shows snapshots at times during the same day that are near the maximum and minimum δ and ζ values. In most cases, in all EBC, the maximum divergence occurred at around 17:00 local time (end of daytime), and the minimum divergence occurred at around 05:00 local time (end of night-time), with the only differences being the intensity of these fields and the exact time at which their minima and maxima occurred. Submesoscale structures strongly emerged during the afternoon with positive skewness for vorticity ($Ro > 1$) and negative skewness for divergence. As revealed by comparing the 05:00 and 17:00 JPDF side by side, the skewness indicates that frontogenesis was more significant during the afternoon than late at night. This implies a change in the kinetic energy transfer, since small-scale motions intensified during the night.

Another point of dynamical comparison was the ζ-δ joint probability distribution of both the divergence and vorticity fields for each season and area. Figures 6 and 7, in addition to the comparison in the physical space, display their corresponding joint probability distribution functions (JPDF). Each of these instantaneous JPDF shows how one can translate dynamical differences in physical space into a JPDF that allows such differences to be described. Additionally, each of these four quadrants corresponds to different motion regimes. In particular, the higher probability densities found in the fourth quadrant (positive ζ, negative δ) and Rossby numbers ζ/f near to an order of 1 give us evidence of intense frontal activity, which is directly associated with submesoscale instabilities, such as fronts or filaments.

3.3 Separating IGW and BM

In the previous sections, we designed a dynamical filter that takes advantage of the dispersion relation of the tenth vertical normal mode limited to its maximum frequency at M_2 ($1/12.42$ h) (Fig. 5). Also, we presented the δ and $zeta$ *unfiltered fields*. In this section we apply the filter to the velocity components u and v and then calculate the corresponding ζ and δ fields. This will serve to assess the performance of the dynamical filter in extracting the features of BM and IGW.

Figure 8 serves as a visual evaluation of how the dynamical filter works. The first row shows both ζ and δ unfiltered fields for a snapshot in summer, whereas the second and third rows showcase the (ζ, δ)-BM and (ζ, δ)-IGW components, respectively. By inspecting the unfiltered fields, it is noticeable that, on one hand, ζ partially filters out IGW. Blurry elongated cyclonic filaments can be identified visually. However, eddy-like structures are unclear. Torres et al. (2018) and Torres et al. (2022) reported that the signature of internal tides and their subharmonics is non-negligible. On the other hand, the impact of IGW is overwhelming in the unfiltered δ field. The IGW dominance over BM is well known during the summer season (Qiu et al., 2018; Savage et al., 2017): δ/f is characterised by having higher values than ζ/f. This description is emphasised in the JPDF by following a vertical distribution, with δ/f values from -1 to 1, whereas ζ/f is limited from -0.5 to 0.5.

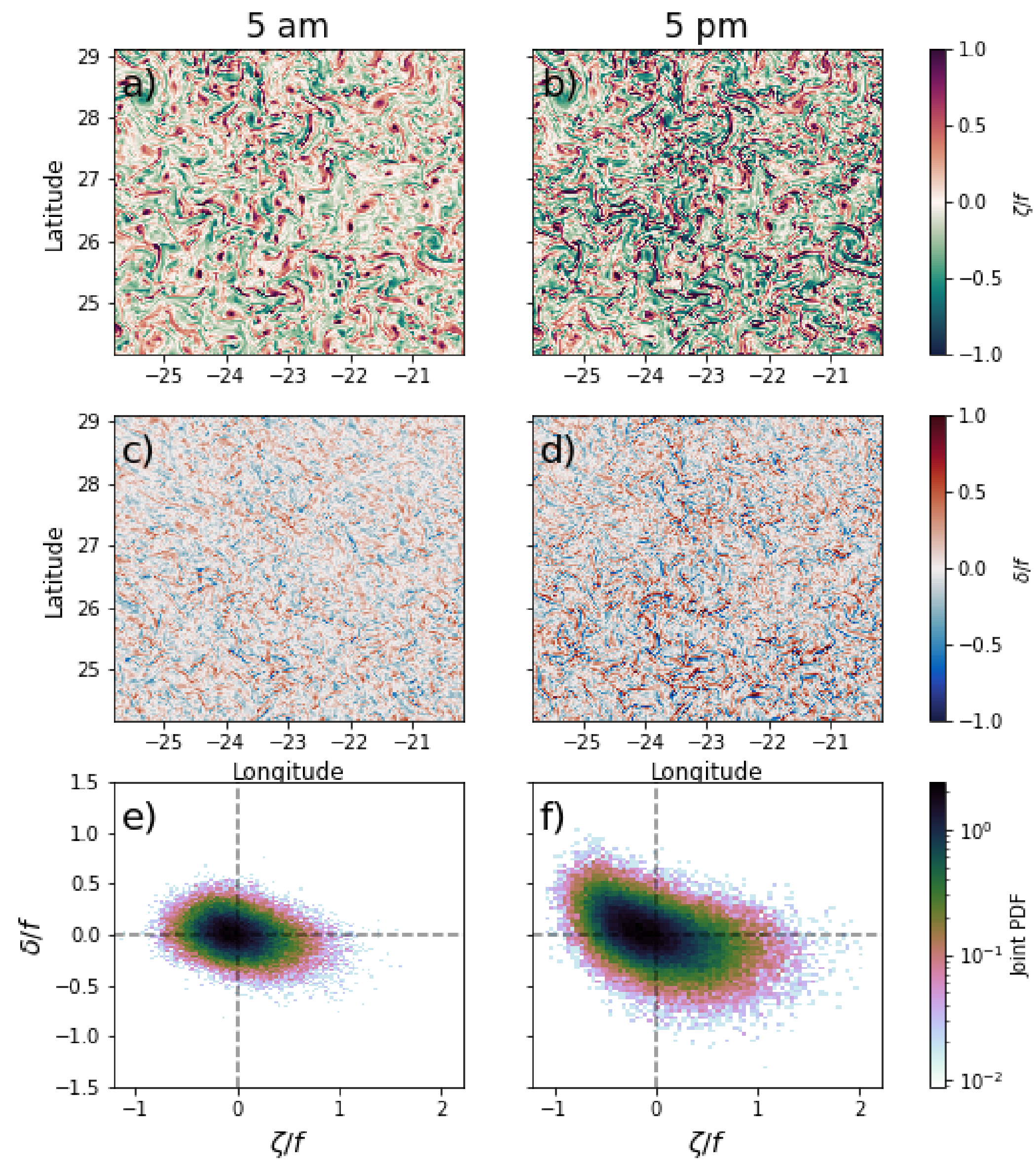

Figure 7. Snapshots of the relative vorticity (ζ: a and b), divergence (δ: c and d), and instantaneous ζ-δ joint probability distributions (e and f) at Canary (26.64 °N) for times where the sea surface temperature was maximal (at around 17:00 local time, left) and minimal (at around 05:00 local time, right) on an arbitrary day in winter (1 March 2012). JPDF colours are presented on a logarithmic scale.

This scenario changes after applying the dynamical filter. The second and third columns of Fig. 8 demonstrate that the filter manages to separate BM and IGW regimes and preserve their respective relevant dynamical features in the ζ-BM and δ-BM fields, such as mesoscale cyclonic and anticyclonic eddies and elongated fronts and filaments, with their respective dipoles in δ-BM. Additionally, the JPDF is slightly yet noticeably skewed towards the fourth quadrant, following a diagonal distribution. It is also noteworthy that the separation of BM is not sensitive to the intensity of the IGW component once the maximum cutoff frequency of the filter has been defined.

As shown in Fig. 9, the JPDF of the 4 EBC areas for the whole summer and winter seasons matches the distribution in Fig. 8, regardless of the intensity of the IGW field. As expected, we found a stronger vorticity field in winter (yielding a diagonal distribution in the JPDF), whereas divergence (primarily associated with IGW) was more dominant in summer (yielding a vertical the distribution in the JPDF). Particularly in winter, the filter allows the leakage of information from the BM to the IGW component, as revealed by the gentile diagonal component in the JPDF of IGW (fourth column in Fig. 9). This is explained by submesoscale motions with frequencies higher than the M_2 internal tides, since the dispersion relation used is limited at M_2. However, the JPDF associated with this leakage in the IGW component is three orders of magnitude smaller than the JPDF of BM.

3.4 Seasonal and diurnal variability of BM and IGW

Given that both divergence ($\delta = u_x + v_y$) and vorticity ($\zeta = v_x - u_y$) have a spatial mean of almost zero in the ocean (Shcherbina et al., 2013), the standard deviation of these quantities (S can be either ζ or δ) $\sigma\left[S\right](t)$ can be approximated by

$$\sigma\left[S\right](t) \simeq \sqrt{\frac{1}{NM}\sum_{n=0,m=0}^{N,M}\left(S_{n,m}(t)\right)^2} = RMS\left[S\right](t)\,, \tag{9}$$

thus serving as a measure of the instantaneous average intensity of these fields (Klein et al., 2019). If one calculates the standard deviation of these variables for each hourly snapshot, a time series that shows the evolution of such fields' intensity can be obtained. These two fields were examined for both the unfiltered and filtered (BM, IGW) components of the motion (Qiu et al., 2018).

We now examine the evolution of the RMS values of both ζ and δ, as per Eq. 9, for the BM and IGW regimes. These calculations are plotted along with the corresponding surface sea temperature (SST), surface net heat flux, magnitude of wind stress, and depth of the KPP boundary layer depth (KPP_{hbl}), since atmospheric forcing is known to impact the frontal dynamics through the vertical viscosity (Garrett & Loder, 1981; Dauhajre et al., 2017). We show the findings for the Canary (Fig. 10) and Benguela (Fig. 11) currents, considering that these two currents have less common features, especially in winter.

Canary has high temperature (and density) gradients and is located near a source of energetic eddies that are ejected towards the West Atlantic. The Benguela current around 26.64 °S, on the other hand, has a weaker vorticity field and is mostly dominated by internal tides generated over topographic features at the Walvis Ridge.

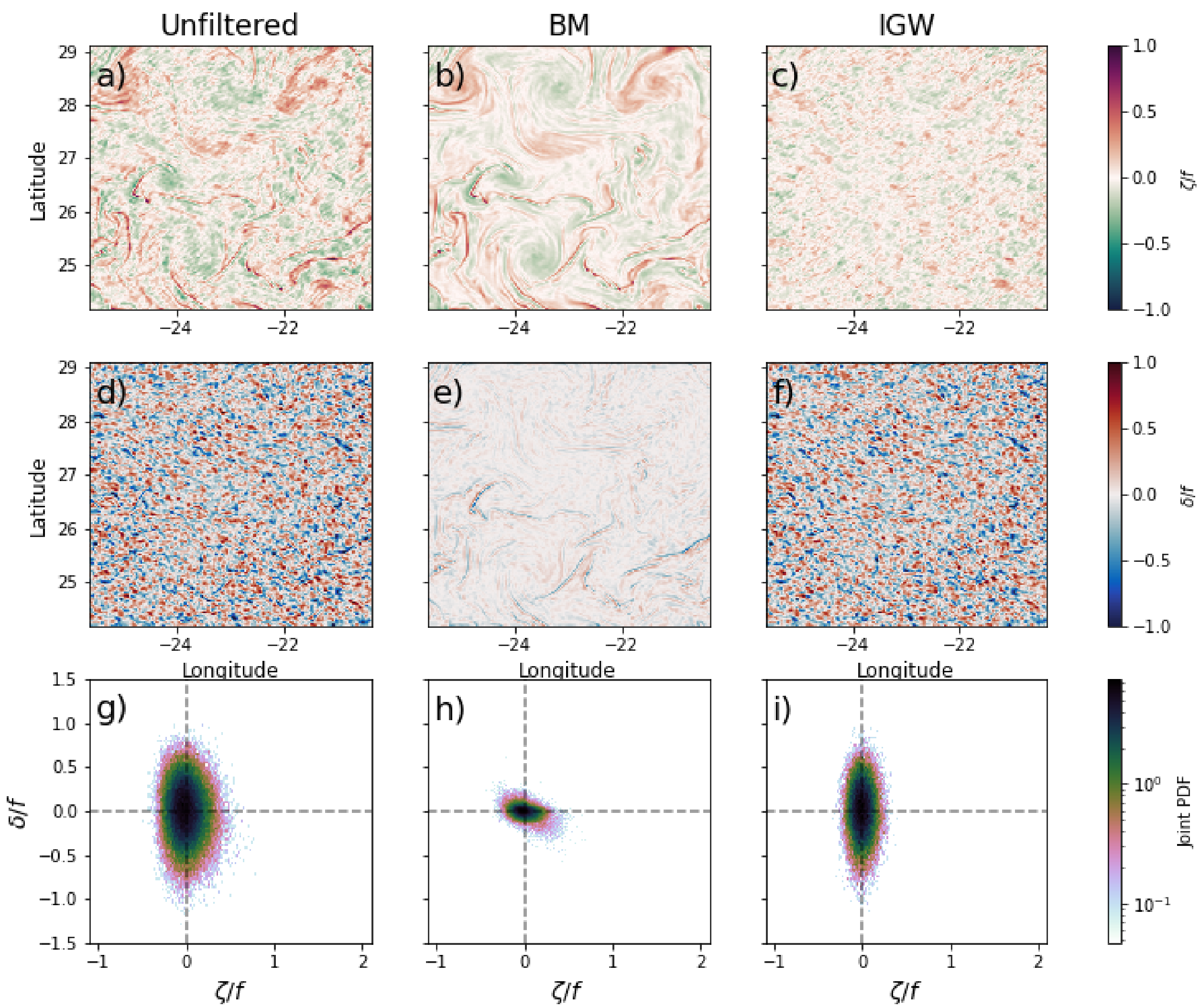

Figure 8. Snapshots of the normalized relative vorticity (ζ/f: a, b and c), divergence (δ/f: d, e, and f), and ζ-δ JPDF (g, h, and i) for a snapshot on September 30, 2012 at Canary (26.64 °N). Fields are shown in an unfiltered state (a, d, and g) as well as for the BM (b, d and h) and IGW (c, e, and i) regimes. JPDF bin colours are presented on a logarithmic scale.

The time series of RMS values of BM-ζ/f and BM-δ/f exhibits intermittency at daily to weekly time scales as well as strong seasonality (third and fourth panels in Fig. 10 and 11). In addition to the well-known seasonal variability in the KPP_{hbl} (deeper in winter and shallower in summer), high-frequency variability can be detected in Figs. 10 and 11 (top panels red line). Simultaneously, KPP_{hbl} displays a strong phase relationship with the ocean net heat flux (red line in the second row). The daily vertical excursion of KPP_{hbl} in winter can be around ~ 100 m, while in summer, this excursion gets weaker since the stratification increases during this season.

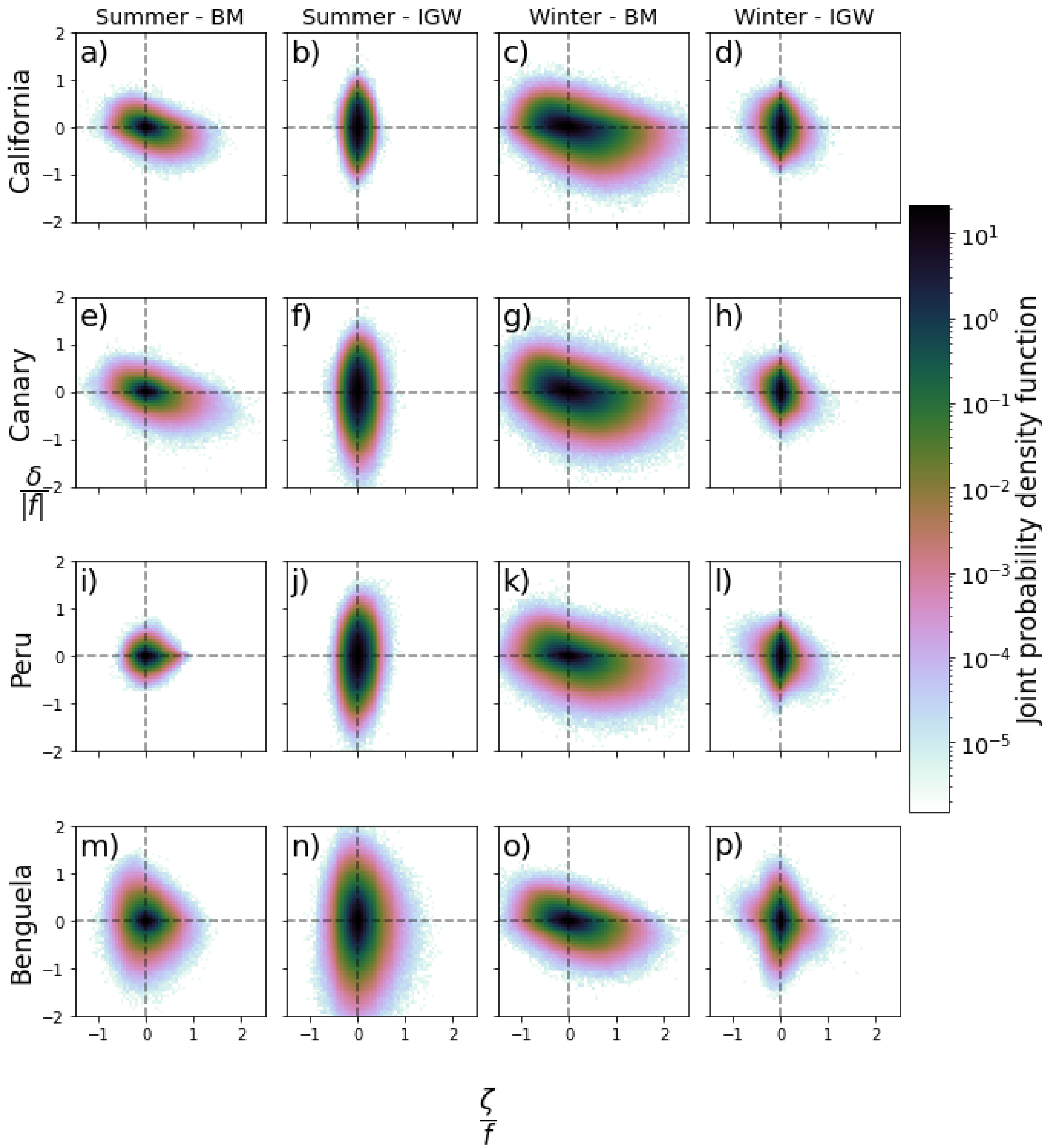

Figure 9. Joint probability distribution of ζ (x axis) and δ (y axis) at selected study areas within the California (26.64 °N: a, b, c, and d), Canary (26.64 °N: e, f, g, and h), Peru–Chile (21.61 °S: i, j, k, and l), and Benguela (26.64 °S: m, n, o and p) current systems for both the balanced motion (BM) and internal gravity wave (IGW) regimes. Both vorticity (ζ) and divergence (δ) are normalized by f. Bin colours are presented on a logarithmic scale.

The intensity of the δ and ζ fields in the BM regime follow the seasonal and diurnal variability of KPP_{hbl}. During winter, when KPP_{hbl} reaches its maximum depth (around $250\ m$ in the Canary Current and $150\ m$ in the Benguela Current), the overall RMS values of ζ and δ increase and the high-frequency variability is intense, such that the RMS values of both BM-δ and BM-ζ increase and decrease drastically at diurnal time scales. From early spring to late summer, the diurnal pattern weakens (even vanishes), as revealed by a reduction in the amplitude of the diurnal variability (see panel g and the final part of panel h in Figs. 10 and 11). This dampening of the diurnal cycle follows the shallowness of KPP_{hbl}. The diurnal excursion of KPP_{hbl} in summer is from 5 m to ~50 m.

Regarding the IGW-ζ and IGW-δ time series, it is remarkable that the diurnal cycle is negligible, in both summer and winter. However, we should remark that dynamical filter is not 100% accurate. A comparison of panels f and h on both Figs. 10 and 11 indicated that there is leakage of high frequency BM onto the IGW component, which is more noticeable during the winter when the RMS values of BM-ζ (pink lines) are large. This is consistent with the IGW-ζ-δ JPDFs in Fig. 9, which shows a slight tendency towards the BM regime (fourth quadrant: positive ζ and negative δ) near $Ro \sim 1$, although their JPDFs are three orders of magnitude smaller than those of their BM counterpart.

Figures 10 and 11 illustrate the synchronisation of the RMS values of BM-ζ and BM-δ with KPP_{hbl} and the ocean net heat flux. Garrett & Loder (1981) described that vertical viscosity forces are an effective divergent flow, δ_κ, that further stimulates frontogenesis. A simple scaling analysis was conducted, following Garrett & Loder (1981) and assuming that the vertical viscosity κ was constant in space, which led to

$$\frac{f}{\kappa}\delta_\kappa \approx \zeta_{zz}, \tag{10}$$

with Δ representing the horizontal Laplacian operator and b representing the buoyancy. This equation means that, through the modulation of the vertical viscosity, the wind intermittency and the diurnal cycle of surface heat fluxes impact the divergence and relative vorticity of BM. In our case, we did not have access to κ, but we show the time series of KPP_{hbl}, which was directly estimated from the vertical viscosity coefficient κ under the KPP parameterisation scheme (Large et al., 1994). One can infer that when the net heat flux is maximal during the day, κ is small, because of heating (oceQnet < 0); therefore, KPP_{hbl} is shallow, and ζ and δ increase. On the contrary, κ increases during the night because of cooling (oceQnet > 0); therefore, KPP_{hbl} is deeper, and ζ and δ decrease. Such diurnal variation modifies the frontogenetic tendency. Torres et al. (2022) reported that the frontogenesis tendency (Hoskins & Bretherton, 1972) exhibits a clear relationship with the net heat flux, with frontogenesis emphasised during the day and frontolysis emphasised during the night.

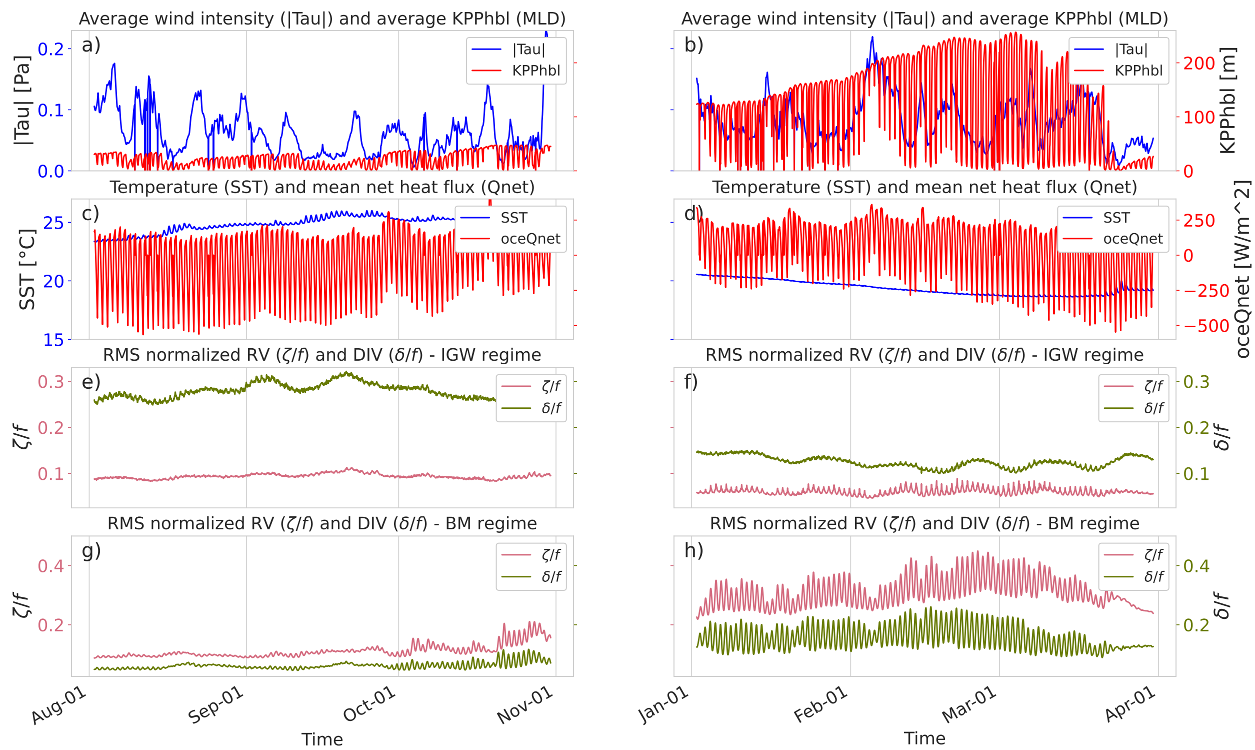

Figure 10. Time series of dynamical variables for the study area centred at 26.6 °N within the Canary current from August 2 to October 30, 2012 (a, c, e, and g) and from January 2 to March 30, 2012 (b, d, f, and h) seasons. First row (a and b): mean values for the wind stress ($|\tau|$, blue) and the KPP turbulent boundary layer depth (KPP_{hbl}, red). Second row (c and d): mean values for the sea surface temperature (T, blue) and ocean net heat flux (oceQnet, red). Third row (e and f): standard deviation of the normalized vorticity (ζ/f, magenta) and divergence (δ/f, green) fields in the internal gravity wave (IGW) regime. Fourth row (g and h): standard deviation of the normalized vorticity (ζ/f, magenta) and divergence (δ/f, green) fields in the balanced motion (BM) regime.

The time series of ζ and δ emphasises the efficiency of the dynamical filter for separating BM and IGW and its ability to recover the BM dynamics on short time scales. Furthermore, the filtering highlights the seasonal variability of the diurnal cycle and its dependence on the seasonality of KPP_{hbl}. In the next section, we focus on the diurnal cycle of the filtered fields and its latitudinal dependence.

In addition to the results shown here, specific implementation details and intermediate calculations have been already shared in our sample Jupyter notebook (Quintana, 2022).

3.5 Diurnal lag between divergence and vorticity

In addition to the seasonal differences in the diurnal cycle that were discussed in subsection 3.4, we found a time lag between the δ and ζ instantaneous intensities in the BM regime. This lag became instantly noticeable in the BM regime by closely inspecting the time series of vorticity and divergence for arbitrary 8-day periods, as per Fig. 12. This pattern was observed for all EBC time series at diurnal scales, particularly in winter. In Fig. 12, δ peaks first at around midday and ζ peaks later with a lag of $\sim$3 hours. This behaviour is consistent with previous studies based on numerical simulations with a higher horizontal resolution (Dauhajre et al., 2017; Dauhajre & McWilliams, 2018; Torres et al., 2022).

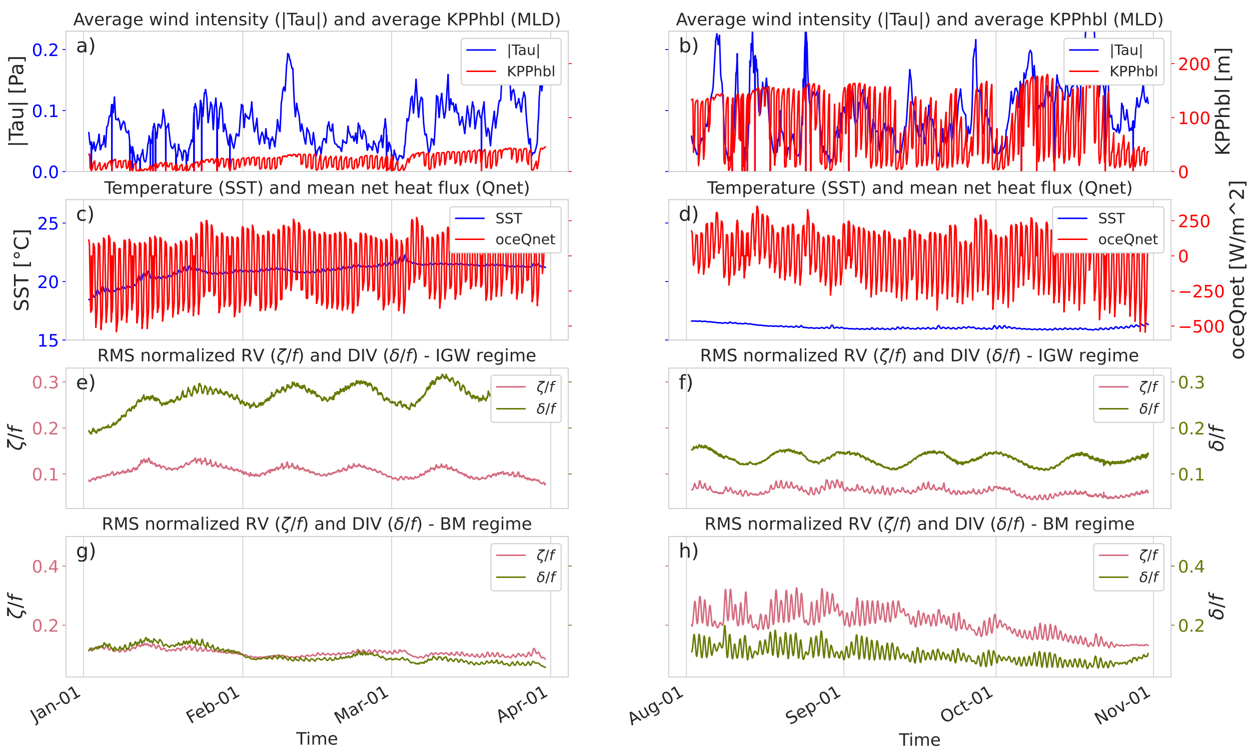

Figure 11. Time series of dynamical variables for the study area centred at 26.6 °S within the Benguela current from January 2 to March 30, 2012 (a, c, e, and g) and from August 2 to October 30, 2012 (b, d, f, and h) seasons. First row (a and b): mean values for the wind stress ($|\tau|$, blue) and the KPP turbulent boundary layer depth (KPP_{hbl}, red). Second row (c and d): mean values for the sea surface temperature (T, blue) and the ocean net heat flux (oceQnet, red). Third row (e and f): standard deviation of the normalized vorticity (ζ/f, magenta) and divergence (δ/f, green) fields in the internal gravity wave (IGW) regime. Fourth row (g and h): standard deviation of the normalized vorticity (ζ/f, magenta) and divergence (δ/f, green) fields in the balanced motion (BM) regime.

Close inspection of both time series shows a temporal phase shift between them for the diurnal frequency component. As this shift might not be evident for time series with several frequency components or for long samples, we calculated the cross power spectral density $P_{\zeta\delta}(\omega)$ (Welch, 1967), from which we obtained phase differences between both signals as a function of frequency. A positive shift implies that

δ precedes ζ, and the converse is true when the shift is negative. We then used Welch's method to obtain the spectral coherence between δ and ζ, $C_{\zeta\delta}(\omega)$ in the form

$$C_{\zeta\delta}(\omega) = \frac{|P_{\zeta\delta}(\omega)|^2}{P_{\zeta\zeta}(\omega)\, P_{\delta\delta}(\omega)}, \tag{11}$$

where $P_{AB}(\omega) = |P_{AB}(\omega)|\, e^{i\theta(\omega)}$ is the cross spectral density between variables A and B. Spectral coherence is the frequency-domain analogue of the correlation coefficient (Biltoft & Pardyjak, 2009), so values near 1 indicate a high correlation at a given frequency or, in other terms, such frequencies have major contributions to the total covariance. This methodology allowed us to confirm that diurnal divergence drives submesoscale vorticity in winter, but this result does not hold in summer.

Figure 12. Time series of dynamical variables for the study area centred at 26.6 °N within the Canary current from September 17 to September 24, 2012 (a, c, e, and g) and from February 17 to February 24, 2012 (b, d, f, and h). First row (a and b): mean values for the wind stress ($|\tau|$, blue) and the KPP turbulent boundary layer depth (KPP_{hbl}, red). Second row (c and d): mean values for the sea surface temperature (T, blue) and ocean net heat flux (oceQnet, red). Third row (e and f): standard deviations of the normalized vorticity (ζ/f, magenta) and divergence (δ/f, green) fields in the internal gravity wave (IGW) regime. Fourth row (g and h): standard deviation of the normalized vorticity (ζ/f, magenta) and divergence (δ/f, green) fields in the balanced motion (BM) regime.

To provide a more quantitative perspective, Table 1 shows the phase separation and coherence between ζ and δ calculated by season and area for the diurnal component. The first thing noted is that the coherence between δ and ζ is consistently high in winter with values above 0.95 in all cases, while phase separation shows a trend towards larger values (around 3.5 hours) as we approach high latitudes and lower values (around 2.5 h) as we get closer to the tropics. In summer, the picture is not that different, although the trend in the ζ-δ lag is not as evident as in winter, along with the fact that coherence is considerably smaller in certain study areas, particularly in northern California and southern Benguela.

Table 1. Phase difference Δt (in hours) between normalized divergence δ and vorticity ζ by current, center (latitude, longitude), and season for each quadrangular area examined. The phase difference is the angle of the complex power spectral density, calculated with a 10-day window using Welch's method (Welch, 1967). All phase differences correspond to the diurnal ($24\ h$) component. Positive values indicate that divergence occurs first and is then *followed* by the relative vorticity. Rows in bold mark the study areas compared in this thesis work. Values with an asterisk (*) correspond to cases when the coherence did not pass the F-test for the 90% confidence interval.

Current	Latitude	Longitude	Summer Δt [h]	Summer $C_{\zeta\delta}$	Winter Δt [h]	Winter $C_{\zeta\delta}$
California	48.4 °N	137 °W	2.41	0.6	3.86	0.97
California	44.5 °N	131 °W	3.14	0.88	3.81	0.97
California	40.4 °N	131 °W	3.57	0.88	3.55	0.95
California	36.05 °N	131 °W	3.22	0.93	3.21	0.97
California	31.46 °N	125 °W	2.95	0.95	3.02	0.97
California	**26.64 °N**	**125 °W**	**2.75**	**0.99**	**3.02**	**0.99**
Canary	31.46 °N	23 °W	3.61	0.95	3.83	0.99
Canary	**26.64 °N**	**23 °W**	**3.33**	**0.96**	**3.57**	**0.99**
Canary	21.61 °N	23 °W	3.35	0.98	3.33	0.99
Canary	16.40 °N	29 °W	2.75	0.97	3.13	0.99
Peru–Chile	16.39 °S	83 °W	2.16	0.67	3.09	0.99
Peru–Chile	**21.61 °S**	**77 °W**	**3.42**	**0.65**	**3.17**	**0.99**
Peru–Chile	40.41 °S	83 °W	3.15	0.94	2.66	0.97
Benguela	11.03 °S	7 °E	2.96	0.76	2.79	0.99
Benguela	16.39 °S	7 °E	2.98	0.63	3.19	0.99
Benguela	**26.64 °S**	**7 °E**	**8.5**	**0.19***	**3.13**	**0.99**

A complement to Table 1 is Fig. 13, which illustrates the trend that the ζ-δ lag follows as a function of latitude in the winter and summer seasons. These delays match what Dauhajre & McWilliams (2018) found using their transient turbulent thermal wind balance (TTTW) model, which takes into consideration the difference between the maximum (κ_{max}) and minimum (κ_{min}) RMS values of the vertical viscosity ($\Delta K = \kappa_{max} - \kappa_{min}$), the period in which this varies (T_κ), and the mixed layer depth (H), described in its 1D formulation by a system of non-dimensional equations:

$$\begin{pmatrix} u \\ v \end{pmatrix}_t + \Omega \begin{pmatrix} -v \\ u \end{pmatrix} - \Gamma \left[\mathcal{K}(t) + k \right] \begin{pmatrix} u \\ v \end{pmatrix}_{zz} = \mathcal{K}(t)(1 - \Gamma) \begin{pmatrix} \overline{u} \\ \overline{v} \end{pmatrix}, \tag{12}$$

where subscripts indicate partial derivatives, $\overline{\mathbf{u}} = (\overline{u}, \overline{v})$ is the steady solution, $\Omega = T_\kappa f_0$, $\mathcal{K}(t) = \cos(2\pi t/T_\kappa)$, $k = 2K_0/\Delta K$, and $\Omega = T_\kappa \Delta K/2H^2$, where Γ represents the ratio of the inertial frequency f_o to the diurnal period, and Γ represents the ratio of the range of mixed time scales $(\Delta K/2H^2)$ relative to the diurnal period. These 1D Ekman layer dynamics are strongly determined by atmospheric forcings as well as by their impacts on the amplitude (ΔK) and frequency (or period T_κ) of the variability of the vertical viscosity.

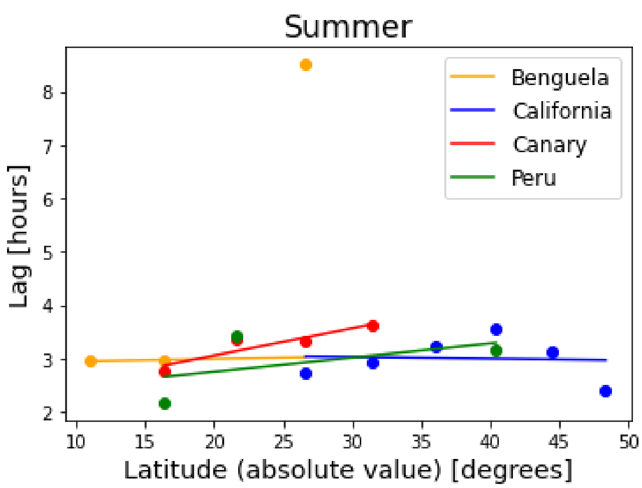

Figure 13. Lag between the divergence and vorticity fields for the four EBC in summer (left) and winter (right) as a function of the latitude (absolute value). Data points were taken from Table 1, and solid lines correspond to a first-order linear regression for each current, calculated by first excluding data points with a coherence below the 90% confidence interval (as per Table 1).

Equation 12 expresses that the amplitude and phase separation between ζ and δ are primarily controlled by inertial (Ω) and diffusive (Γ) mechanisms. If the phase separation is zero, the diffusive mechanism is the main driver (δ and ζ evolve in phase with each other). As long the phase separation is nonzero, there is competition between both mechanisms. Additionally, if the difference between κ_{min} and κ_{max} tends to zero, the amplitude of the diurnal cycle tends to zero as well. The aforementioned scenario applies when the wind stress is weak and the surface net heat flux is the main atmospheric forcing. Table 1 indicates that both mechanisms play crucial roles in dictating the diurnal cycle.

The variability of lagging between the highest and the lowest latitudes is about 1 h, indicating that the diffusive mechanism becomes slightly more relevant. In summer, the diurnal excursion of KPP_{hbl} is not as dramatic as in winter. This indicates that the difference between κ_{min} and κ_{max} is small compared to what we observed in the winter season. This explains the weak signal of the diurnal cycle in ζ and δ for the summer season.

Turbulent transient thermal wind (TTTW) is a mechanism that arises from the interaction between small-scale turbulent motions and the large-scale background flow in the ocean. It describes how the time-varying turbulent motions can drive ageostrophic secondary circulations that affect the balance of the mean flow, leading to transient adjustments of the geostrophic balance. Here, we describe the physical mechanism behind TTTW using equations.

Consider the Boussinesq equations for an incompressible, stratified fluid in the presence of the Earth's rotation, neglecting friction:

$$\frac{\partial \mathbf{u}}{\partial t} + \mathbf{u} \cdot \nabla \mathbf{u} = -\frac{1}{\rho_0} \nabla p + f\hat{\mathbf{z}} \times \mathbf{u} + \frac{1}{\rho_0} \rho \mathbf{g}, \tag{13}$$

$$\frac{\partial \rho}{\partial t} + \mathbf{u} \cdot \nabla \rho = 0, \tag{14}$$

$$\nabla \cdot \mathbf{u} = 0. \tag{15}$$

Here, $\mathbf{u}$ is the velocity vector, ρ_0 is the reference density, p is the pressure, f is the Coriolis parameter, $\hat{\mathbf{z}}$ is the unit vector in the vertical direction, ρ is the density perturbation, and $\mathbf{g}$ is the gravitational acceleration.

Now, let's decompose the velocity and density fields into mean $\overline{(\cdot)}$ and fluctuating $(\cdot)\prime$ components:

$$\mathbf{u} = \overline{\mathbf{u}} + \mathbf{u}', \tag{16}$$

$$\rho = \overline{\rho} + \rho'. \tag{17}$$

Substituting these decompositions into the Boussinesq equations and taking the time average, we obtain the equations for the mean flow:

$$\frac{\partial \overline{\mathbf{u}}}{\partial t} + \overline{\mathbf{u}} \cdot \nabla \overline{\mathbf{u}} = -\frac{1}{\rho_0} \nabla \overline{p} + f\hat{\mathbf{z}} \times \overline{\mathbf{u}} + \frac{1}{\rho_0} \overline{\rho} \mathbf{g} - \nabla \cdot \overline{\mathbf{u}'\mathbf{u}'}, \tag{18}$$

$$\frac{\partial \overline{\rho}}{\partial t} + \overline{\mathbf{u}} \cdot \nabla \overline{\rho} = -\nabla \cdot \overline{\mathbf{u}'\rho'}. \tag{19}$$

In the quasi-steady state, the thermal wind balance for the mean flow is given by:

$$f\hat{\mathbf{z}} \times \overline{\mathbf{u}} = -\frac{1}{\rho_0}\nabla \overline{p} + \frac{1}{\rho_0}\overline{\rho}\mathbf{g}. \tag{20}$$

Now, let's consider the equations for the fluctuating components by subtracting the mean equations from the original Boussinesq equations:

$$\frac{\partial \mathbf{u}'}{\partial t} + \overline{\mathbf{u}} \cdot \nabla \mathbf{u}' + \mathbf{u}' \cdot \nabla \overline{\mathbf{u}} + \mathbf{u}' \cdot \nabla \mathbf{u}' = -\frac{1}{\rho_0}\nabla p' + f\hat{\mathbf{z}} \times \mathbf{u}' + \frac{1}{\rho_0}\rho'\mathbf{g}, \tag{21}$$

$$\frac{\partial \rho'}{\partial t} + \overline{\mathbf{u}} \cdot \nabla \rho' + \mathbf{u}' \cdot \nabla \overline{\rho} + \mathbf{u}' \cdot \nabla \rho' = 0. \tag{22}$$

The TTTW mechanism is associated with the interaction between the fluctuating components of velocity and density with the mean flow. The key term in this interaction is the Reynolds stress divergence, $\nabla \cdot \overline{\mathbf{u}'\mathbf{u}'}$, which appears in the momentum equation for the mean flow. This term represents the horizontal momentum transport by the turbulent fluctuations.

The TTTW mechanism can be understood as follows:

1. Turbulent motions generate horizontal velocity fluctuations that are correlated with density fluctuations (i.e., $\overline{\mathbf{u}'\rho'} \neq 0$).

2. The correlated velocity and density fluctuations drive a secondary ageostrophic circulation, which modifies the mean flow and leads to a transient adjustment of the thermal wind balance.

3. This transient adjustment causes the mean flow to evolve, redistributing kinetic energy between the mean and fluctuating components.

In summary, the TTTW mechanism arises from the interaction of turbulent fluctuations with the background flow, leading to the generation of ageostrophic secondary circulations and a transient adjustment of the thermal wind balance. The key term in this process is the Reynolds stress divergence, which represents the horizontal momentum transport by the turbulent fluctuations.

3.6 Discussion

The dynamical filter presented in this study relies on the dispersion relation of IGW of the local tenth baroclinic normal mode, limited by the dominant tides below it. Qiu et al. (2018) and Torres et al. (2018) applied a similar technique in the spectral space. However, they did not recover BM in the physical space. Here, we tested the performance of this dynamical filter by recovering BM and IGW in the physical space in four EBC, where IGW showed a kinetic energy level close to the submesoscale BM (Savage et al., 2017; Qiu et al., 2018; Torres et al., 2018). Preliminary analyses (not shown) demonstrated that the correct way to use the dispersion relation of the tenth baroclinic is to combine it with the permissible tide as a cut-off wavenumber-dependent frequency (Qiu et al., 2018).

BM explain most of the advective horizontal and vertical transport of heat and any tracers in the ocean (Ferrari & Wunsch, 2009; Klein et al., 2019). However, diagnosing such transport in the presence of IGW requires, first, the partitioning of both classes of motion. Using low-pass temporal filters to remove IGW contributions also removes the high-frequency part of frontal dynamics (Qiu et al., 2017, 2018). A spatial filter that removes large horizontal scales results in incomplete removal of IGW (see supporting information in Torres et al. (2022)). The challenge is that IGW and submesoscale BM share the same short time scale and small horizontal scale ranges. The application of dynamical filters is an alternative to accurately partition BM and IGW. In this research, we aimed to make improvements in two areas: a) isolating IGW from BM regimes and b) studying them separately within the four major EBC.

Recently, Torres et al. (2022) developed a simple approach to separate small-scale frontal dynamics from energetic internal gravity waves. Their method relies on two assumptions: IGW are mostly captured by low baroclinic normal modes and, therefore, by vertical scales larger than the mixed-layer depth. Second, small-scale frontal dynamics are trapped within the mixed-layer depth and, therefore, are explained by smaller vertical scales. The disadvantage of the method described by Torres et al. (2022) is that BM and IGW cannot be separated below the mixed-layer depth. The method proposed here circumvents this constraint by relying on the local dispersion relation of IGW. The workflow used to apply our method to the ocean numerical simulation was as follows: 1) compute the frequency–wavenumber spectrum of KE; 2) compute the n-*th* local baroclinic normal modes as long as the spacing interval allows it; 3) identify the dispersion relation of the n-*th* baroclinic mode that best separates IGW and B; 4) use this dispersion relation as a criterion to separate BM and IGW in the Fourier space (3D spectral space (k,l,ω)), and 5) compute the inverse Fourier transform to get back to the physical space (x,y,t). This workflow can be applied at any vertical level in the water column and to any component of the speed vector and tracer. Calculations over the filtered variables can be performed, always considering there will be some noise as the complexity of such calculations grows, since handling slightly unevenly spaced, discrete, windowed data leads to some sort of spectral leakage.

The BM and IGW separation during winter poses a challenge due to the small-scale motions with frequencies larger than M_2 internal tides. In this chapter, we used the model output of the LLC4320 simulation with a nominal horizontal resolution of $\sim$ 2 km ($1/48°$). Our method mitigates the leakage of information from BM to IGW during winter. Nevertheless, the horizontal and vertical resolutions of the LLC4320 prevent the proliferation of small-scale motions with frequencies larger than M_2 internal tides. Nelson et al. (2019) demonstrated the strengthen of the kinetic energy frequency spectrum at frequencies greater than M_2 internal tides when the horizontal and vertical resolutions increases. However, this scenario needs to be tested by analysing the JPDF of ζ and δ, as we did in this study.

Recovering high-frequency ($\omega > f$) submesoscale motions in the presence of IGW is a critical issue for diagnosing vertical heat transport in the ocean. Su et al. (2020) and Siegelman et al. (2020) reported the impact of high-frequency motions on vertical heat fluxes using LLC4320, and Richards et al. (2021) reported the impact using ROMS simulations, further confirming the contribution of such high-frequency motions as a doubling of the amplitude of the vertical heat flux when compared with low-frequency estimates ($<$ 1/36-hr). The performance of our dynamical filter when recovering BM at short time scales was tested in four EBC and in two seasons. The JPDF of ζ-δ in the BM regime revealed ζ/f values close to or larger than one during winter, which reflects the presence of ageostrophic motions (McWilliams, 2019). The time series of the same variables displays diurnal variability, which is a distinctive characteristic of submesoscale motions (Dauhajre & McWilliams, 2018; Sun et al., 2020; Torres et al., 2022). Previous studies have described the dependency of the diurnal cycle on the vertical eddy viscosity κ (Wenegrat & McPhaden, 2016). Here, we reveal, for the first time, the seasonal variability of the diurnal cycle of ζ and δ, which is mainly modulated by KPP diagnostics. The model output of LLC4320 does not provide κ, but one can use KPP_{hbl} as a proxy for the seasonal and diurnal variability of the strength of κ.

As we have already stated, the methodology proposed in this thesis work is not flawless; even if this were the case, its implementation is not feasible in all cases. First, although the design of the filter does not depend on the measurement data or simulation outputs within the region of interest, if tides near the inertial frequency are highly energetic on the submesoscale BM regime, both regimes will overlap, and consequently it will be hard to chose a maximum cutoff frequency of the filter (see black dashed line in Fig. 3); in this scenario, the resulting BM regime could either include BM motions and internal tides, or miss some submesoscale BM features. Also, the filter requires access to data whose spatial and temporal resolution (i.e. sampling period) is enough to resolve submesoscales and internal gravity waves of at least the maximum cutoff frequency (e.g., M_2 tides), while having the minimum (Nyquist) sampling frequency to diminish aliasing effects as much as possible, otherwise the analysis will be highly contaminated and lead to invalid results.

Additional concerns may exist regarding the interaction between IGW and BM motions, such as inertial (or near-inertial) waves that are trapped by eddies. These interactions, however, would not have any impact on the filter. Conversely, analyses in the physical or spectral space of BM-IGW interactions could benefit from the separation of regimes our method has achieved.

Chapter 4. Kinetic energy exchange between BM and IGW

4.1 Mathematical framework

For any variable of interest ψ (e.g. velocity, force, energy, etc), we can write the partition into its BM and IGW components as

$$\psi = \psi_B + \psi_W, \tag{23}$$

where ψ_B and ψ_W are the BM and IGW components of ψ, respectively, $\{\ \}_B$ is the filter operator that isolates the BM component of the field so that

$$\psi_B = \{\psi\}_B\,, \tag{24}$$

and its complement, $\{\ \}_W$, that isolates the IGW component

$$\psi_W = \psi - \{\psi\}_B = \psi - \psi_B. \tag{25}$$

At this point, the partitioning of the motion into its BM and IGW components through of the application of the dynamical filtering function (see Eq. 5) has proved to be successful. As it turns out, we are able to analyse the kinetic energy exchange between these regimes.

In this section we will borrow some of the basic postulates and assumptions from the turbulence theory in its statistical formulation, where the fields and equations of motion are *averaged* using a generalised averaging function. After we compare the properties of such averaging function to the ones of the filtering function and applying them to the fields and motion equations in a similar manner, a *filtering* formulation will arise (similarly to Barkan et al. (2017) and, in a more general way, to Germano (1992) and Johnson (2020)), so we can obtain an expression for the KE exchange between the BM and IGW components of the flow. Such formulation will impose certain conditions on the filter, which will need to be proved valid for the dynamical filter we use in this work. At the end of the day, the analogies between the *statistical* and the *filtering* formulations will be helpful in the interpretation of the results we obtain for the latter, such as its implications in models that cannot resolve IGW.

4.1.1 Reynolds conditions in the filtering approach

Any filter operator in Eq. 24 can be also written as the convolution of the signal ψ and the kernel $K\left(x,y,z,t\right)$.

$$\begin{aligned} \psi = \{\psi\}_B = \psi \star K = & \int_{\Omega'} \psi\left(x-x', y-y', z-z', t-t'\right) K\left(x', y', z', t'\right)\, d\Omega' \\ = & \int_{\Omega'} \psi\left(x', y', z', t'\right) K\left(x-x', y-y', z-z', t-t'\right)\, d\Omega', \end{aligned} \tag{26}$$

where Ω is the entire domain. Then, when we calculate the Fourier transform $F[\ ]$ of the equation Eq. 26 for $\{\psi\}_B$ we get that

$$F\left[\{\psi\}_B\right] = F\left[\psi \star K\right] = F[\psi]F[K]. \tag{27}$$

If the convolutional kernel $K\left(x,y,z,t\right)$ is the dynamical filter in the physical space (i.e. the inverse Fourier transform of Eq. 8), it follows that $F[K]\left(k_x, k_y, k_z, \omega\right)$ is the Fourier transform of the dynamical filter, so that $F[\psi]F[K]$ represents the application of the filter K over f in the Fourier space. It is worth mentioning that, in the Fourier space, $F[K]\left(k_x, k_y, k_z, \omega\right)$ is given by Eq. 8, whose value is approximately 1 for the region in the Fourier spectrum below the plane described by Eq. 6, and 0 otherwise (see white area in Fig. 5, right panel).

On the one hand, from the properties of the convolution operator, the dynamical filtering satisfies the following conditions for any two given variables ψ, ξ, and a constant a:

$$\{\psi + \xi\}_B = \psi_B + \xi_B, \tag{28a}$$

$$\{a\psi\}_B = a f_B, \tag{28b}$$

$$\{a\}_B = a, \tag{28c}$$

$$\left\{\frac{\partial \psi}{\partial s}\right\}_B = \frac{\partial \psi_B}{\partial s}, \qquad \text{where } s = \{x,y,z,t\}. \tag{28d}$$

On the other hand, conditions in Eqs. 28 are also satisfied by any averaging rule (Monin & Yaglom,

1979) defined as

$$
\begin{aligned}
\overline{f(x,y,z,t)} &= \int_{\Omega'} f\left(x-x',y-y',z-z',t-t'\right)\gamma\left(x',y',z',t'\right)\, d\Omega' \\
&= \int_{\Omega'} f\left(x',y',z',t'\right)\gamma\left(x-x',y-y',z-z',t-t'\right)\, d\Omega',
\end{aligned}
\tag{29}
$$

where $\gamma(x,y,z,t)$ is an arbitrary weighting function, or a probability density function (pdf). An example of a pdf is the uniform distribution of width T centred at $t=0$:

$$
\gamma(x,y,z,t) = \frac{1}{T}\delta(x)\delta(y)\delta(z)\left(H(t+T/2)-H(t-T/2)\right), \tag{30}
$$

where $H(t)$ is the Heaviside function and $\delta(x_i)$ is the Dirac delta function. When applied as an weighting function as in Eq. 29, it results in a moving average in time, widely used to smooth out time series or, in other words, to filter out the fluctuations whose period is shorter than T.

Such averaging rules are the base of the statistical description of turbulence (Monin & Yaglom, 1979; McComb, 1990), which separates the motion into its mean ($\overline{f}$) and fluctuating ($f' = f - \overline{f}$) components. In this context, the choice of a pdf is constrained by a set of conditions known as the *Reynolds conditions* that must be satisfied for two arbitrary functions f, g, and a constant a:

$$
\overline{f+g} = \overline{f} + \overline{g}, \tag{31a}
$$

$$
\overline{af} = a\overline{f}, \tag{31b}
$$

$$
\overline{a} = a, \tag{31c}
$$

$$
\overline{\frac{\partial f}{\partial s}} = \frac{\partial \overline{f}}{\partial s}, \qquad \text{where } s = \{x,y,z,t\}, \tag{31d}
$$

$$
\overline{\overline{f}g} = \overline{f}\,\overline{g}, \tag{31e}
$$

The last condition, strictly speaking, will not be satisfied exactly for any, even simple, weighting function $\gamma(x,y,z,t)$. In spite of this, we can relax this condition and the only requirement is that it be must satisfied approximately (Monin & Yaglom, 1979), which might be verified numerically in case it poses a concern.

If the Reynolds conditions (Eqs. 31) are satisfied, the following properties become valid

$$\overline{\overline{f}} = \overline{f}, \tag{32a}$$

$$\overline{f'} = \overline{f - \overline{f}} = \overline{f} - \overline{f} = 0, \tag{32b}$$

$$\overline{\overline{f}g'} = \overline{f}\left(\overline{g'}\right) = 0, \tag{32c}$$

$$\overline{fg} = \overline{\left(\overline{f} + f'\right)\left(\overline{g} + g'\right)} = \left(\overline{f}\right)\left(\overline{g}\right) + \overline{f'g'} \neq \overline{f}\overline{g}, \tag{32d}$$

$$\overline{f'g'} \neq 0, \tag{32e}$$

$$\overline{\frac{\partial f'}{\partial s}} = \frac{\partial \overline{f'}}{\partial s}, \qquad \text{where } s = \{x, y, z, t\}. \tag{32f}$$

By comparing the properties of the filtering operator (Eqs. 28) and the Reynolds conditions (as per Eqs. 31), one can see the former is a subset of the latter, since the last condition (Eq. 31e) does not have an equivalent in the filter properties. However, as we do for the statistical formulation, where we cannot ensure the last Reynolds condition (Eq. 31e) holds true for any pdf, we can require the condition

$$\{\{\psi\}_B\,\xi\}_B = \psi_B \xi_B, \tag{33}$$

to be satisfied to an extent, so we can include it in Eqs. 28 to establish a complete analogy between the filtering and averaging operators. It makes sense that we can "borrow" the turbulence theory and apply it to the BM-IGW partition by means of the dynamical filter we designed and implemented, so that

$$\{\psi_B\}_B = \psi_B, \tag{34a}$$

$$\{\psi_W\}_B = \{\psi - \psi_B\}_B = \psi_B - \psi_B = 0, \tag{34b}$$

$$\{\psi_B \xi_W\}_B = \psi_B \{\xi_W\}_B = 0, \tag{34c}$$

$$\{\psi\xi\}_B = \{(\{\psi\}_B + \psi_W)(\{\xi\}_B + \xi_W)\}_B = \{\psi_B\xi_B\}_B + \{\psi_W\xi_W\}_B \neq \{\psi\}_B\{\xi\}_B\,, \tag{34d}$$

$$\{\psi_W\xi_W\}_B \neq 0, \tag{34e}$$

$$\left\{\frac{\partial \psi}{\partial s}\right\}_W = \frac{\partial \psi_W}{\partial s} \tag{34f}$$

are completely analogous to the properties in Eq. 32, with s being one of the coordinates $\{x, y, z, t\}$.

In analogy to the statistical formulation, we refer to the set of Eqs. 28 along with Eq. 33 as the **Reynolds conditions for filtered fields**. We leave the proof of its validity, in particular the last one (Eq. 33), to Appendix A.

4.1.2 Equations of motion for the BM and IGW regimes

Given the Reynolds conditions for the filtering operator hold valid, we can now derive the equations that describe the kinetic energy exchange between BM and IGW.

Here, it is worth spending a few lines to explain what we are doing next and what it might imply. Assume we need to run a numerical model that is only capable of resolving BM, so that we can only compute the BM component of the fields and its kinetic energy, but we are also interested in including the impact that IGW might have on the kinetic energy of the BM regime, similarly to the way models parameterise smaller-scale effects such as turbulence. In this scenario, we focus on the equations that describe KE from the BM realm only; one can achieve this by applying the filter $\{\ \}_B$ to the fundamental equations, whose result will be a **projection of the physics onto the BM domain** which, given the non-linearity of the motion equations, will contain terms that depend on the contribution by IGW.

We start by expressing continuity equation for an incompressible fluid in terms of the BM and IGW components

$$\frac{\partial u_i}{\partial x_i} = \frac{\partial \left(\{u_i\}_B + \{u_i\}_W \right)}{\partial x_i} = \frac{\partial \{u_i\}_B}{\partial x_i} + \frac{\partial \{u_i\}_W}{\partial x_i} = 0, \tag{35}$$

along with the momentum equations (Eq.4), now expressed as

$$\begin{aligned} &\frac{\partial \left(\{u_i\}_B + \{u_i\}_W \right)}{\partial t} + \left(\{u_i\}_B + \{u_i\}_W \right) \frac{\partial \left(\{u_i\}_B + \{u_i\}_W \right)}{\partial x_j} + \epsilon_{i3k} f \hat{e}_3 \left(\{u_k\}_B + \{u_k\}_W \right) \\ &= \frac{\partial \{u_i\}_B}{\partial t} + \{u_i\}_B \frac{\partial \{u_i\}_B}{\partial x_j} + \epsilon_{i3k} f \hat{e}_3 \{u_k\}_B + \frac{\partial \{u_i\}_W}{\partial t} + \{u_i\}_W \frac{\partial \{u_i\}_W}{\partial x_j} + \epsilon_{i3k} f \hat{e}_3 \{u_k\}_W \\ &+ \{u_i\}_B \frac{\partial \{u_i\}_W}{\partial x_j} + \{u_i\}_W \frac{\partial \{u_i\}_B}{\partial x_j} = \{X_i\}_B + \{X_i\}_W - \frac{\partial \left(\phi_B + \phi_W \right)}{\partial x_i} + \nu \frac{\partial^2 \left(\{u_i\}_B + \{u_i\}_W \right)}{\partial^2 x_j}, \end{aligned} \tag{36}$$

and then applying then filter kernel $K(x, y, z, t)$ (Eq. 8), that satisfies Eqs. 28 and 33.

For the continuity equation we obtain

$$\left\{\frac{\partial u_i}{\partial x_i}\right\}_B = \frac{\partial \{u_i\}_B}{\partial x_i} = 0, \tag{37}$$

that, in combination to the continuity equation for the entire flow (Eq. 35), in turn implies

$$\frac{\partial \{u_i\}_W}{\partial x_i} = 0, \tag{38}$$

so that the BM and IGW components comply with the continuity equations by themselves. On the other hand, the BM component of the equations of motion 36, since they are non-linear in $\{u_i\}_B$, become

$$\frac{\partial \{u_i\}_B}{\partial t} + \{u_j\}_B \frac{\partial \{u_i\}_B}{\partial x_j} + \left\{\{u_j\}_W \frac{\partial \{u_i\}_W}{\partial x_j}\right\}_B + \epsilon_{i3k} f \hat{e}_3 \{u_k\}_B = \{X_i\}_B - \frac{\partial \phi_B}{\partial x_i} + \nu \frac{\partial^2 \{u_i\}_B}{\partial^2 x_j}, \tag{39}$$

where the terms on the right hand side are the BM components of the external forces, pressure gradient, and viscous dissipation, respectively, whereas the first two terms in the left hand side are analogous to $\frac{D\{u_i\}_B}{Dt}$, considering advection by the BM components $\{u_j\}_B$ only. The third term in the left hand side, by means of the continuity equation (Eq. 37) can be written as

$$\left\{\{u_j\}_W \frac{\partial \{u_i\}_W}{\partial x_j}\right\}_B = \frac{\partial}{\partial x_j} \left\{\{u_i\}_W \{u_j\}_W\right\}_B = \frac{\partial \tau_{ij}}{\partial x_j}, \tag{40}$$

where we just defined the second-rank tensor

$$\tau_{ij} = \left\{\{u_i\}_W \{u_j\}_W\right\}_B, \tag{41}$$

which, in analogy with the turbulence theory, represents the additional **stress that IGW exerts on BM** (Germano, 1992; Barkan et al., 2017; Johnson, 2020).

This way, by arranging Eq. 39 we arrive at the equations of motion for the BM regime

$$\frac{\partial \left\{u_i\right\}_B}{\partial t} + \left\{u_j\right\}_B \frac{\partial \left\{u_i\right\}_B}{\partial x_j} + \epsilon_{i3k} f \hat{e}_3 \left\{u_k\right\}_B = \left\{X_i\right\}_B - \frac{\partial \phi_B}{\partial x_i} + \nu \frac{\partial^2 \left\{u_i\right\}_B}{\partial^2 x_j} - \frac{\partial \tau_{ij}}{\partial x_j}, \tag{42}$$

which, when substracted from the momentum equations (Eqs. 36), result in a similar set of equations for the IGW realm

$$\begin{aligned} \frac{\partial \left\{u_i\right\}_W}{\partial t} + \left\{u_j\right\}_W \frac{\partial \left\{u_i\right\}_W}{\partial x_j} + \left\{u_j\right\}_B \frac{\partial \left\{u_i\right\}_W}{\partial x_j} + \left\{u_j\right\}_W \frac{\partial \left\{u_i\right\}_B}{\partial x_j} + \epsilon_{i3k} f \hat{e}_3 \left\{u_k\right\}_W \\ = \left\{X_i\right\}_W - \frac{\partial \phi_W}{\partial x_i} + \nu \frac{\partial^2 \left\{u_i\right\}_W}{\partial^2 x_j} + \frac{\partial \tau_{ij}}{\partial x_j}. \end{aligned} \tag{43}$$

By simple inspection, we note that both equations contain the same derivatives of the stress tensor τ_{ij}, which is entirely a function of the IGW fields, but with opposite sings. This is the first hint that τ_{ij} is involved in the KE exchange between BM (Eqs. 37 and 42) and IGW (Eqs. 38 and 43). This stress term has a similar effect than the dissipation by kinematic or turbulent viscosity, with the difference that is can be positive or negative.

In contrast with the turbulence theory, where τ_{ij} can be understood as the auto-covariance tensor of the field u', in the filtering approach each entry in τ_{ij} corresponds to the wave-wave interaction between $\left\{u_i\right\}_W$ and $\left\{u_j\right\}_W$ captured by the filter $\{\ \}_B$. For instance, if we have two different waves $\Psi_1\left(k_1, \omega_1\right)$ and $\Psi_2\left(k_2, \omega_2\right)$, their nonlinear interaction will result in 4 new waves

$$\begin{aligned} \Psi_1\left(k_1, \omega_1\right) \Psi_2\left(k_2, \omega_2\right) = \Psi_a\left(k_1 + k_2, \omega_1 + \omega_2\right) + \Psi_b\left(k_1 + k_2, \omega_1 - \omega_2\right) \\ + \Psi_c\left(k_1 - k_2, \omega_1 + \omega_2\right) + \Psi_d\left(k_1 - k_2, \omega_1 - \omega_2\right), \end{aligned} \tag{44}$$

so that the application of the filter onto it (i.e. $\left\{\Psi_1\left(k_1, \omega_1\right) \Psi_2\left(k_2, \omega_2\right)\right\}_B$) τ_{ij} will only capture the wave-wave stress in the BM domain (i.e. the ones whose frequency and wavenumber are below the IGW$_{10}$ dispersion line given by Eq. 6, see the white area in Fig 5, right panel); in this example, it is possible that the filter only captures the slower, longer wave Ψ_d into the stress tensor τ_{ij}. We will further investigate the effect of τ_{ij} on the KE exchange in the following sections.

4.1.3 Kinetic energy exchange between BM and IGW regimes

Now that we have the equations of motion for the BM and IGW regimes, we can proceed to derive an expression of the evolution of kinetic energy in the BM realm. First, if we put the density aside of the equations, the total kinetic energy (KE) is given by

$$\begin{aligned} KE = \frac{1}{2}u_i u_i &= \frac{1}{2}\left(\{u_i\}_B + \{u_i\}_W\right)\left(\{u_i\}_B + \{u_i\}_W\right) \\ &= \frac{1}{2}\left(\{u_i\}_B \{u_i\}_B + 2\{u_i\}_B \{u_i\}_W + \{u_i\}_W \{u_i\}_W\right). \end{aligned} \tag{45}$$

Following a similar procedure as we just did to project (i.e. filter) the motion equations into the BM regime, we filter the total KE (Eq. 45) with $\{\ \}_B$ to obtain

$$\begin{aligned} \{KE\}_B = \frac{1}{2}\{u_i u_i\}_B &= \frac{1}{2}\left(\{u_i\}_B \{u_i\}_B + 2\{\{u_i\}_B \{u_i\}_W\}_B + \{\{u_i\}_W \{u_i\}_W\}_B\right) \\ &= \frac{1}{2}\{u_i\}_B \{u_i\}_B + \frac{1}{2}\{\{u_i\}_W \{u_i\}_W\}_B \\ &= \frac{1}{2}\{u_i\}_B \{u_i\}_B + \frac{1}{2}\sum_i \tau_{ii} = \kappa_B + \kappa_W, \end{aligned} \tag{46}$$

where κ_B and κ_W in the right hand side are the BM and IGW **contributions** to the BM kinetic energy (KE_B), respectively. It is important to emphasise that Eq. 46 implies that the total KE in the BM regime is not explained by the BM KE (κ_B) alone, but it also contains IGW **contributions** whose origin are the nonlinear wave-wave interactions that occur in the IGW regime (see Eqs. 41 and 44).

Then, to derive the equation for the evolution of the total KE we multiply the full momentum equation (Eq. 36) by u_i, which results in

$$
\begin{aligned}
u_i\frac{\partial u_i}{\partial t} + u_i u_j\frac{\partial u_i}{\partial x_j} + u_i\epsilon_{i3k}f\hat{e}_3 u_k &= \frac{1}{2}\frac{\partial\left(u_i u_i\right)}{\partial t} + \frac{1}{2}u_j\frac{\partial\left(u_i u_i\right)}{\partial x_j}\\
&= \frac{1}{2}\frac{\partial\left(\left(\{u_i\}_B + \{u_i\}_W\right)\left(\{u_i\}_B + \{u_i\}_W\right)\right)}{\partial t}\\
&+\frac{1}{2}\left(\{u_i\}_B + \{u_i\}_W\right)\frac{\partial\left(\left(\{u_i\}_B + \{u_i\}_W\right)\left(\{u_i\}_B + \{u_i\}_W\right)\right)}{\partial x_j}\\
&= \frac{1}{2}\frac{\partial\left(\{u_i\}_B\{u_i\}_B\right)}{\partial t} + \frac{1}{2}\frac{\partial\left(\{u_i\}_W\{u_i\}_W\right)}{\partial t} + \frac{\partial\left(\{u_i\}_B\{u_i\}_W\right)}{\partial t}\\
&+\frac{1}{2}\{u_i\}_B\frac{\partial\left(\{u_i\}_B\{u_i\}_B\right)}{\partial x_j} + \frac{1}{2}\{u_i\}_B\frac{\partial\left(\{u_i\}_W\{u_i\}_W\right)}{\partial x_j}\\
&+\frac{1}{2}\{u_i\}_W\frac{\partial\left(\{u_i\}_B\{u_i\}_B\right)}{\partial x_j} + \frac{1}{2}\{u_i\}_W\frac{\partial\left(\{u_i\}_W\{u_i\}_W\right)}{\partial x_j}\\
&+\{u_i\}_B\frac{\partial\left(\{u_i\}_B\{u_i\}_W\right)}{\partial x_j} + \{u_i\}_I\frac{\partial\left(\{u_i\}_B\{u_i\}_W\right)}{\partial x_j}\\
= u_i X_i - u_i\frac{\partial\phi}{\partial x_i} + u_i\nu\frac{\partial^2 u_i}{\partial^2 x_j} &= \{u_i\}_B\{X_i\}_B + \{u_i\}_B\{X_i\}_W + \{u_i\}_W\{X_i\}_B + \{u_i\}_W\{X_i\}_W\\
&-\{u_i\}_B\frac{\partial\phi_B}{\partial x_i} + -\{u_i\}_B\frac{\partial\phi_W}{\partial x_i} + -\{u_i\}_W\frac{\partial\phi_B}{\partial x_i} + -\{u_i\}_W\frac{\partial\phi_W}{\partial x_i} +\\
&+\{u_i\}_B\nu\frac{\partial^2\{u_i\}_B}{\partial^2 x_j} + \{u_i\}_B\nu\frac{\partial^2\{u_i\}_W}{\partial^2 x_j} + \{u_i\}_W\nu\frac{\partial^2\{u_i\}_B}{\partial^2 x_j} + \{u_i\}_W\nu\frac{\partial^2\{u_i\}_W}{\partial^2 x_j},
\end{aligned}
\tag{47}
$$

and then apply the filtering operator $\{\ \}_B$ on it to yield

$$
\begin{aligned}
&\frac{1}{2}\frac{\partial\left(\{u_i\}_B\{u_i\}_B\right)}{\partial t} + \frac{1}{2}\frac{\partial\left\{\{u_i\}_W\{u_i\}_W\right\}_B}{\partial t}\\
&+\frac{1}{2}\{u_j\}_B\frac{\partial\left(\{u_i\}_B\{u_i\}_B\right)}{\partial x_j} + \frac{1}{2}\{u_j\}_B\frac{\partial\left\{\{u_i\}_W\{u_i\}_W\right\}_B}{\partial x_j}\\
&+\frac{1}{2}\left\{\{u_j\}_W\frac{\partial\left(\{u_i\}_W\{u_i\}_W\right)}{\partial x_j}\right\}_B + \left\{\{u_j\}_W\frac{\partial\left(\{u_i\}_B\{u_i\}_W\right)}{\partial x_j}\right\}_B\\
&= \{u_i\}_B\{X_i\}_B + \left\{\{u_i\}_W\{X_i\}_W\right\}_B - \{u_i\}_B\frac{\partial\phi_B}{\partial x_i} - \left\{\{u_i\}_W\frac{\partial\phi_W}{\partial x_i}\right\}_B\\
&+\nu\{u_i\}_B\frac{\partial^2\{u_i\}_B}{\partial^2 x_j} + \nu\left\{\{u_i\}_W\frac{\partial^2\{u_i\}_W}{\partial^2 x_j}\right\}_B.
\end{aligned}
\tag{48}
$$

Also, the evolution of the first term in the right hand side of Eq. 46 can be obtained by multiplying Eq. 42 by $\{u_i\}_B$

$$
\begin{aligned}
\{u_i\}_B \frac{\partial \{u_i\}_B}{\partial t} + \{u_i\}_B \{u_j\}_B \frac{\partial \{u_i\}_B}{\partial x_j} + \{u_i\}_B \epsilon_{i3k} f \hat{e}_3 \{u_k\}_B \\
= \frac{1}{2}\frac{\partial \left(\{u_i\}_B \{u_i\}_B\right)}{\partial t} + \frac{1}{2}\{u_j\}_B \frac{\partial \left(\{u_i\}_B \{u_i\}_B\right)}{\partial x_j} \\
= \{u_i\}_B \{X_i\}_B - \{u_i\}_B \frac{\partial \phi_B}{\partial x_i} + \{u_i\}_B \nu \frac{\partial^2 \{u_i\}_B}{\partial^2 x_j} - \{u_i\}_B \frac{\partial \tau_{ij}}{\partial x_j}.
\end{aligned}
\tag{49}
$$

Before substracting Eq. 49 from Eq. 48, it is worth rewriting the last term in the right hand side of the former as

$$
\begin{aligned}
\{u_i\}_B \frac{\partial \tau_{ij}}{\partial x_j} = \frac{\partial \left(\{u_i\}_B \tau_{ij}\right)}{\partial x_j} - \tau_{ij}\frac{\partial \{u_i\}_B}{\partial x_j} = \left\{\frac{\partial \left(\{u_i\}_B \{u_i\}_W \{u_j\}_W\right)}{\partial x_j}\right\}_B - \tau_{ij}\frac{\partial \{u_i\}_B}{\partial x_j} \\
= \left\{\{u_j\}_W \frac{\partial \left(\{u_i\}_B \{u_i\}_W\right)}{\partial x_j}\right\}_B + \left\{\{u_i\}_B \{u_i\}_W \frac{\partial \{u_j\}_W}{\partial x_j}\right\}_B - \tau_{ij}\frac{\partial \{u_i\}_B}{\partial x_j} \\
= \left\{\{u_j\}_W \frac{\partial \left(\{u_i\}_B \{u_i\}_W\right)}{\partial x_j}\right\}_B - \tau_{ij}\frac{\partial \{u_i\}_B}{\partial x_j},
\end{aligned}
\tag{50}
$$

where we made use of the continuity equation (Eq. 38) along with the Reynolds conditions for filtered fields (see Eqs. 28 and 33), so that we can now rewrite Eq. 49 as

$$
\begin{aligned}
\frac{1}{2}\frac{\partial \left(\{u_i\}_B \{u_i\}_B\right)}{\partial t} + \frac{1}{2}\{u_j\}_B \frac{\partial \left(\{u_i\}_B \{u_i\}_B\right)}{\partial x_j} + \left\{\{u_j\}_W \frac{\partial \left(\{u_i\}_B \{u_i\}_W\right)}{\partial x_j}\right\}_B \\
= \{u_i\}_B \{X_i\}_B - \{u_i\}_B \frac{\partial \phi_B}{\partial x_i} + \nu \{u_i\}_B \frac{\partial^2 \{u_i\}_B}{\partial^2 x_j} + \tau_{ij}\frac{\partial \{u_i\}_B}{\partial x_j}.
\end{aligned}
\tag{51}
$$

Now, we obtain the expression for the IGW contribution to Eq. 48 by subtracting the BM contribution (Eq. 51) from it

$$
\begin{aligned}
\frac{1}{2}\frac{\partial \left\{\{u_i\}_W \{u_i\}_W\right\}_B}{\partial t} + \frac{1}{2}\{u_j\}_B \frac{\partial \left\{\{u_i\}_W \{u_i\}_W\right\}_B}{\partial x_j} + \frac{1}{2}\left\{\{u_j\}_W \frac{\partial \left(\{u_i\}_W \{u_i\}_W\right)}{\partial x_j}\right\}_B \\
= \left\{\{u_i\}_W \{X_i\}_W\right\}_B - \left\{\{u_i\}_W \frac{\partial \phi_W}{\partial x_i}\right\}_B + \nu \left\{\{u_i\}_W \frac{\partial^2 \{u_i\}_W}{\partial^2 x_j}\right\}_B - \tau_{ij}\frac{\partial \{u_i\}_B}{\partial x_j}.
\end{aligned}
\tag{52}
$$

At this point, we can express Eqs. 51 and 52 in terms of the contributions κ_B and κ_W (see Eq. 46) as follows

$$
\begin{aligned}
\frac{D\kappa_B}{Dt} &= F_B - D_B - \Pi, \\
\frac{D\kappa_W}{Dt} &= F_W - D_W + \Pi,
\end{aligned}
\tag{53}
$$

where F is the energy injected by external forces, and D is the viscous energy dissipation rate. Finally, similarly to what we found for the equations of motion (Eqs. 42 and 43), the **production term** (Π) appears on both equations with opposite sign, hence it represents the mutual exchange of energy between the BM and IGW domains, so that when $\Pi > 0$, kinetic energy is transferred from BM to IGW, and when $\Pi < 0$, kinetic energy is transferred from IGW to BM. The production term Π is given by

$$
\Pi = -\tau_{ij} \frac{\partial \{u_i\}_B}{\partial x_j} = \{\{u_i\}_W \{u_j\}_W\}_B \frac{\partial \{u_i\}_B}{\partial x_j},
\tag{54}
$$

which, if we only account for the horizontal components of the velocity field (i.e. the sum over indices i, j only ranges from 1 to 2), it becomes the **horizontal production term**

$$
\Pi = -\tau_{ij} S_{ij} = -\left[\{U_W U_W\}_B \frac{\partial U_B}{\partial x} + \{V_W V_W\}_B \frac{\partial V_B}{\partial y} + \{U_W V_W\}_B \left(\frac{\partial U_B}{\partial y} + \frac{\partial V_B}{\partial x} \right) \right],
\tag{55}
$$

where

$$
S_{ij} = \frac{1}{2} \left(\frac{\partial \{u_i\}_B}{\partial x_j} + \frac{\partial \{u_j\}_B}{\partial x_i} \right)
\tag{56}
$$

is the strain rate tensor of the BM velocity field.

Unlike other approaches that also apply filtering operations the motion equations and velocity components of the field (Barkan et al., 2017; Johnson, 2020), due to the nature of the filter we are proposing this time, our interpretation of the production term Π differs from other results since it does not capture kinetic energy exchange across temporal or spatial scales alone, but it describes the energy exchange between BM and IGW by means of a spatio-temporal filtering. This is because, in our case, the cutoff frequency depends on the IGW dispersion relation where the frequency ω_c is a function of horizontal wavenumber (as per Eq. 6). Moreover, if we inspect closely the production term (Eq. 54), and consider that the stress tensor τ_{ij} arises from the nonlinear (IGW wave-wave) interactions projected onto the BM regime, we find out that the KE exchange is given by the BM strain tensor S_{ij} (Eq. 56) *modulated* by the stress tensor τ_{ij} waves.

Summing up:

- Π quantifies the exchange of kinetic energy between the BM and IGW components of the velocity field.
- When $\Pi > 0$, energy is transferred from BM to IGW. This is, IGW gains and BM loses KE.
- When $\Pi < 0$, energy is transferred from IGW to BM. This is, BM gains and IGW loses KE.
- Π is one of the many terms that impact the total KE evolution, so we can expect it to correlate with its evolution to a certain extent only.
- Given its dependency on terms with origin in both BM and IGW regimes, the KE exchange is zero when at least one of the two components is zero. This means that BM and IGW must coincide in space and time in order to exchange kinetic energy, and that Π does not consider any potential *transformation* of KE from one kind to the other.

4.2 Kinetic energy exchange between BM and IGW

To get some insight on what phenomena have more influence on the total Π, we first analyse Eq. 55 term by term for the Canary current around 26 °N on February 2012. The first aim is to understand the contribution of each of these terms, namely

$$\Pi_{xx} = -\tau_{xx} S_{xx} = -\left\{U_W U_W\right\}_B \frac{\partial U_B}{\partial x}, \tag{57a}$$

$$\Pi_{yy} = -\tau_{yy} S_{yy} = -\left\{V_W V_W\right\}_B \frac{\partial V_B}{\partial y}, \tag{57b}$$

$$\Pi_{xy} = -\tau_{xy} S_{xy} - \tau_{yx} S_{yx} = -\left\{U_W V_W\right\}_B \left(\frac{\partial U_B}{\partial y} + \frac{\partial V_B}{\partial x}\right), \tag{57c}$$

where the components of the stress (τ_{ij}) and strain ($\S_{ij}$) tensors are given by

$$\tau_{xx} = \{U_W U_W\}_B\,, \tag{58a}$$

$$\tau_{yy} = \{V_W V_W\}_B\,, \tag{58b}$$

$$\tau_{xy} = \tau_{yx} = \{U_W V_W\}_B\,, \tag{58c}$$

$$S_{xx} = \frac{\partial U_B}{\partial x}, \tag{58d}$$

$$S_{yy} = \frac{\partial V_B}{\partial y}, \tag{58e}$$

$$S_{xy} = S_{yx} = \frac{1}{2}\left(\frac{\partial U_B}{\partial y} + \frac{\partial V_B}{\partial x}\right). \tag{58f}$$

To provide a complete overview, we begin by comparing the Canary (Figs 14 and 15) and Benguela (Figs. 16 and 17) currents, during summer and winter seasons 2012. The choice of these two currents to compare them was made considering they are, among the four EBC we study here, the most distinct; while Benguela is mostly dominated by waves, Canary current tends to have intense BM activity, even at submesoscales (SBM).

From these snapshots, we can identify the patterns in all our study areas share: the κ_B contribution to the total KE_B is significantly higher than κ_W, whereas the latter is not negligible in some cases; since the stresses τ_{xx} and τ_{yy} are notably stronger than τ_{xy}, the terms Π_{xx} and Π_{yy} tend to account for most of the total KE exchange, although the shear stress S_{xy} component of the strain tensor is stronger than the expansion/compression terms S_{xx} and S_{yy}; lastly, as τ_{ij} originates in the IGW regime and S_{ij} is derived from the BM fields, there is no significant difference between the total Π in summer and winter seasons.

For the sake of completeness, we will also show snapshots of the Π and its contributions for the California (Fig. 18) and Peru–Chile (Fig. 19) currents during the winter season, and the breakdown of their production term Π into the Π_{ij} components. From these figures, we encounter the same pattern we have found so far: as California and Peru–Chile are less energetic than Canary but more than Benguela, then Π clearly follows the same tendency as the amount of kinetic energy exchanged (or to be exchanged) depends directly on the amount of *available kinetic energy* on both regimes. At this point, we consider it would be redundant to present the corresponding snapshots for the summer season, as these currents follow the same seasonal variation.

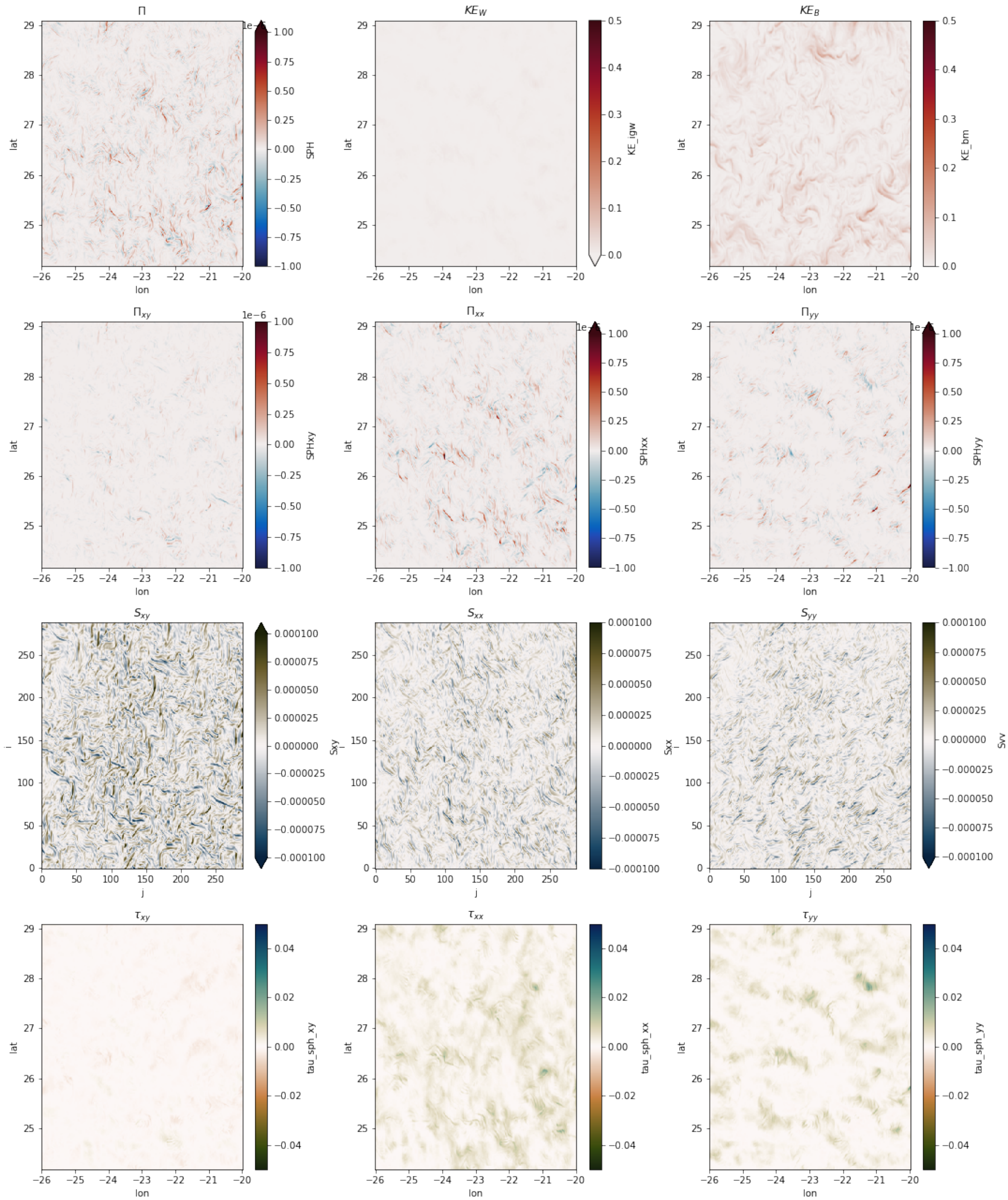

Figure 14. KE exchange (Π, upper left), contribution to the KE in the BM regime by IGW (κ_W, upper center) and BM (κ_B, upper right), compared with Π_{xy} (second row, left), Π_{xx} (second row, center) and Π_{yy} (second row, right), along with the components of the strain rate tensor S_{xy} (third row left), S_{xx} (third row center) and S_{yy} (third row right) and the IGW stress tensorτ_{xy} (lower left), τ_{xx} (lower center) and τ_{yy} (lower right). All snapshots correspond to the area centred around 26.6 °N within the Canary current, during the winter season (March 1st 2012, 17:00 local time).

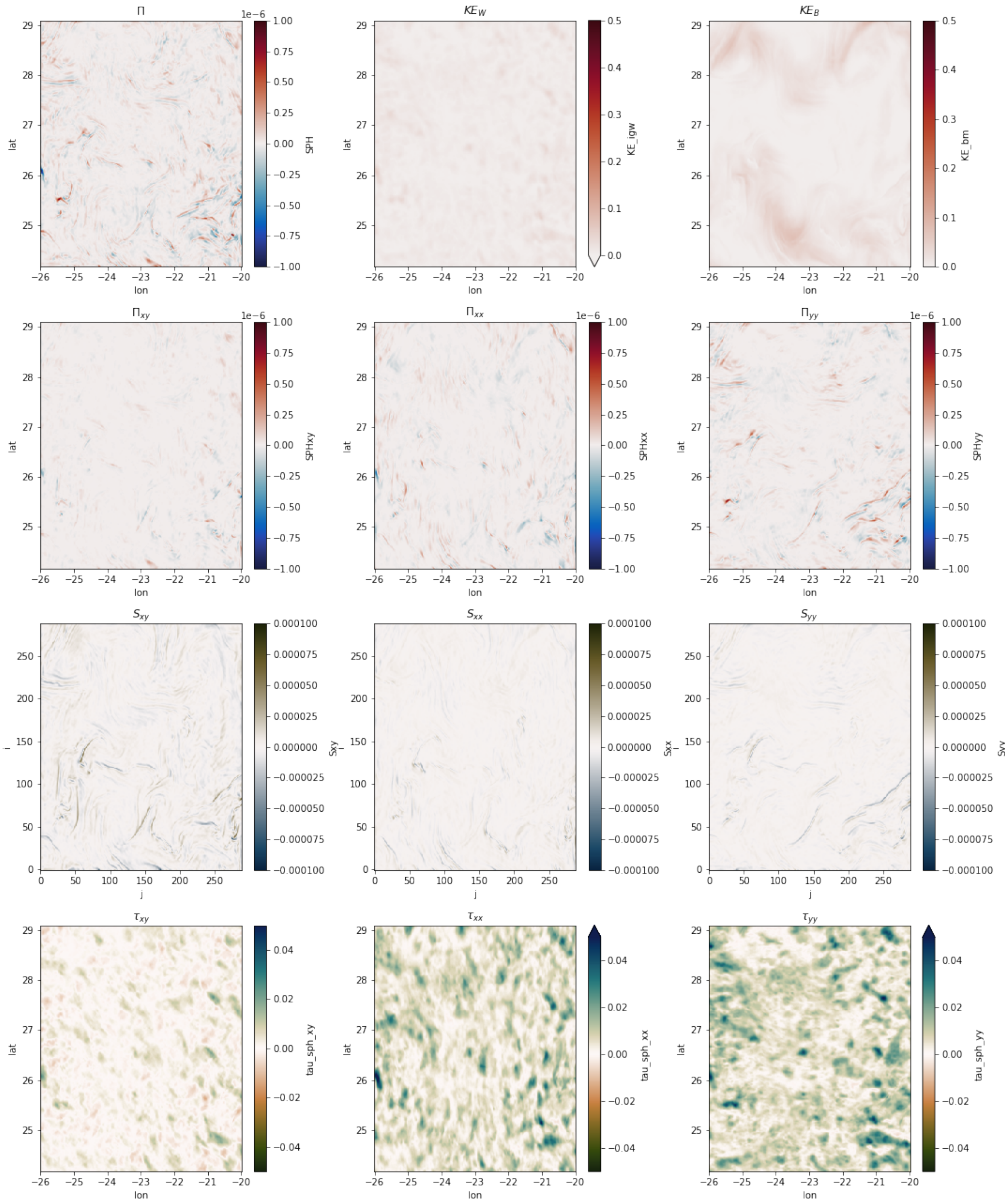

Figure 15. KE exchange (Π, upper left), contribution to the KE in the BM regime by IGW (κ_W, upper center) and BM (κ_B, upper right), compared with Π_{xy} (second row, left), Π_{xx} (second row, center) and Π_{yy} (second row, right), along with the components of the strain rate tensor S_{xy} (third row left), S_{xx} (third row center) and S_{yy} (third row right) and the IGW stress tensorτ_{xy} (lower left), τ_{xx} (lower center) and τ_{yy} (lower right). All snapshots correspond to the area centred around 26.6 °N within the Canary current, during the summer season (September 1st 2012, 17:00 local time).

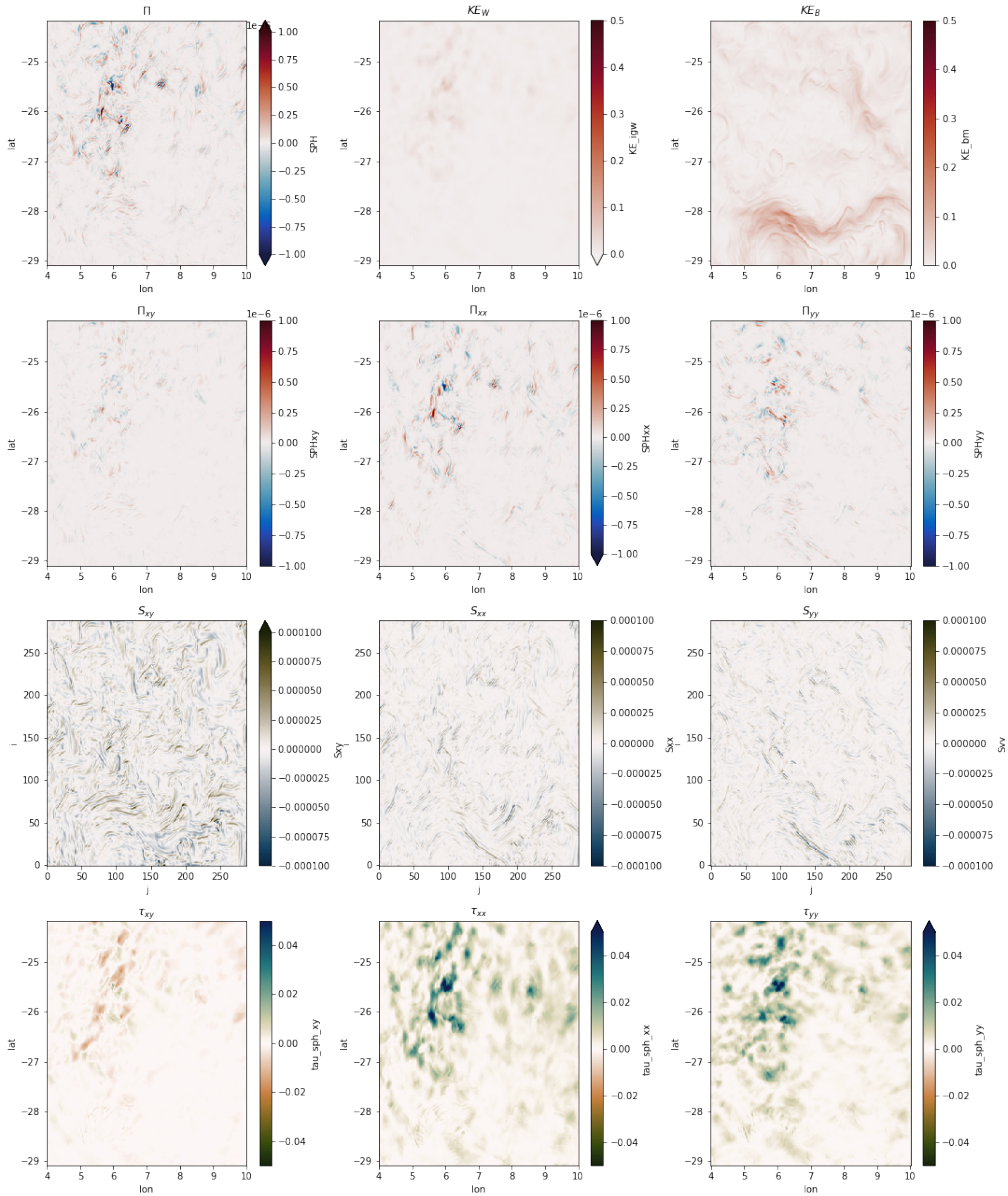

Figure 16. KE exchange (Π, upper left), contribution to the KE in the BM regime by IGW (κ_W, upper center) and BM (κ_B, upper right), compared with Π_{xy} (second row, left), Π_{xx} (second row, center) and Π_{yy} (second row, right), along with the components of the strain rate tensor S_{xy} (third row left), S_{xx} (third row center) and S_{yy} (third row right) and the IGW stress tensorτ_{xy} (lower left), τ_{xx} (lower center) and τ_{yy} (lower right). All snapshots correspond to the area centred around 26.6 °S within Benguela current, during the winter season (September 1st 2012, 15:00 local time).

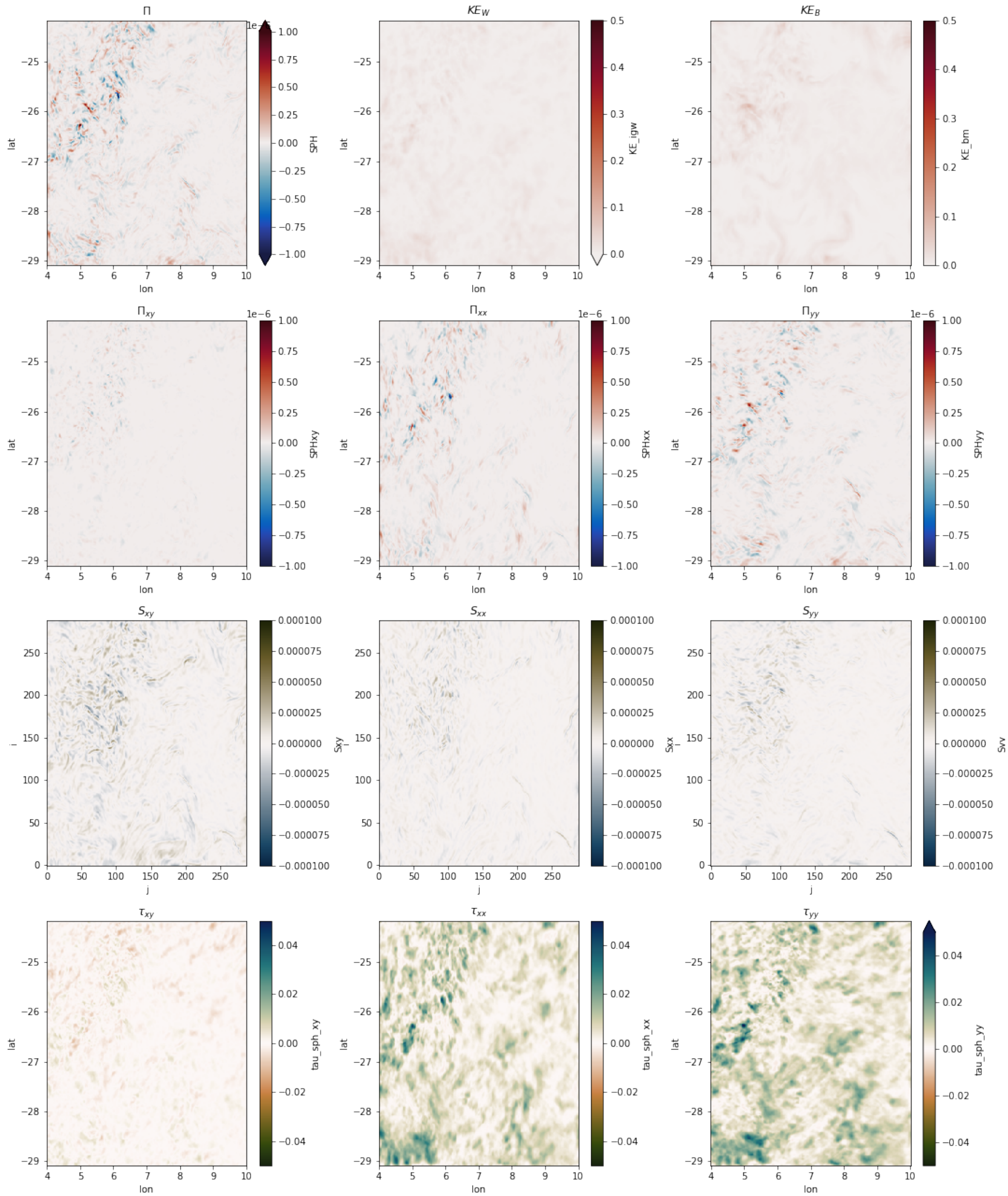

Figure 17. KE exchange (Π, upper left), contribution to the KE in the BM regime by IGW (κ_W, upper center) and BM (κ_B, upper right), compared with Π_{xy} (second row, left), Π_{xx} (second row, center) and Π_{yy} (second row, right), along with the components of the strain rate tensor S_{xy} (third row left), S_{xx} (third row center) and S_{yy} (third row right) and the IGW stress tensorτ_{xy} (lower left), τ_{xx} (lower center) and τ_{yy} (lower right). All snapshots correspond to the area centred around 26.6 °S within the Benguela current, during the summer season (March 1st 2012, 17:00 local time).

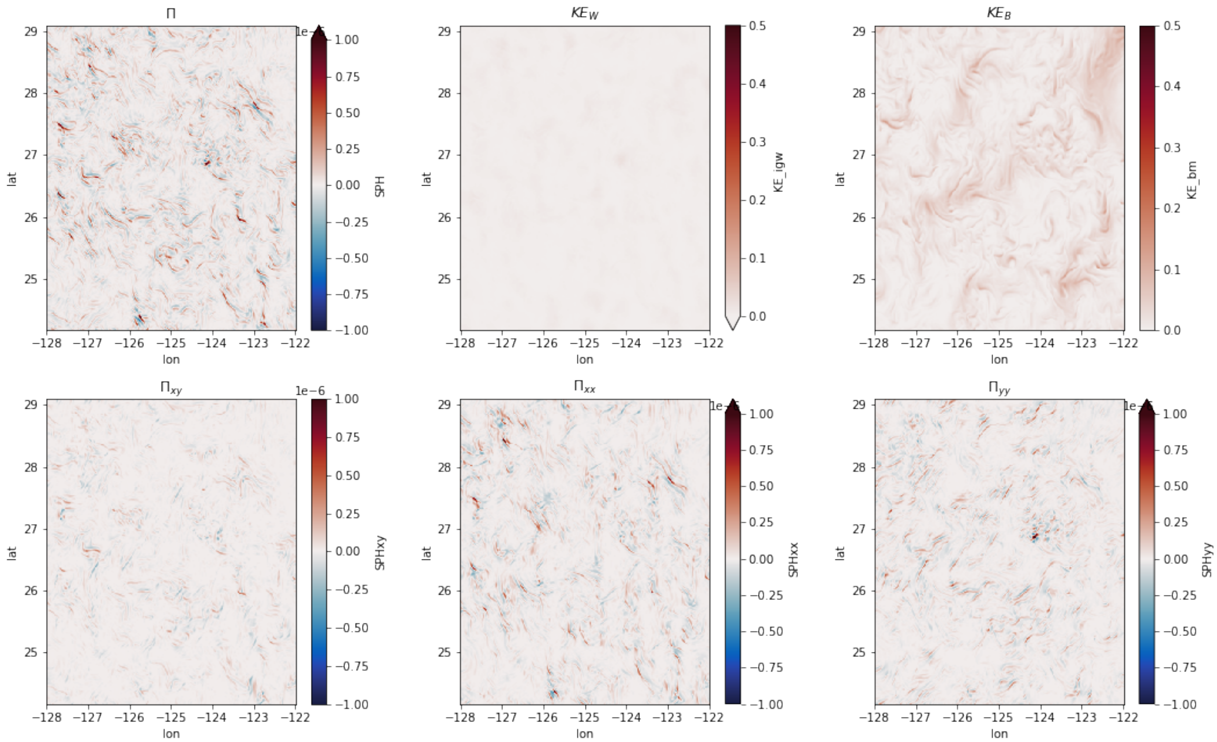

Figure 18. KE exchange (Π, upper left), contribution to the KE in the BM regime by IGW (κ_W, upper center) and BM (κ_B, upper right), compared with Π_{xy} (second row, left), Π_{xx} (second row, center) and Π_{yy} (second row, right), along with the components of the strain rate tensor S_{xy} (third row left), S_{xx} (third row center) and S_{yy} (third row right) and the IGW stress tensorτ_{xy} (lower left), τ_{xx} (lower center) and τ_{yy} (lower right). All snapshots correspond to the area centred around 26.6 °N within the California current, during the winter season (March 1st 2012, 17:00 local time).

4.2.1 KE exchange: structure and contribution to the energy equation

Given the role the strain tensor plays in the production term Π, it is natural to ask ourselves how the normal and shear stresses impact the KE exchange. By looking at the Eqs. **??** and the figures in the section above (14, 15, 16, 17, 18 and 19), we can infer that Π is favoured by higher values of the normal component of the strain tensor

$$s_n = \frac{\partial u_B}{\partial x} - \frac{\partial v_B}{\partial y} = S_{xx} - S_{yy}, \tag{59}$$

while, on the other hand, the shear component

$$s_s = \frac{\partial v_B}{\partial x} + \frac{\partial u_B}{\partial y} = S_{xy} \tag{60}$$

also contributes to the KE exchange, but not as much as the normal component s_n.

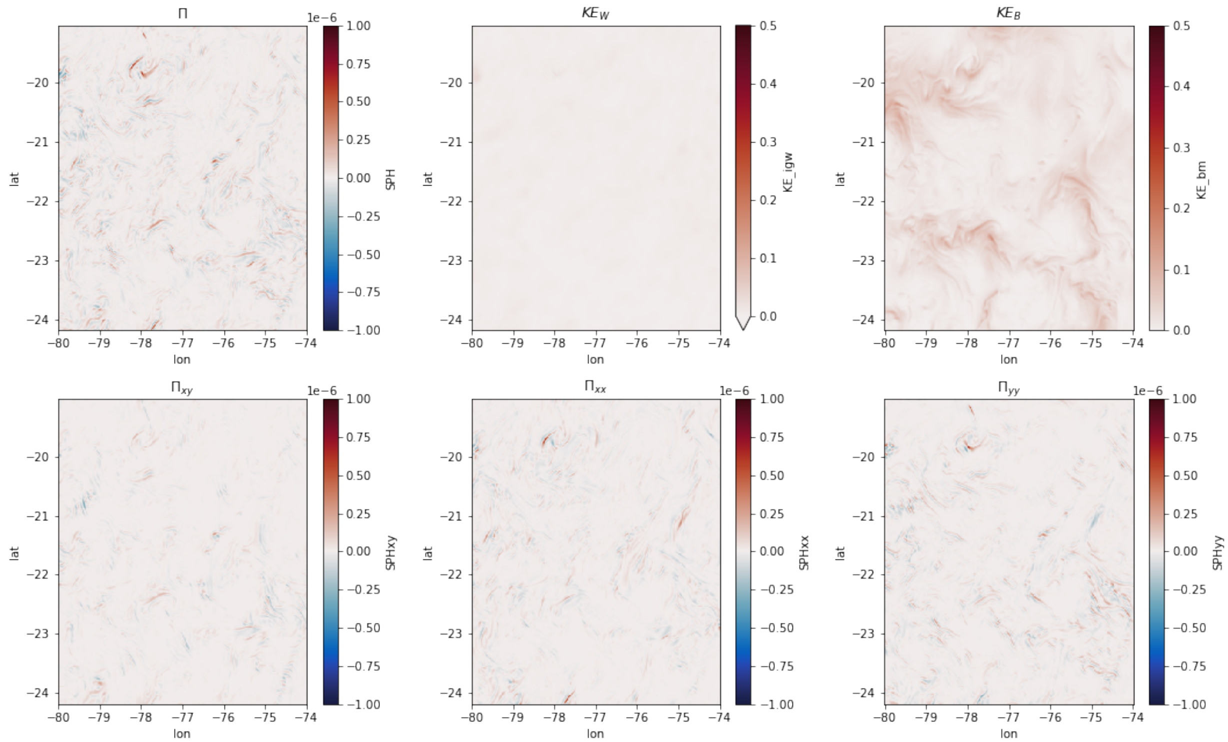

Figure 19. KE exchange (Π, upper left), contribution to the KE in the BM regime by IGW (κ_W, upper center) and BM (κ_B, upper right), compared with Π_{xy} (second row, left), Π_{xx} (second row, center) and Π_{yy} (second row, right), along with the components of the strain rate tensor S_{xy} (third row left), S_{xx} (third row center) and S_{yy} (third row right) and the IGW stress tensorτ_{xy} (lower left), τ_{xx} (lower center) and τ_{yy} (lower right). All snapshots correspond to the area centred around 21 °S within the Peru–Chile current, during the winter season (September 1st 2012, 17:00 local time).

Overall, we could expect the exchange of KE to be promoted or correlated to strain-dominated regions of the velocity field.

An important question to address is the validity and significance of our mathematical framework and the calculations concerning the kinetic energy (KE) exchange between balanced motions (BM) and internal gravity waves (IGW). First, upon examining the energy equations (Eqs. 51 and 52), along with their simplified form (Eq. 53) it becomes evident that Π is merely one among numerous factors influencing the evolution of κ_B (or reciprocally, κ_W). Second, more precise formulations of the motion and energy equations can potentially be developed by deviating from the hydrostatic approximation; this could include considering stratification effects, incorporating vertical velocities, and other factors. Last, it is essential to recognise that we cannot presume a significant contribution from Π to the motion and energy equations, even in the EBC where IGW kinetic energy is about the same order of magnitude of BM KE. To validate our results, we approximated the total time derivative of κ_B (considering the advection terms with U_B only) and compared it with the KE exchange term, and calculated its correlation with Π, so this approximation aids in assessing the influence of Π the energy exchange process.

We address the questions above for the Canary (26.6 °N, Figs. 20, 21) and Benguela (26.6 °S, 22 and 23) currents. First, on the first rows, we compare the corresponding snapshots of the KE exchange term (upper left), the estimated time derivative (upper right), and the Okubo-Weiss parameter for the BM field

$$OW_B = \frac{s_n^2 + s_s^2 - \omega^2}{f^2}, \tag{61}$$

where f is the local Coriolis parameter (as the normalisation factor), ω is the BM relative vorticity (RV_B), and s_n and s_s are given by Eqs 60 and 59, respectively. The Okubo-Weiss parameter separates the flow into regions dominated by relative vorticity ($OW_B < 0$) or by strain ($OW_B > 0$), then it will help us determine whether Π is more likely to occur near areas with relatively high strain. Also, we include the estimated total time derivative of κ_B (lhs of Eq. 53). Finally, in order to provide the full picture of these relations, we include in the panels below the JPDF of Π with the time derivative of κ_B (left) and the Okubo-Weiss parameter (right), where the former PDF also includes the Pearson correlation coefficient and its corresponding the p-value (where $p = 0.01$, for instance, would imply there is 1% chance the correlation is not statistically significant).

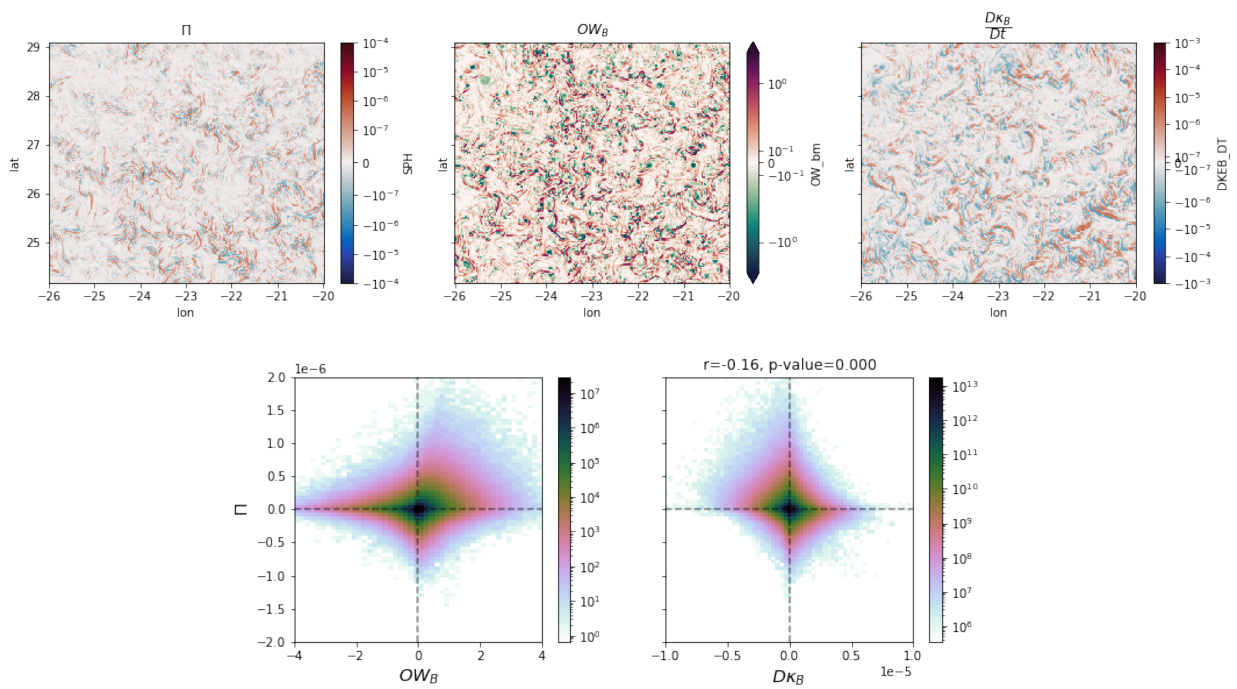

Figure 20. Up: KE exchange term (Π, left), BM Okubo-Weiss parameter (OW_B, center) and estimated ($\frac{D\kappa_B}{Dt}$, right) at to the area centred around 26.6 °N within the Canary current on March 1st 2012, 17:00 local time. Down: JPDF of Π with OW_B. (left) and $\frac{D\kappa_B}{Dt}$ (right) for the whole winter. Unlike figures above, Logarithmic scales were used in the upper panels.

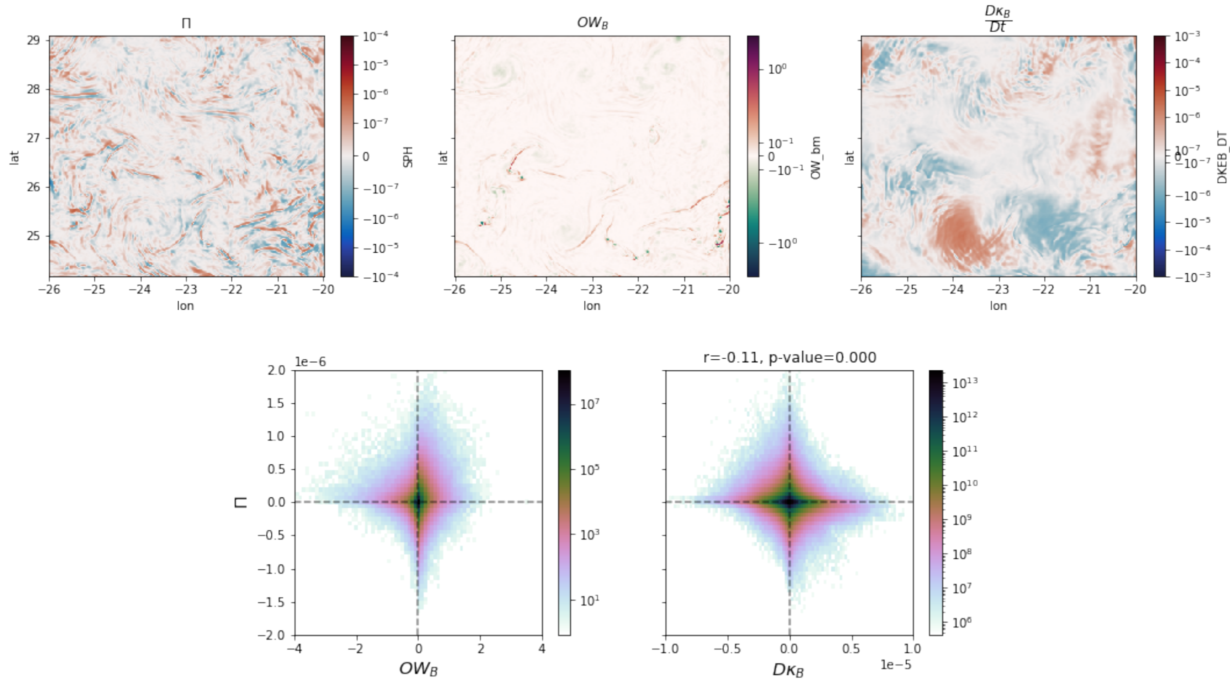

Figure 21. Up: KE exchange term (Π, left), BM Okubo-Weiss parameter (OW_B, center) and estimated ($\frac{D\kappa_B}{Dt}$, right) at to the area centred around 26.6 °N within the Canary current on September 1st 2012, 17:00 local time. Down: JPDF of Π with OW_B. (left) and $\frac{D\kappa_B}{Dt}$ (right) for the whole summer. Logarithmic scales were used in the upper panels.

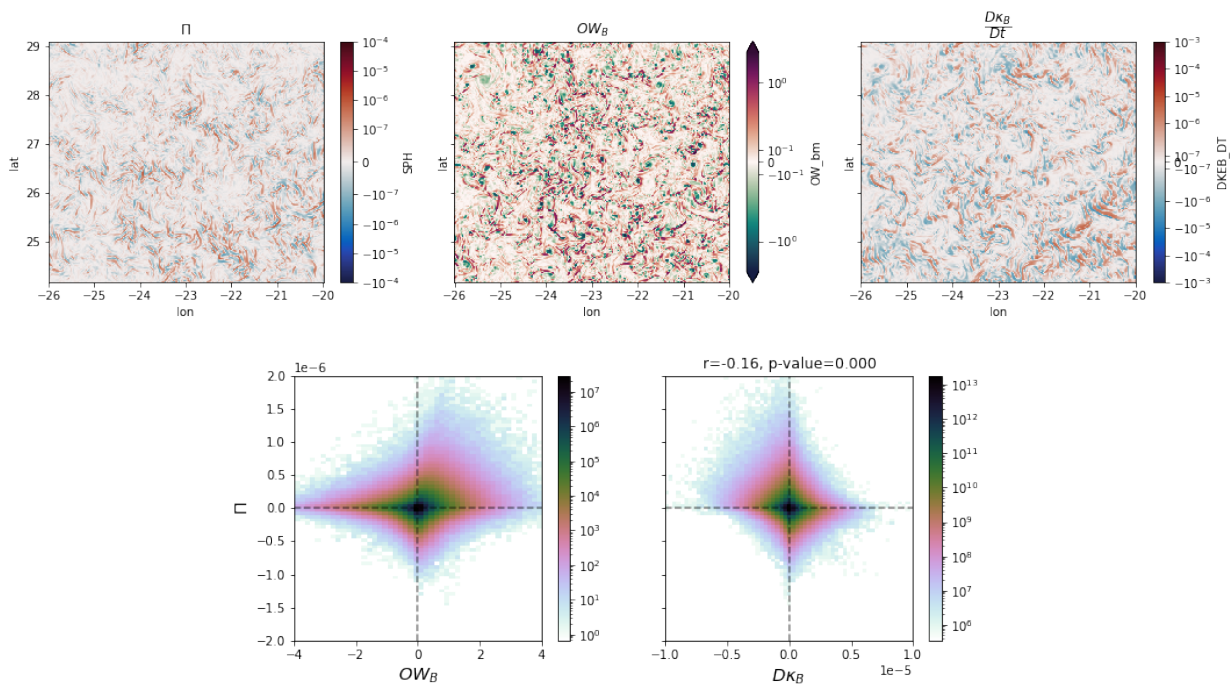

Figure 22. Up: KE exchange term (Π, left), BM Okubo-Weiss parameter (OW_B, center) and estimated ($\frac{D\kappa_B}{Dt}$, right) at to the area centred around 26.6 °S within the Benguela current on September 1st 2012, 17:00 local time. Down: JPDF of Π with OW_B. (left) and $\frac{D\kappa_B}{Dt}$ (right) for the whole winter. Logarithmic scales were used in the upper panels.

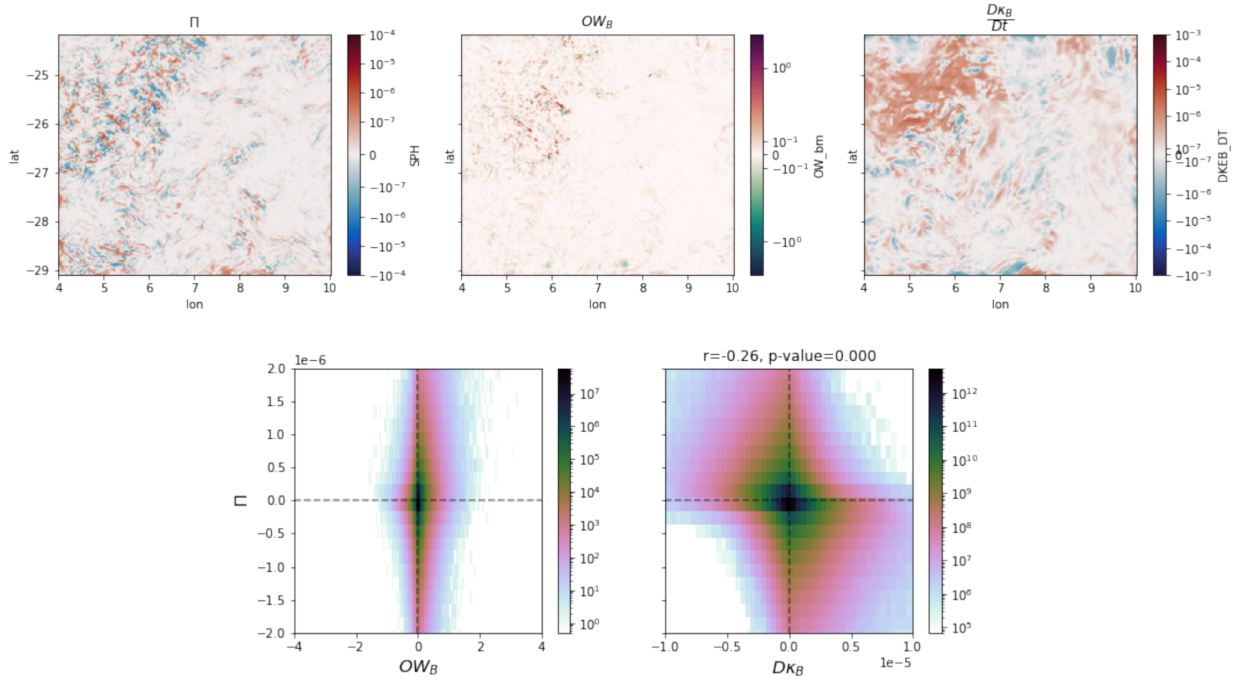

Figure 23. Up: KE exchange term (Π, left), BM Okubo-Weiss parameter (OW_B, center) and estimated ($\frac{D\kappa_B}{Dt}$, right) at to the area centred around 26.6 °N within the Benguela current on March 1st 2012, 17:00 local time. Down: JPDF of Π with OW_B. (left) and $\frac{D\kappa_B}{Dt}$ (right) for the whole summer. Logarithmic scales were used in the upper panels.

Despite the contribution of Π is about an order of magnitude smaller than the total $\frac{D\kappa_B}{Dt}$, the Pearson correlation (r, with extremely low p-values) captures two important factors. First, Π is correlated negatively (with r between -0.1 and -0.3) with the evolution of the total BM KE, which confirms that positive values of Π imply that KE is transferred *from* the BM to the IGW (JPDF in the second quadrant, lower right panels), although it does not happen that often in the inverse direction (fourth quadrant of the same JPDF). Second, in winter, where submesoscales are stronger, KE exchange is enhanced in strain-dominated areas even though IGW (hence τ_{ij} stresses) are weak compared to summer; during summer, by contrast, intense IGW compensate weaker strain fields, giving place to exchange terms of similar orders of magnitude than in winter.

In addition to the snapshots, JPDF and correlations shown above, we made the same calculations for all the 16 areas of the EBC analysed in this work. Table 2 consolidates the correlations between the estimated total time derivative of the BM KE contribution ($\frac{D\kappa_B}{Dt}$) and the KE exchange term Π.

Table 2. Pearson coefficient (r) and p-value (rounded to 2 decimal digit) between estimated total time derivative of the BM kinetic energy (κ_B) and the BM-IGW exchange term (Π) by current, centre (latitude, longitude), and season for each quadrangular area examined. Rows in bold mark the study areas compared in this thesis work, typically near 26 °N or 26 °S.

			Summer		Winter	
Current	Latitude	Longitude	r	p-value	r	p-value
California	48.4 °N	137 °W	-0.01	0.00	0.00	0.00
California	44.5 °N	131 °W	-0.06	0.00	-0.03	0.00
California	40.4 °N	131 °W	-0.06	0.00	-0.03	0.00
California	36.05 °N	131 °W	-0.13	0.00	-0.04	0.00
California	31.46 °N	125 °W	-0.08	0.00	-0.07	0.00
California	**26.64 °N**	**125 °W**	**-0.19**	**0.00**	**-0.13**	**0.00**
Canary	31.46 °N	23 °W	-0.09	0.00	-0.06	0.00
Canary	**26.64 °N**	**23 °W**	**-0.11**	**0.00**	**-0.16**	**0.00**
Canary	21.61 °N	23 °W	-0.10	0.00	-0.18	0.00
Canary	16.40 °N	29 °W	-0.15	0.00	-0.19	0.00
Peru–Chile	16.39 °S	83 °W	-0.19	0.00	-0.20	0.00
Peru–Chile	**21.61 °S**	**77 °W**	**-0.26**	**0.00**	**-0.18**	**0.00**
Peru–Chile	40.41 °S	83 °W	-0.10	0.00	-0.09	0.00
Benguela	11.03 °S	7 °E	-0.16	0.00	-0.13	0.00
Benguela	16.39 °S	7 °E	-0.27	0.00	-0.22	0.00
Benguela	**26.64 °S**	**7 °E**	**-0.25**	**0.00**	**-0.15**	**0.00**

4.3 Discussion

In the previous section, we developed and tested the usefulness of a dynamical filter that successfully separates the motion into balanced motions (BM) and internal gravity waves (IGW). The filter was capable of isolating submesoscale BM (SBM), in such a way that we were able to capture, for instance, the effects of turbulent transient thermal wind (TTTW) balance. Here, we applied it to investigate the main topic of this thesis: kinetic energy exchange between BM and IGW. This is, by means of the BM-IGW filtering approach, in analogy to the treatment we borrowed from turbulence theory, and following Monin & Yaglom (1979); Germano (1992); Johnson (2020), we arrived to equations of motion and energy for the BM regime, which included a shared term between the BM and IGW equations: the KE exchange term Π.

Before quantifying the exchange term itself, we broke it down into its different components. Such dissection allowed us to identify that Π does not account for kinetic energy *generation* but *exchange*, this means that BM and IGW need to coexist at a given instant and point in space. From the BM standpoint, KE transfer from BM to IGW is enhanced by the presence of strong normal strain fields, but it is not a sufficient condition for it to occur; IGW-wise, the KE exchange arises from nonlinear (wave-wave) IGW stress.

When we compared winter and summer seasons, we found high strain BM fields have a greater impact on Π in winter than in summer, where SBM are weaker, while IGW are more dominant in summer so the IGW stress tends to compensate lower BM activity. In this regard, even though all elements in the BM strain tensor S_{ij} are about the same order, off-diagonal elements of the IGW stress tensor

$$\tau_{ij} = \left\{ \{u_i\}_W \{u_j\}_W \right\}_B \tag{62}$$

are much smaller than its diagonal elements. Lastly, while IGW drive KE exchange in both directions (positive and negative values of Π were found), the presence of normal strain fields tend to promote KE transference to the IGW regime.

It is worth considering that the Π term is analogous to the turbulent kinetic energy (TKE) production term in the Reynolds-averaged Navier-Stokes (RANS) equations, which is described by a similar equation as the one we derived for Π, with the difference that the stresses τ_{ij} in turbulence theory are given by cross-covariance of the turbulent fields. Thus, in analogy with turbulence theory, we can say that IGW exert viscous stresses on the BM field by means of wave-wave interactions, which give rise to KE exchange between BM and IGW since, unlike molecular viscosity that only dissipates kinetic energy, this viscosity can be either positive or negative. Motivated by this analogy, our results could leave the door open to find ways to parameterise these IGW stresses in terms of the BM field, in a similar fashion as we currently parameterise viscous turbulence in terms of the mean field only, with the aim to solve the closure problem presented by including additional (in principle unknown and unresolved) variables.

4.3.1 How does this apply to other currents?

Given the results we presented for the Eastern Boundary Currents, one might be encouraged to ask whether our methodology and results can be extended to currents that do not necessarily share the same features with the EBC. Since this is a valid concern and, should it proves successful, it could add more value to ours methods and results, we followed the entire workflow for an area within the Kuroshio extension, a Western Boundary Current or WBC. WBCs, in contrast to EBC, have orders of magnitude more kinetic energy and are dominated by BM in the meso and submesoscale ranges. To make the comparison valid enough and to prevent the colorbar ranges in the plots to override, we took an area 7° south of the highest intensity current stream; although, our results remain valid as longs as we are close to the current stream to capture the features of interest.

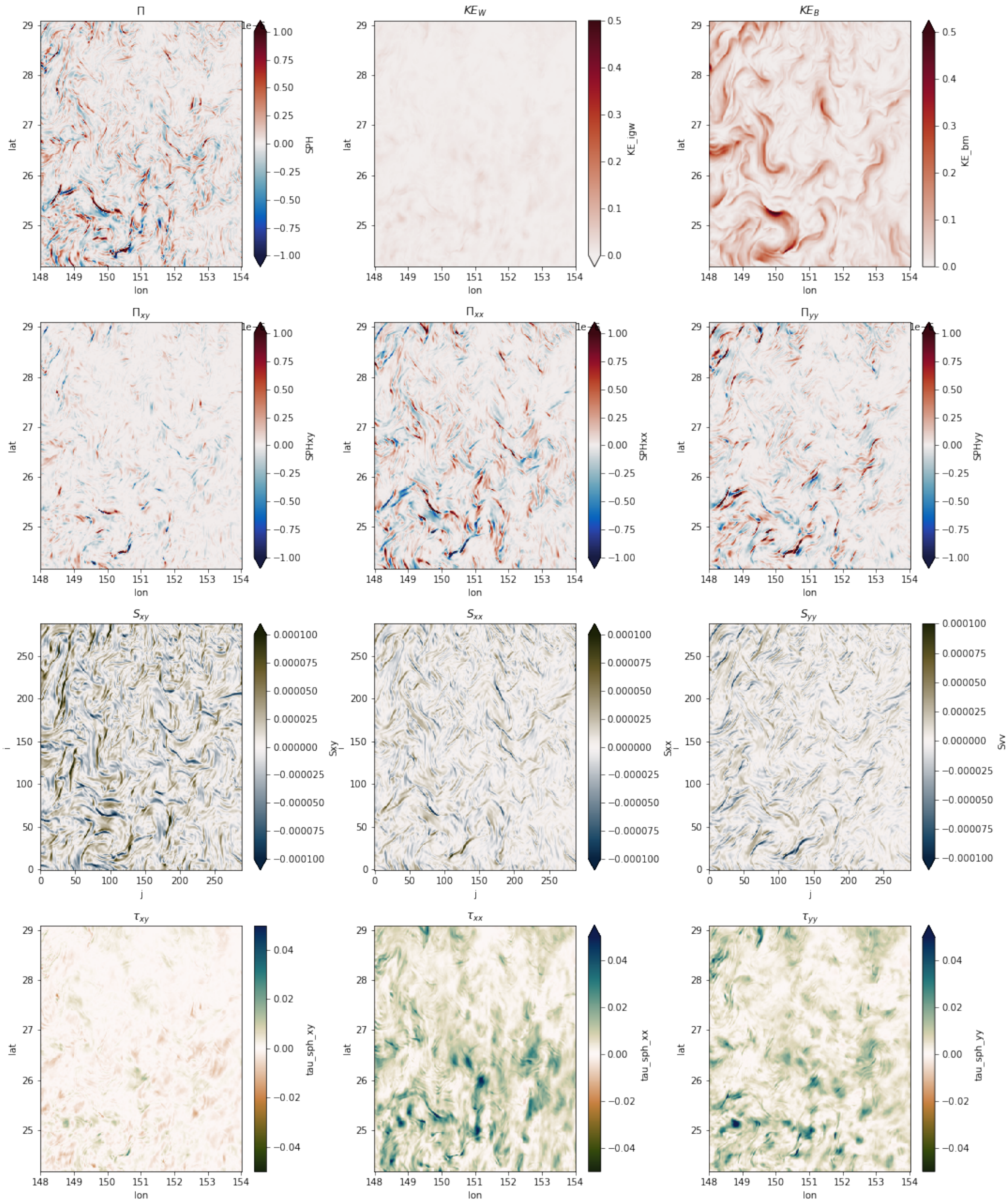

Figure 24. KE exchange (Π, upper left), contribution to the KE in the BM regime by IGW (κ_W, upper center) and BM (κ_B, upper right), compared with Π_{xy} (second row, left), Π_{xx} (second row, center) and Π_{yy} (second row, right), along with the components of the strain rate tensor S_{xy} (third row left), S_{xx} (third row center) and S_{yy} (third row right) and the IGW stress tensorτ_{xy} (lower left), τ_{xx} (lower center) and τ_{yy} (lower right). All snapshots correspond to the area centred around 26.6 °N within the Kuroshio current, during the winter season (March 1st 2012, 17:00 local time).

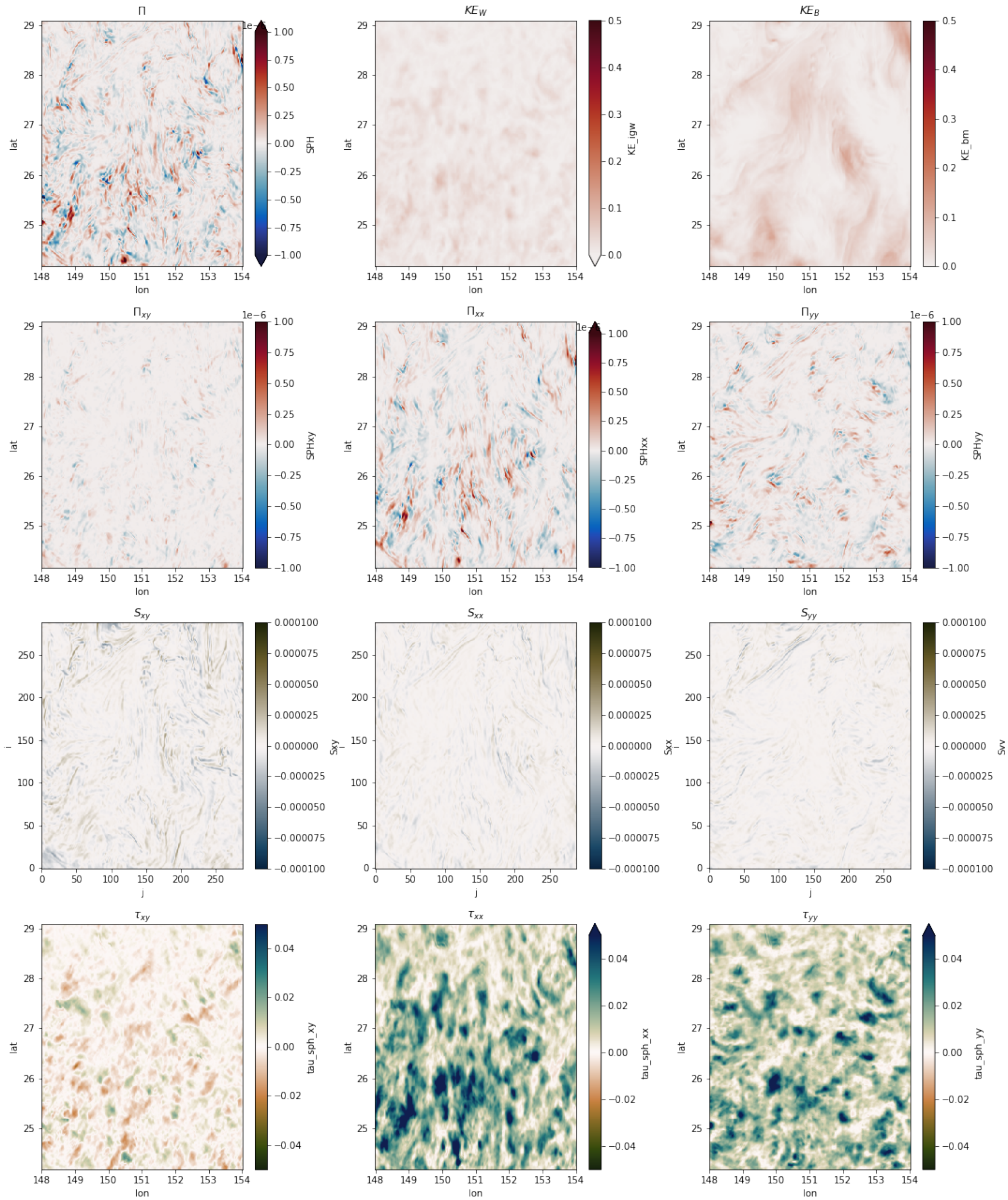

Figure 25. KE exchange (Π, upper left), contribution to the KE in the BM regime by IGW (κ_W, upper center) and BM (κ_B, upper right), compared with Π_{xy} (second row, left), Π_{xx} (second row, center) and Π_{yy} (second row, right), along with the components of the strain rate tensor S_{xy} (third row left), S_{xx} (third row center) and S_{yy} (third row right) and the IGW stress tensorτ_{xy} (lower left), τ_{xx} (lower center) and τ_{yy} (lower right). All snapshots correspond to the area centred around 26.6 °N within the Kuroshio current, during the summer season (September 1st 2012, 17:00 local time).

As Fig. 24 demonstrates, all the dynamical features of the BM and the Π are well-isolated by the same dynamical filtering strategy we followed for the EBC. In addition, since the BM are even more energetic than the Canary current, the available KE to be converted into IGW by strengthening or weakening fronts and the strain field is higher, hence the Π term ends up being more prominent in these regions.

The results below are a clear indicator that we can apply and extend our method to study areas with different physical features than the EBC, always bearing in mind the limitations of the methodology itself. Furthermore, it is crucial to highlight the potential that can be harnessed by implementing and enhancing the dynamic filtering we proposed in this thesis, particularly when applied to facilitate more comprehensive analyses or parameterisations of the interactions between BM-IGW.

Chapter 5. Conclusions

BM and IGW are the two main classes of oceanic motion, since they encompass most of the different phenomena observed there and, consequently, account for most of the kinetic energy (Klein et al., 2019). Although different in nature, there have been found to be interactions between these two dynamical regimes, so the interest in studying and understanding BM and IGW has increased in recent years (Chereskin et al., 2019; Klein et al., 2019; Torres et al., 2018; Qiu et al., 2018).

This work contributes to an improvement in the understanding of the Eastern Boundary Currents in the BM regime. The temporal evolution of BM within these currents was characterised by means of a dynamical filtering to separate IGW from BM, even in the presence of intense IGW signals that might in principle interfere with high-frequency submesoscale BM. Additionally, we identified submesoscale features such as diurnal changes in the eddy viscosity induced by ocean surface heat flux. Finally, we found evidence of energetic exchange between both regimes, even though EBC are known for being low-energy currents dominated by linear IGW.

The main lesson from our work is twofold. First, within relative low-energy regions such as the EBC, IGW overshadow strong, quasi diurnal submesoscale activity, mainly driven by atmospheric and seasonal forcings. Second, also as a consequence of relatively high-energy IGW in these regions, kinetic energy exchange from and to the BM regime is present through the whole year, with a greater tendency by BM to yield their KE energy to IGW in winter, influenced by high strain submesoscale fields.

Currently, highly realistic ocean numerical simulations are continuously running, both regionally and globally. Simulations are capable of resolving submesoscale dynamics and the internal gravity wave continuum. It is critical to separate BM from IGW to achieve accurate vertical heat flux estimates induced by BM at low and high frequencies. The method we propose in this thesis work can be applied at any vertical level in the water column, opening up the possibility of separating IGW and deep-reaching submesoscale balanced motions (Siegelman et al., 2020; Yu et al., 2019) (whose vertical scale is larger than the mixed-layer depth) and quantifying their respective contributions to vertical heat fluxes. Additional concerns may exist regarding the interaction between IGW and BM motions, such as inertial (or near-inertial) waves that are trapped by eddies. These interactions, however, would not have any impact on the filter. Conversely, analyses in the physical or spectral spaces of BM–IGW interactions could benefit from the separation of the dynamical regimes achieved by our method. Ultimately, our dynamical filtering and its application on the study of energetic interaction across dynamical regimes will contribute to the study of the interaction between IGW and submesoscale turbulent motions on data coming from realistic, high-resolution simulations, and could potentially be applied in comparisons among other dynamical regimes besides BM vs IGW.

The filtering function developed in this thesis succeeds at separating balanced motions (BM) from internal gravity waves (IGW), and offers further applications in the realm of oceanographic research and modelling. Firstly, it aids in enhancing our understanding of internal gravity waves by differentiating balanced motions from internal gravity waves. In this regard, the dynamical filter enables a more detailed analysis of IGW, since allows us to scrutinise the properties, propagation, and energy dispersion of IGW more accurately, thereby deepening our comprehension of their these processes. Secondly, it can contribute to improved parameterisation in ocean models that do not resolve IGW. Parameterisations represent simplified mathematical encapsulations of more complex physical processes, and their accuracy is key in emulating ocean behaviour in climate or regional ocean circulation models. The representation of IGW in these models can be enhanced, leading to more precise simulations of their impact on ocean circulation, mixing, and energy transport. Lastly, the filtering function and its properties facilitates an examination of their interactions with other oceanic phenomena, like mesoscale eddies, frontal systems, etc. Such investigations of interactions between IGW and these processes can yield insights into overall ocean dynamics and its influence on large-scale circulation patterns.

Bibliography

Abernathey, R., Dussin, R., Smith, T., Fenty, I., Bourgault, P., Bot, S., Doddridge, E., Goldsworth, F., Losch, M., Almansi, M., Jones, S., Uchida, T., Cimatoribus, A., Leskis, A., Quintana, A., Ponte, A., Rose, B., Balwada, D., Sérazin, G., & Brannigan, L. (2021). Mitgcm/xmitgcm: v0.5.1. https://doi.org/10.5281/zenodo.4574204.

Barkan, R., Winters, K., & McWilliams, J. (2017). Stimulated imbalance and the enhancement of eddy kinetic energy dissipation by internal waves. *Journal of Physical Oceanography*, 47(1). https://doi.org/10.1175/JPO-D-16-0117.1.

Biltoft, C. & Pardyjak, E. (2009). Spectral coherence and the statistical significance of turbulent flux computations. *Journal of Atmospheric and Oceanic Technology*, 26(2). https://doi.org/10.1175/2008JTECHA1141.1.

Chavez, F. & Messié, M. (2009). A comparison of Eastern Boundary Upwelling Ecosystems. *Progress in Oceanography*, 83(1-4). https://doi.org/10.1016/j.pocean.2009.07.032.

Chereskin, T., Rocha, C., Gille, S., Menemenlis, D., & Passaro, M. (2019). Characterizing the Transition From Balanced to Unbalanced Motions in the Southern California Current. *Journal of Geophysical Research: Oceans*, 124(3). https://doi.org/10.1029/2018JC014583.

Connolly, T., Hickey, B., Shulman, I., & Thomson, R. (2013). Coastal Trapped Waves, Alongshore Pressure Gradients, and the California Undercurrent. *Journal of Physical Oceanography*, 44(1). https://doi.org/10.1175/jpo-d-13-095.1.

Daru, V. & Tenaud, C. (2004). High order one-step monotonicity-preserving schemes for unsteady compressible flow calculations. *Journal of Computational Physics*, 193(2). https://doi.org/10.1016/j.jcp.2003.08.023.

Dauhajre, D. & McWilliams, J. (2018). Diurnal evolution of submesoscale front and filament circulations. *Journal of Physical Oceanography*, 48. https://doi.org/10.1175/JPO-D-18-0143.1.

Dauhajre, D., McWilliams, J., & Uchiyama, Y. (2017). Submesoscale coherent structures on the continental shelf. *Journal of Physical Oceanography*, 47(12). https://doi.org/10.1175/JPO-D-16-0270.1.

Dunphy, M., Ponte, A., Klein, P., & Le Gentil, S. (2017). Low-Mode Internal Tide Propagation in a Turbulent Eddy Field. *Journal of Physical Oceanography*, 47(3). https://doi.org/10.1175/jpo-d-16-0099.1.

Erickson, Z., Thompson, A., Callies, J., Yu, X., Garabato, A., & Klein, P. (2020). The vertical structure of open-ocean submesoscale variability during a full seasonal cycle. *Journal of Physical Oceanography*, 50(1). https://doi.org/10.1175/JPO-D-19-0030.1.

Ferrari, R. & Wunsch, C. (2009). Ocean Circulation Kinetic Energy: Reservoirs, Sources, and Sinks. *Annual Review of Fluid Mechanics*, 41(1). https://doi.org/10.1146/annurev.fluid.40.111406.102139.

Fox-Kemper, B. & Menemenlis, D. (2008). *Can Large Eddy Simulation Techniques Improve Mesoscale Rich Ocean Models?*, (pp. 319–337). American Geophysical Union (AGU).

Fréon, P., Barange, M., & Arístegui, J. (2009). Eastern boundary upwelling ecosystems: Integrative and comparative approaches. *Progress in Oceanography*, 83(1-4). https://doi.org/10.1016/j.pocean.2009.08.001.

Fu, L. & Ferrari, R. (2008). Observing oceanic submesoscale processes from space. *EOS, Transactions American Geophysical Union*, 89(48). https://doi.org/10.1029/2008EO480003.

Garrett, C. & Loder, J. (1981). Dynamical aspects of shallow sea fronts. *Philosophical Transactions of the Royal Society of London. Series A, Mathematical and Physical Sciences*, 302. https://doi.org/10.1098/RSTA.1981.0183.

Germano, M. (1992). Turbulence: the filtering approach. *Journal of Fluid Mechanics*, 238. https://doi.org/10.1017/S0022112092001733.

Gill, A. (1982). *Atmosphere-ocean dynamics*. Academic Press New York.

Gutiérrez, M., López, M., Candela, J., Castro, R., Mascarenhas, A., & Collins, C. (2014). Effect of coastal-trapped waves and wind on currents and transport in the gulf of California. *Journal of Geophysical Research*, 119(8). https://doi.org/10.1002/2013JC009538.

Hill, A., Hickey, B., Shillington, F., Strub, P., Brink, K., Barton, E., & Thomas, A. (1998). Eastern Ocean Boundaries, Coastal Segment (E). In Robinson, A. R. & Brink, K. H., editors, *The Sea: The Global Coastal Ocean: Regional Studies and Syntheses*, volume 11, chapter 2, (pp. 29–67). Harvard University Press, Boston, MA.

Hoskins, B. & Bretherton, F. (1972). Atmospheric frontogenesis models: Mathematical formulation and solution. *Journal of Atmospheric Sciences*, 29(1). https://doi.org/10.1175/1520-0469(1972)029%3C0011:AFMMFA%3E2.0.CO;2.

Hoyer, S. & Hamman, J. (2017). xarray: Nd labeled arrays and datasets in python. *Journal of Open Research Software*, 5(1). https://doi.org/10.5334/jors.148.

Huang, X., Wang, Z., Zhang, Z., Yang, Y., Zhou, C., Yang, Q., Zhao, W., & Tian, J. (2018). Role of Mesoscale Eddies in Modulating the Semidiurnal Internal Tide: Observation Results in the Northern South China Sea. *Journal of Physical Oceanography*, 48(8). https://doi.org/10.1175/jpo-d-17-0209.1.

Illig, S. & Bachèlery, M. (2019). Propagation of Subseasonal Equatorially-Forced Coastal Trapped Waves down to the Benguela Upwelling System. *Scientific Reports*, 9(1). https://doi.org/10.1038/s41598-019-41847-1.

Johnson, P. (2020). Energy transfer from large to small scales in turbulence by multiscale nonlinear strain and vorticity interactions. *Phys. Rev. Lett.*, 124. https://doi.org/10.1103/PhysRevLett.124.104501.

Klein, P. & Lapeyre, G. (2009). The Oceanic Vertical Pump Induced by Mesoscale and Submesoscale Turbulence. *Annual Review of Marine Science*, 1(1). https://doi.org/10.1146/annurev.marine.010908.163704.

Klein, P., Lapeyre, G., Siegelman, L., Qiu, B., Fu, L., Torres, H., Su, Z., Menemenlis, D., & Le Gentil, S. (2019). Ocean-Scale Interactions From Space. *Earth and Space Science*. https://doi.org/10.1029/2018EA000492.

Large, W., McWilliams, J., & Doney, S. (1994). Oceanic vertical mixing: A review and a model with a nonlocal boundary layer parameterization. *Reviews of Geophysics*, 32. https://doi.org/10.1029/94RG01872.

Mackas, D., Strub, P., Thomas, A., & Montecino, V. (2006). Eastern ocean boundaries pan-regional overview. In Robinson, A. R. & Brink, K. H., editors, *The sea, the Global Coastal Ocean*, volume 14A, (pp. 21–59). Harvard Press Ltd., Cambridge, MA.

McComb, W. (1990). *The Physics of Fluid Turbulence*. Oxford Engineering Science Series. Clarendon Press.

McWilliams, J. (2019). A Perspective on the Legacy of Edward Lorenz. *Earth and Space Science*, 6(3). https://doi.org/10.1029/2018EA000434.

Mcwilliams, J., Gula, J., Jeroen Molemaker, M., Renault, L., & Shchepetkin, A. (2015). Filament Frontogenesis by Boundary Layer Turbulence. *Journal of Physical Oceanography*, 45(8). https://doi.org/10.1175/JPO-D-14-0211.1.

Menemenlis, D., Campin, J., Heimbach, P., Hill, C., Lee, T., Nguyen, A., Schodlok, M., & Zhang, H. (2008). Ecco2: High resolution global ocean and sea ice data synthesis. *Mercator Ocean Quarterly Newsletter*, 31.

Monin, A. & Yaglom, A. (1979). *Statistical Fluid Mechanics: Mechanics of turbulence*, volume 1. M.I.T. Press.

Nelson, A., Arbic, B., Zaron, E., Savage, A., Richman, J., Buijsman, M., & Shriver, J. (2019). Toward realistic nonstationarity of semidiurnal baroclinic tides in a hydrodynamic model. *Journal of Geophysical Research: Oceans*, 124(9). https://doi.org/10.1029/2018JC014737.

Price, J., Weller, R., & Schudlich, R. (1987). Wind-Driven Ocean currents and Ekman transport. *Science*, 238(4833). https://doi.org/10.1126/science.238.4833.1534.

Qiu, B., Chen, S., Klein, P., Wang, J., Torres, H., Fu, L., & Menemenlis, D. (2018). Seasonality in transition scale from balanced to unbalanced motions in the world ocean. *Journal of Physical Oceanography*, 48(3). https://doi.org/10.1175/JPO-D-17-0169.1.

Qiu, B., Nakano, T., Chen, S., & Klein, P. (2017). Submesoscale transition from geostrophic flows to internal waves in the northwestern Pacific upper ocean. *Nature Communications*, 8:14055. https://doi.org/10.1038/ncomms14055.

Quintana, A. (2022). github.com/antonimmo/ebc-wk-spectral-analysis: v1.2.0. https://doi.org/10.5281/zenodo.6510574.

Richards, K., Whitt, D., Brett, G., Bryan, F., Feloy, K., & Long, M. (2021). The impact of climate change on ocean submesoscale activity. *Journal of Geophysical Research: Oceans*, 126(5). e2020JC016750 2020JC016750. https://doi.org/10.1029/2020JC016750.

Rocha, C., Gille, S., Chereskin, T., & Menemenlis, D. (2016). Seasonality of submesoscale dynamics in the Kuroshio extension. *Geophysical Research Letters*, 43(21). https://doi.org/10.1002/2016GL071349.

Rocklin, M. (2015). Dask: Parallel Computation with Blocked algorithms and Task Scheduling. In Kathryn Huff & James Bergstra, editors, *Proceedings of the 14th Python in Science Conference*, 126 – 132. https://doi.org/10.25080/Majora-7b98e3ed-013.

Savage, A., Arbic, B., Alford, M., Ansong, J., Farrar, J., Menemenlis, D., O'Rourke, A., Richman, J., Shriver, J., Voet, G., Wallcraft, A., & Zamudio, L. (2017). Spectral decomposition of internal gravity wave sea surface height in global models. *Journal of Geophysical Research: Oceans*, 122(10). https://doi.org/10.1002/2017JC013009.

Shcherbina, A., D'Asaro, E., Lee, C., Klymak, J., Molemaker, M., & McWilliams, J. (2013). Statistics of vertical vorticity, divergence, and strain in a developed submesoscale turbulence field. *Geophysical Research Letters*, 40(17). https://doi.org/10.1002/grl.50919.

Siegelman, L., Klein, P., Rivière, P., Thompson, A., Torres, H., Flexas, M., & Menemenlis, D. (2020). Enhanced upward heat transport at deep submesoscale ocean fronts. *Nature Geoscience*, 13(1). https://doi.org/10.1038/s41561-019-0489-1.

Su, Z., Torres, H., Klein, P., Thompson, A., Siegelman, L., Wang, J., Menemenlis, D., & Hill, C. (2020). High-frequency submesoscale motions enhance the upward vertical heat transport in the global ocean. *Journal of Geophysical Research: Oceans*, 125(9). e2020JC016544 2020JC016544. https://doi.org/10.1029/2020JC016544.

Sun, D., Bracco, A., Barkan, R., Berta, M., Dauhajre, D., Molemaker, M., Choi, J., Liu, G., Griffa, A., & McWilliams, J. (2020). Diurnal cycling of submesoscale dynamics: Lagrangian implications in drifter observations and model simulations of the northern Gulf of Mexico. *Journal of Physical Oceanography*, 50(6). https://doi.org/10.1175/JPO-D-19-0241.1.

Talley, L., Pickard, G., Emery, W., & Swift, J. (2012). Dynamical Processes for Descriptive Ocean Circulation. In *Descriptive Physical Oceanography*, (pp. 1–72). Academic Press.

Torres, H., Klein, P., D'Asaro, E., Wang, J., Thompson, A., Siegelman, L., Menemenlis, D., Rodriguez, E., Wineteer, A., & Perkovic-Martin, D. (2022). Separating energetic internal gravity waves and small-scale frontal dynamics. *Geophysical Research Letters*, 49(6). e2021GL096249 2021GL096249. https://doi.org/10.1029/2021GL096249.

Torres, H., Klein, P., Menemenlis, D., Qiu, B., Su, Z., Wang, J., Chen, S., & Fu, L. (2018). Partitioning ocean motions into balanced motions and internal gravity waves: A modeling study in anticipation of future space missions. *Journal of Geophysical Research: Oceans*, 123(11). https://doi.org/10.1029/2018JC014438.

Welch, P. (1967). The use of fast Fourier transform for the estimation of power spectra: A method based on time averaging over short, modified periodograms. *IEEE Transactions on Audio and Electroacoustics*, 15(2). https://doi.org/10.1109/TAU.1967.1161901.

Wenegrat, J. & McPhaden, M. (2016). A simple analytical model of the diurnal ekman layer. *Journal of Physical Oceanography*, 46(9):2877 – 2894. https://doi.org/10.1175/JPO-D-16-0031.1.

Wooster, W. & Reid, J. (1963). *Eastern boundary currents, The Sea, 2 MN Hill, 253–280*. Interscience, New York.

Yu, X., Naveira Garabato, A., Martin, A., Buckingham, C., Brannigan, L., & Su, Z. (2019). An annual cycle of submesoscale vertical flow and restratification in the upper ocean. *Journal of Physical Oceanography*, 49(6). https://doi.org/10.1175/JPO-D-18-0253.1.

Appendix

A. Validity of Reynolds conditions for the dynamical filtering

In section 4.1 we developed a mathematical framework that allowed us to "borrow" the statistical formulation of turbulence theory to the dynamical filtering approach. In particular, we used the Reynolds conditions to derive the equations of motion and kinetic energy for the filtered velocity fields. We also mentioned that, in a similar fashion as in the turbulence theory, the Reynolds conditions are only approximately valid. In this appendix we will show that the Reynolds conditions are also approximately valid for the dynamical filtering approach, in particular for the filter we developed in this thesis, and applied to the EBC.

Given the properties in Eqs. 28 hold for an arbitrary "low-pass" filter operator but 31e does not in general, we only need to ensure the latter is valid. Here, by "low-pass" filter, we mean a filter that preserves the mean (or zero-frequency and zero-wavenumber) component of the field.

Now, in analogy to the Reynolds conditions in the statistical formulation of turbulence theory, we just need to prove it approximately valid. To do that, we can estimate the validity of 31e by calculating the error function

$$Err(f,g) = |f_B g_B - \{f_B g\}_B| \tag{63}$$

In particular, since we are dealing with the horizontal components of the velocity field, U and V, we need to test that

$$\{U_B U\}_B \approx U_B U_B \tag{64a}$$

$$\{U_B V\}_B \approx U_B V_B \tag{64b}$$

$$\{V_B U\}_B \approx V_B U_B \tag{64c}$$

$$\{V_B V\}_B \approx V_B V_B \tag{64d}$$

First, we inspect the instantaneous error function (Eq. 63) for an arbitrary snapshot during the winter and summer seasons in the Canary current. The choice of this region was not entirely arbitrary, since it presents the most submesoscale BM activity, which are closer to the cutoff dispersion relation (see Eq. 6, or Fig. 5) of the filter, thus more likely to "leak" low frequency and low wavenumber interference into the BM regime.

In both seasons we can note the error function, compared to product terms, is small in the four different combinations (rows) in Fig. 27. This seems to be a good indicator that the filter is good enough to comply with the last Reynolds condition. Furthermore, if we wanted to make a broader comparison by combination and season, we could calculate the mean absolute error function at each, giving rise to the time-dependant error function

$$\text{MeanAbsError}\left[f,g\right](t) = \overline{Err\left(f,g\right)} \tag{65}$$

where the overbar ($\overline{f}$) denotes spatial mean of the instantaneous quantity. The result, as we might have already guessed, is a time series of how the error behaves during the whole season. Although this new function could suffice for a single variable, we need to compare the magnitude of the error for the four term combinations in Eqs. 64 between two different seasons. In order to provide the reader with a quick overview of how these errors are distributed, we decided to calculate the histogram of the 4 quantities, one by current and season, and compare them with the distribution of the absolute value of the products $\{U_i\}_B\{U_j\}_B$ (or $\{\{U_i\}_B U_j\}_B$) (see Eqs. 64).

At first glance, we note by inspecting the errors in winter and summer (Figs. 28 and 29, respectively) that it behaves similarly for the four cases and across both seasons. Moreover, considering the order of magnitude of the products of the filtered components of the field (Eqs. 64), we note that the relative error (i.e. the quotient of the absolute error and absolute the values of the products $\{U_i\}_B\{U_j\}_B$) can reach up to 20%, but the mean errors are around 10% or less. We can take this analysis to conclude that the Reynolds conditions of the BM-IGW filtered fields are **approximately valid**.

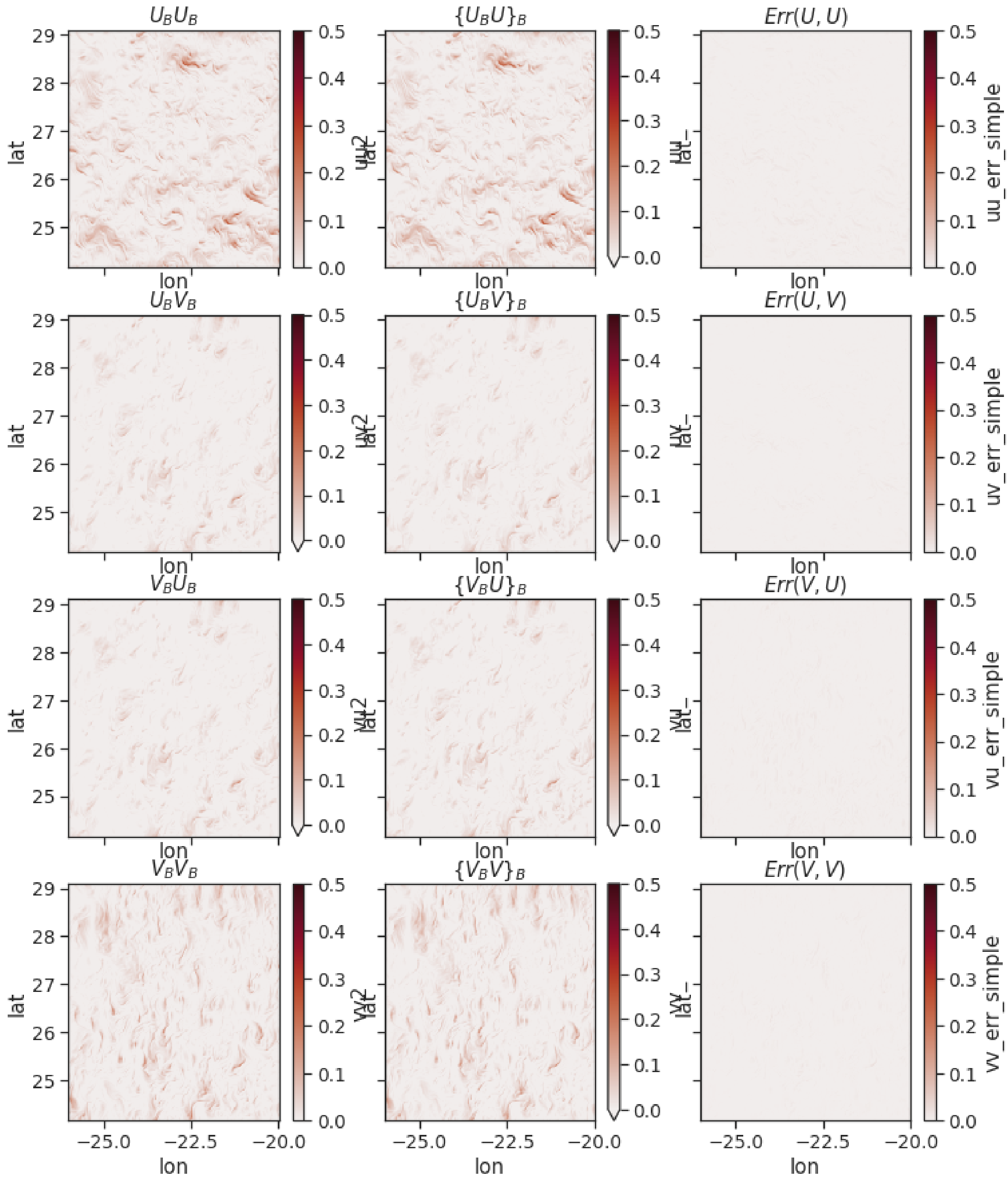

Figure 26. Snapshots of the terms referenced in Eq. 64 (left, center), and the absolute error function Err(U_i, U_j) (right) of the horizontal components of the velocity field, at the Canary current (26.42 °N) during the winter season (March 1st 2012, 17:00 local time). The two terms and the error function are presented using the same colour and scale to make the comparison more intuitive. The more similar the first two terms are, the smaller the error function is, and the more valid the Reynolds conditions become.

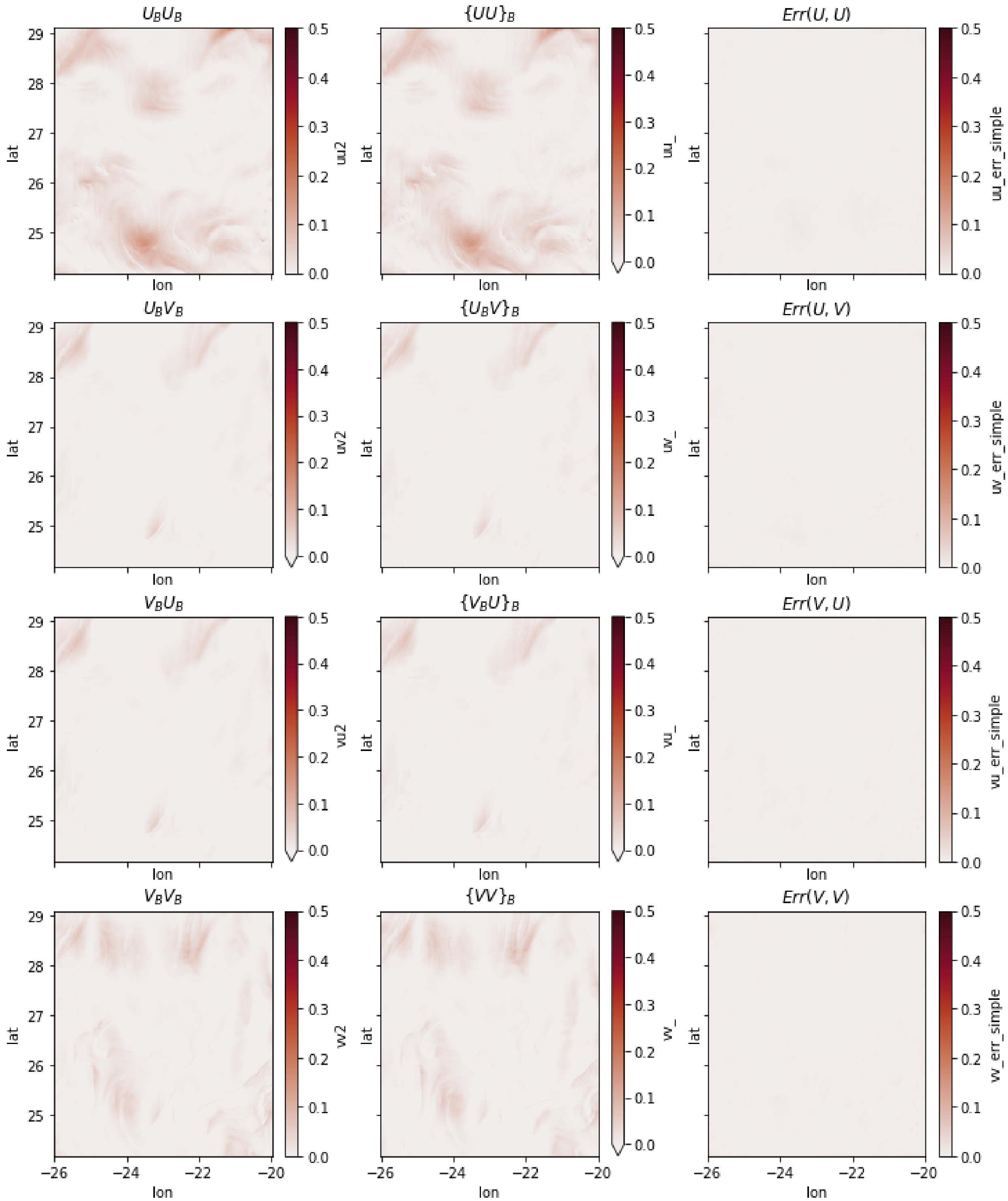

Figure 27. Snapshots of the terms referenced in Eq. 64 (left, center), and the absolute error function Err(U_i, U_j) (right) of the horizontal components of the velocity field, at the Canary current (26.42 °N) during the winter season (September 1st 2012, 17:00 local time). The two terms and the error function are presented using the same colour and scale to make the comparison more intuitive. The more similar the first two terms are, the smaller the error function is, and the more valid the Reynolds conditions become.

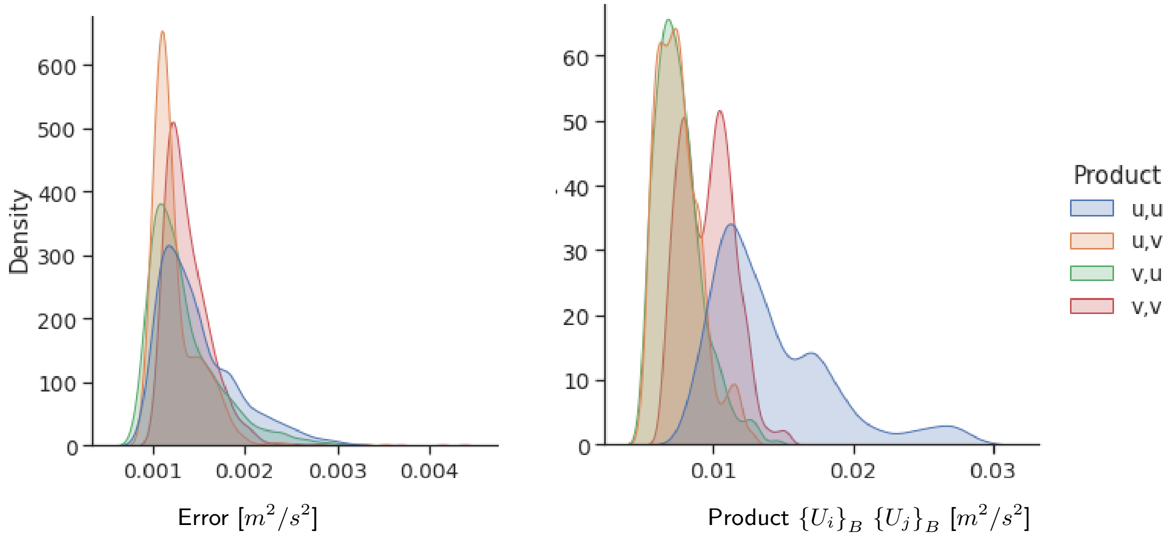

Figure 28. Estimated PDF of the mean Reynolds condition error (left, see Eqs. 65 and 63) and the mean absolute value of the products $\{U_i\}_B \{U_j\}_B$ (right, see Eqs. 64), at the Canary current (area around 26.42 °N) during the winter season. The units of the vertical axis are adimensional since it corresponds to a PDF, whereas the horizontal axes share the same units.

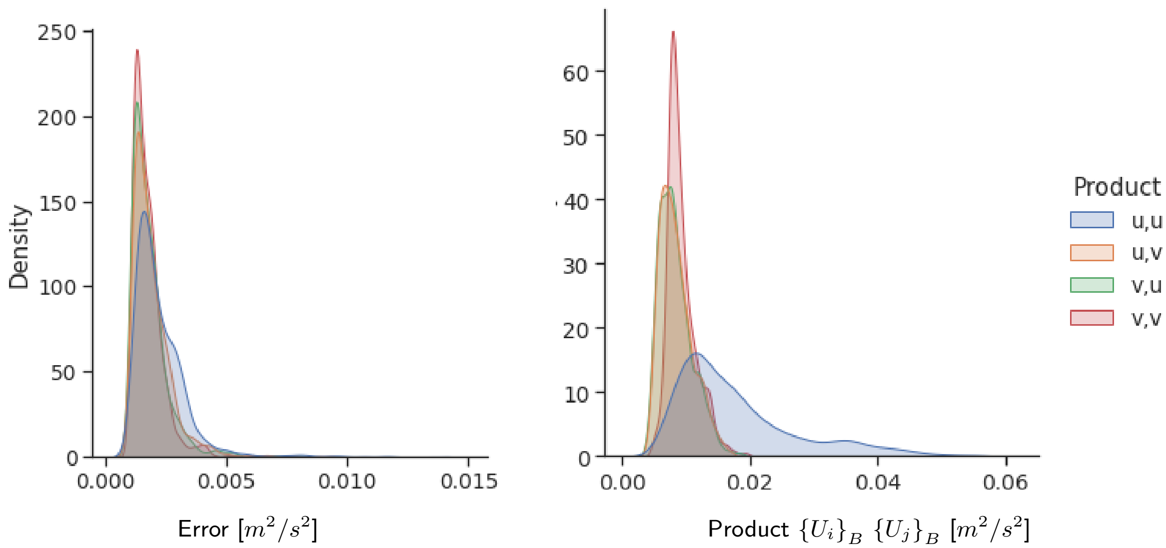

Figure 29. Estimated PDF of the mean Reynolds condition error (left, see Eqs. 65 and 63) and the mean absolute value of the products $\{U_i\}_B \{U_j\}_B$ (right, see Eqs. 64), at the Canary current (area around 26.42 °N) during the summer season. The units of the vertical axis are adimensional since it corresponds to a PDF, whereas the horizontal axes share the same units.